Development of Silver-doped Phosphate Glasses for Radio Photoluminescence Glass Dosimeter

by

Muhammad Taqiyuddin Mawardi Ayob

Thesis Submitted to Flinders University
for the degree of

Doctor of Philosophy

College of Science and Engineering
18th June 2019

Table of Contents

Chapter 1

Chapter 2

Chapter 3

Chapter 4

4. Adsorption of Polyelectrolyte Layers on Silver Nanoparticles   67
Surface: Synthesis and Hue Changing Study

ABSTRACT

A series of the radio-photoluminescent glass dosimeters (RPLGDs) with different ratios of chemical composition in the glass were successfully prepared using the wet melting method. RPLGDs are applicable for measurement of ionizing radiation at variant doses using silver-doped phosphate glass. When the RPLGD is exposed to γ-rays, electrons and holes produced by the γ-radiation are trapped by the Ag^+ ions, producing $Ag°$ and Ag^{2+} ions respectively, resulting in the emission of two RPL peaks at 460 and 620 nm. There were three main parts to this study which includes; 1) the silver nanoparticles (AgNPs) preparation, 2) formation of glasses with different ratios of chemical elements and 3) development of the RPLGD using the optimum ratio of chemical element composition with AgNPs. In this work, AgNPs with different sizes were prepared by polyol method. The basic physical and optical properties of the glasses, such as hardness, density, transmission, absorbance and photoluminescence values were analysed. The addition of protic polyethyleneimine and aprotic poly(sodium 4-styrene sulfonate) polymers produces different colour of final AgNPs solutions with yellow of AgNPs-PSS and colourless of AgNPs-Pei, respectively. Next, the glasses were prepared using wet chemical method and the optimal base composition range of phosphate glasses for RPLGDs was also investigated. The correlation between the RPLGD properties investigated and the glass compositions showed that the characteristic properties were dependant on the ratio of chemical compostition used. Based on thermo-physical and structural studies, the hardness test shows that the HRA values increased with increasing Al and Na content. Moreover, RPLGD series have the highest sensitivity between 3.0 to 5.0 wt.% of silver. Apart from that, the effect of various silver sizes addition on the phosphate glass microstructure, composition and chemical characteristics was investigated using X-ray diffraction, Fourier transform infrared and photoluminescence spectroscopy. It was established that the phosphate glasses suitable for dosimeter control possess density values ranging from 2.15 to 2.78 g.cm^{-3}. FT-IR spectra of Ag-doped phosphate glasses have been studied before and after 100 Gy of γ-irradiation. The decrease in oxygen content of glass sample after γ-irradiation was indicated by bond breaking in the glass sample. The orange RPL at 620 nm was associated with the 325 nm of the excitation band and this optical activity was due to the Ag^{2+} centers. The photoluminescence study of AgNPs-doped phosphate glass showed enhanced radiation sensitivity towards γ-radiation compared with phosphate glass doped with bulk silver under the same conditions. The AgNPs with 4.3 wt% showed the highest γ-ray detection sensitivity, which showed the highest PL peaks at the same absorbed dose, followed by 2.5 wt% and 7.7 wt%. In conclusion, using AgNPs as activators in the RPLGD will enhance the radiation sensitivity due to the rapid and excellent growth of the RPL centers within the forbidden band of the glass formed by the initial ionizing event.

Declaration

I certify that this thesis does not incorporate without acknowledgment any material previously submitted for a degree of doctor of philosophy and that to the best of my knowledge and belief it does not contain any material previously published or written by another person except where due reference is made in the text.

_____

Muhammad Taqiyuddin Mawardi Ayob

Acknowledgments

List of Figures

Chapter 4

List of Tables

List of Equations

List of Abbreviations

AELB	Atomic Energy licensing Board
ALARA	As Low As Reasonably Achievable
ARS	Acute Radiation Syndrome
BSE	Backscattered Electrons
CRN	Continuous Random Network
CRT	Cathode Ray Tube
DSC	Differential Scanning Calorimetry
DLS	Dynamic Light Scattering
EDXA	Energy Dispersive X-ray Analysis
FTIR	Fourier Transform Infrared Spectroscopy
HRTEM	High Resolution Transmission Electron Microscopy
ICRP	International Commission on Radiological Protection
JCPDS	Joint Committee on Powder Diffraction Standards
NBO	Non-Bridging Oxygen
NDRP	National Directory for Radiation Protection
OSL	Optically Stimulated Luminescence
PMF	Potential of Mean Force
PMT	Photomultiplier Tubes
PID	Proportional, Integral and Derivative
RPLGD	Radiophotoluminescent glass dosimeter
SEM	Scanning Electron Microscopy
SE	Secondary Electrons
SERS	Surface Enhanced Raman Spectroscopy
TEC	Thermal Expansion Coefficient
TGA	Thermal Gravimetric Analysis
TO	Terminal Oxygen Bond
TLD	Thermoluminescence Dosimeter
UV-Vis	Ultraviolet-Visible Light Spectroscopy
XRD	X-ray Diffractometer

List of Units

α	Alpha-ray
Å	Angstrom
β	Beta-ray
K_T	Compressibility
q	Cooling Rate
ρ	Density
H	Enthalpy
e^-	Electron
V_{fg}	Free Volume of The Glass
V_o	Frequencies of The Incident Lights
V_i	Frequencies of The Scattered Lights
γ	Gamma-ray
G	Gibbs Free Energy
C_P	Heat Capacity
h^+	Hole
V_m	Molar Volume
t_o	Observation Time
T_{ds}	Softening Temperature
Sv	Sievert
T_f	Fictive Temperature
Q^n	Structural Units
α_T	Thermal Expansion
T_g	Transition Temperature
T_m	Melting Point
t_r	Relaxation Time
V_g	Volume Of Glass
α_{TL}	Volume Thermal Expansion of Liquid
α_{Tg}	Volume Thermal Expansion of Glass

Chapter 1

1. Introduction

1.1 Background of research

Nowadays, there is a lot of radiation dosimeter were used to detect and measure radiation reliably including the dose rate and distribution of radiation source from ionizing radiation to numerical value and an appropriate unit. There are several types of solid state dosimeters that have been developed, not only for personal monitoring but also for environmental background radiation monitoring. For instance, a thermoluminescence (TL) dosimeter has been studied to monitor the environmental background radiation [1]. Recently, new passive solid state dosimeters utilizing optically stimulated luminescence (OSL) dosimeter [2], direct ion storage (DIS) dosimeter [3] and radiophotoluminescence (RPL) dosimeter have been developed not only to monitor personal and but also environmental radiation [4]. The characteristics of TLD, OSLD and RPLGD were recorded in Table 1.1.

Table 1.1:   The characteristics comparison of TLD, OSLD and RPLGD [5]

	TLD	OSLD	RPLGD
Principle of measurement	Luminescence signal	Optically stimulated luminescence signal	Radiophotoluminescence signal
Luminescence material	Crystal	Crystal	Glass
Excitation source	Heat	Visible light	Ultra-violet laser
Sensitivity	Material-dependent	Material-dependent	Good
Repeatable readout	No	Yes, but intensity reduced	Yes, with the same intensity
Range of	Material	Material-	10 μ - 10 Gy (personal)

measurement	dependent (10 μGy – 10 Gy)	dependent (10 μGy – 10 Gy)	1 - 500 Gy (environment)
Capability to distinguish the types of radiation	Yes	Yes	Yes
Re-useable	Yes	No	Yes

From Table 1.1, the advantages of the RPLGD are good reproducibility of readout values, low energy dependence, long stability, better dose linearity and capability of repeatable readouts without damaging the system. Generally, radiophotoluminescent glass dosimeter for measuring and recording ionizing radiation has been introduced since 1951 by Schulman [6]. These dosimeters are silver-bearing phosphate glass dosimeters which are similar to film dosimeters and are generally used for personnel dosimetry [6]. These glass dosimeters, generally comprising two polished surfaces vertical to each other, are exposed to an Ultraviolet light source after having been exposed to prior radiation. The fluorescent radiation thus emitted is proportional to the radiation dose received, and is measured vertically in the direction of the incident UV-radiation. Although RPLGD and TLD systems were developed in parallel during 1960s, photon energy dependence of the detector material and high pre-dose of RPLGD prevented major breakthrough of glass dosimetry. Therefore, RPLGDs were used only as an emergency dosimeter in accident situations [7]. However in mid 1980s, the readout systems using pulsed UV stimulation were introduced using mercury UV lamps was helped in reducing pre-dose level by a factor of 100 (from mSv to a few μSv). This development results revealed improving in the RPLGDs manufacture with fully automatic RPL reader systems which capable of measuring doses range between 10μSv and 10Sv [8].

The basic principle of RPLGD is that the luminescence or colour centres are formed when the luminescent material inside the glass compound is exposed to radiation and fluorescence are emitted from the colour centres after they are irradiated with ultra-violet light. The colour centres formed by such radiation are believed to represent interference centres which emit fluorescent light in the visible spectrum as radio-photoluminescence phenomena when the glass was exciting with UV light. The intensity of the emitted light is linear to the ionizing radiation dose

received up to certain dose level depending on glass sensitivity and chemical compounds in the glass.

The natural fluorescence of such compositions, which has been described as an "initial dose", comprises several components [9]. The initial dose is partially dependent on the glass composition employed, the melting conditions used, the surface finish of the glass dosimeter and chemical changes which have taken place at the surface due to atmospheric influences [10]. Such noble metal-activated phosphate glasses especially silver metal should desirably show a low natural fluorescence upon UV light stimulation, as well as a high sensitivity to radiation. The silver metal content of the phosphate glass has an important function as activator on the build-up performance, which accelerates the build-up, while a decreasing content retards build-up. The silver was chosen as activator in the phosphate glasses because it shows extraordinarily efficient at absorbing and scattering light, which have a colour that depends upon the size, shape and the local refractive index of the particle. At nanoscale, the strong interaction of silver nanoparticles with light occurs because the conduction electrons on the metal surface undergo a collective oscillation when excited by light at specific wavelengths, much higher than identically sized non-plasmonic nanoparticles, known as a surface plasmon resonance (SPR) [11].

Another chemical element is alkali metal. The lithium proportion ensures a low effective order of magnitude while at the same time giving a low natural luminescence or initial dose to the dosimeter. In most applications, it is desirable to exclude thermal neutron sensitivity so that the glasses used in such dosimeters must not contain lithium. Sodium and potassium are available as substitutes for the alkali metal lithium in phosphate glasses [12]. Additionally, such high alkaline metaphosphate contents result in poor resistance to atmospheric weathering. In principle, it is possible to improve the surface chemical resistance by the addition of beryllium oxide or beryllium phosphate, as the low position of beryllium in the periodic table of the elements is an advantage in favouring low energy dependence but this is not a desirable alternative in view of the extreme toxicity of beryllium compounds. Alternatively, magnesium or calcium compounds can be used to improve the surface chemical resistance. However, the sensitivity of this glass is somewhat less than that of a comparable magnesium-free dosimeter glass and the

initial dose increases as the result of the changed chemical composition. The purpose of this research was to explore the different types of composition elements with different percentage of weight compositions for producing high sensitivity RPLGD to detect and measure the exposure dose from ionizing radiation to make it suitable for personal and environmental dosimeter.

1.2   Rational of the research

Solid state dosimeters can be divided into two categories; active dosimeters and passive dosimeters. Active dosimeters are used for dose measurements in areas with unknown radiation level to accumulate the radiation dose readings immediately. The common active dosimeters available in the market are scintillation counters, semi-conductor detectors and gas-filled counters. Besides that, passive dosimeters are used as periodic radiation monitor for radiation worker who work in the radiation area to monitor the accumulated dose and the types of radiation. It can be used as personal or environmental dose measurement monitor. The film badge, optically stimulated luminescence dosimeter (OSLD), thermoluminescence dosimeter (TLD) and radio-photoluminescence glass dosimeter (RPLGD) are example of passive dosimeters. RPLGD was chosen from other passive dosimeters for the measurement of radiation absorbed dose because RPLGD displays high sensitivity, low energy dependence and good chemical stability. Moreover, the centres of luminescence will never disappear unless the glasses are annealed with high temperatures of about 400 °C. This produces some excellent features such as reproducibility, repeatable measurement, type of radiation and small dispersions among samples [13].

Recent technological applications have generated much interest in the study of glasses especially oxide glasses [14]. Among oxide glasses, phosphate based glasses are particularly attractive due to their ability to accommodate large concentrations of active ions without losing their useful properties of the material [15]. Phosphate glasses are relatively easy to prepare and offers a large range of compositional possibilities, which facilitates in tailoring the physical, chemical and optical properties of interest for specific technological applications and RPLGD is one of them. One of major component for luminescence properties of RPLGD is from noble metal element which is silver metal. The investigation of silver metal

luminescence in phosphate glasses was the subject of this research in relation to the use of these materials as γ-radiation and X-radiation dosimeters.

In 2017, a radiophotoluminescent glass dosimeter was used to verify the dose accuracy for the CyberKnife procedure and validate a viable dose verification system for CyberKnife treatment [16]. Apart from that, there was a research on demonstration of a real-time fiber-optic-coupled dosimetry system using Ag-activated phosphate glasses based on radiophotoluminescent (RPL) phenomena in 2018. The performance characterization using real-time fiber RPL glass dosimetry is compared with that of real-time fiber plastic scintillation dosimetry [4]. Moreover, the direct observation and characterization of silver nanoparticles embedded in a Ag^+-activated phosphate glass was demonstrated by Zheng and Kurobori (2011). Correlations between the isolated Ag^+ concentration and X-ray-induced silver species were systematically examined using optical measurements with transmission electron microscopy [17]. Therefore, the purpose of this study was to explore the ratio of composition elements for producing high sensitivity RPLGD using different sizes of silver particle in simple process and measures the absorbed doses of γ-irradiation to make it suitable for personal and environmental dosimeter.

1.3   Research hypothesis

The chemical elements in the glass composition influences the sensitivity to ionizing radiation and the RPL 'build-up' kinetics. For example, a higher concentration of $Al(PO_3)_3$ makes the build-up slower, indicating the importance of base compositions analysis. Moreover, the RPL centre concentration will increases as dosage of ionizing radiation increases. Beside glass composition, the irradiation dose consumption to RPLGD also affects the readout characteristic. At high dose irradiation, the reduction of RPL efficiency probably occurs due to attenuation of UV radiation, not to saturation of trapping or recombination centres in a dosimeter. The amount of each chemical composition in matrix glass and ionizing radiation dose level are studied to determine the optimum value of each chemical elements and dose range of ionizing radiation of RPLGD.

Silver particle play important role in phosphate glass for radiation dosimeter. Doping of silver metal to phosphate glass matrix resulted in a structure changed with

higher compressive modulus and more sensitivity to radiation than phosphate glass alone [18]. Silver metal-doped phosphate glass after exposure to γ-radiation exhibits an intense luminescence caused by excitation with UV light. The excited electrons generated from the colour centres return to the original colour centres after emitting the fluorescence. This phenomenon is called radio-photoluminescence (RPL). Because the electrons in the colour centres return to the electron traps after emitting the fluorescence, it can be re-readout the count with a single irradiation. The number of silver content is proportional to energy levels in colour centres and the numbers of electron trap(s) [18]. However, excessive numbers of silver will decrease the penetration efficiency of the UV light and increases energy dependence [18]. Therefore, a sufficiently loaded ratio of silver content is required for the best luminescence and excitation efficiency. A comparative study between silver bulk and silver nanoparticles (AgNPs) doped phosphate glass was also done to produce high sensitivity RPLGD.

The influence of activator concentration in the glass for dosimetric properties of RPL glasses including chemical durability was also an important part to study. Alkali metal play an important role in the dosimetric properties of RPLGD related to the stabilization of RPL centres. The formation of RPL centres includes two processes; at first, electrons and holes trapped defect centres are generated in the phosphate glass network after ionizing irradiation and alkali ions are involved in the formation of phosphorus oxygen hole centres (POHC). Secondly, holes and electrons are trapped by silver metal ions and stable RPL centres are formed. For example, the lithium alumina-phosphate glasses have low energy dependence compared to other alkali alumina-phosphate glasses because of its low effective atomic number, thus they are widely used in RPLGD [18]. It was found that POHC is transferred to ionic silver and be the main reason of RPL build-up [19]. The concentration of ionizing radiation induced defect centres affects the characteristics of RPL centres according to the principle of RPLGD. So, the aim is to find out suitable type of alkali ions and the optimum weight percentage (wt.%) in glass composition of RPLGD.

The formation and assignment of irradiation induced defect centres (colour centres) in silver metal-doped phosphate glass induced by γ-radiation would create the ability to change the optical characteristics, most notably the refractive index of

phosphate glasses doped with silver particles. In particular, using AgNPs-doped in phosphate glass using the wet melting method was studied to clarify the formation kinetics and obtain additional evidence of silver metal-related colour centres in a RPL glass and leading to different optical signature. As far as the AgNPs in glass were concerned, it shows some excellent optical properties such as large third-order nonlinear susceptibility and ultra-fast nonlinear response. Further analysis of induced colour centres and mechanism of RPL in RPLGD were carried out through physical and optical properties measurements by radiative lifetime and thermal treatment.

1.4   Research objective

1.   To demonstrates the formation of colloidal complex of silver-polymer with different sizes and high stability.
2.   To optimise the chemical formulation of glass compositions for improving the optical properties and the RPL 'build-up' kinetics in RPLGD.
3.   To determine the optimum weight of different sizes of silver metal (bulk and nanoparticles) doped in phosphate glass, based on the energy levels in the colour centre.
4.   To provide RPLGD which are substantially free from highly toxic compounds such as beryllium and arsenic. Besides that, to characterize physical, chemical and optical properties of RPLGD including the emission mechanism of radio-photoluminescence in the RPLGD.

1.5   Scope of the research

The scope of this research covered all the preparation, characterization and testing related to AgNPs and RPLGDs. At the beginning, the wet melting method was employed to synthesize Ag-doped phosphate glasses. All samples were coloured by γ-irradiation with specific dose rate. In order to study the character of RPLGD, the crystallization behaviour of the glasses were characterized using differential scanning calorimetry (DSC) at a normal heating rate of 10 °C.min^{-1} with temperature measurement accuracy of 5 °C. Glass transition temperature (T_g) and softening temperature (T_{ds}) of the glass samples was also measured using DSC. The phases formed were identified using X-ray diffractometer (XRD). The density of the prepared glasses were measured using the Archimedes principle, with distilled water

as the immersion fluid at room temperature (25±1 ºC).Mechanical strength/hardness of glasses were determined by using a Rockwell indentation technique with a 10 kgf preload and 60 kgf major load of diamond cone. The absorption edge and transmission also depend on the composition as well as the nature of glass network therefore optical absorption studies were carried out using UV-Vis spectrophotometer. Non-bridging oxygen atoms can also lead to the creation of localized centres in the glasses and some of them can give luminescence peaks on optical excitation. Luminescence spectra (excitation and emission peaks) of each glass samples were measured using photoluminescence instrument. FTIR spectroscopic techniques were used as chemical analysis regarding the structural aspects of the glasses. To show the sensitivity of glasses for ionizing radiation detection, each of the glass samples will be irradiated at different dose levels, ranging from 5 Gy to 2000 Gy using γ-radiation. Results were elaborate and discussed.

Chapter 2

2.   Literature Review

2.1   Silver nanoparticles

Nanotechnology is rapidly growing by producing nanoproducts and nanoparticles (NPs) that can have novel and size-related physicochemical properties differing significantly from larger matter. Research based on advanced nanomaterials of noble metals like silver has conquered a lot of interest among scientists during the past decades for its physiochemical properties such as size, distribution and morphology, they have been studied for catalytic activity [20], optical properties [21], antibacterial properties [22] and magnetic properties [23] and its application in various field such as biomaterial production, biochemistry, medical and pharmaceutical products [24], toothpastes, optical receptors and bio-sensing. Generally, the synthesis of nanoparticles has been carried out using three different approaches, including physical, chemical, and biological methods. In physical methods, nanoparticles are prepared by evaporation-condensation using a tube furnace at atmospheric pressure. The advantages of physical methods are speed, radiation used as reducing agents, and no hazardous chemicals involved, but the downsides are low yield and high energy consumption, solvent contamination, and lack of uniform distribution [25]. Chemical methods use water or organic solvents to prepare the silver nanoparticles. This process usually employs three main components, such as metal precursors, reducing agents, and stabilizing/capping agents. Basically, the reduction of silver salts involves two stages (1) nucleation; and (2) subsequent growth. In general, silver nanomaterials can be obtained by two methods, classified as "top-down" and "bottom-up". The "top-down" method is the mechanical grinding of bulk metals with subsequent stabilization using colloidal protecting agents. The advantage of chemical methods is high yield, contrary to physical methods, which have a low yield.

In general, silver nanoparticles can be produced by various methods including the chemical reduction of silver ions [26], thermal decomposition in organic solvents [27] and polyol method [28]. All these advances have promoted the scientific

knowledge on the nature of nanomaterials. The synthesis method used in the present study is the so-called polyol method, which is well suited for the preparation of nano-sized metal or oxide particles of various shapes [29]. The general polyol process involves the dissolution of a protecting agent or stabilizer in a polyol medium. The required silver precursor is then added to this solution. Although the synthesis process of monodisperse silver nanoparticles is well established, little is known about the influence of precursor injection during the polyol synthesis for silver nanoparticle sizes control.

2.2 Glass: Definition

A glass is an inorganic product form by fusion process from certain compound, which has been cooled to stiff condition without crystallization and can be defined as a non-crystalline solid material. Glass is an amorphous solid completely lacking in long-range periodicity and exhibit glass transition behaviour [30]. The terms amorphous and non-crystalline are synonymous and configurationally like frozen liquid [31]. The glass transition is a phenomenon in which a solid amorphous phase shows an abrupt change in the derivative thermodynamic properties from solid like to liquid like values with change of temperature [30]. From a thermodynamic point of view, the glassy state is a meta-stable state and unlike crystalline state which depends upon the thermal history of the melting process and represents a local minimum in the free energy. Given adequate time, the system will relax to a more stable state of lower free energy, provided the energy barrier separating these states can be crossed [32]. However, the time taken for relaxation of most present glasses is too long that meta-stability questions are purely academic interests.

2.3 Glass transition phenomenon

The glass transition is an essential attribute of any glassy material. The glass transition phenomenon is quite complex and many theories have been suggested based on various parameters and properties, which characterize the glasses. These theories have been successful only to a limited extent as the glass transition is a function of many parameters including heat capacity, thermal conductivity, melting temperature, cooling rate and etc. Significant variation in the value of glass transition

temperature (T_g) has also been observed depending on the method used for its measurement because during heating, the degrees of freedom start getting relaxed and when a melt is quenched to form a glass, the different degrees of freedom get arrested [31]. These different degrees of freedom, corresponding to different properties, which are used to evaluate T_g, relax at different rates and result in different values of T_g being measured. Although glass has atomic arrangement akin to liquid state, in terms of all other properties such as rigidity, glass is unequivocally a solid. This phenomenon can be understood readily by monitoring the changes in enthalpy or volume as a role of temperature in figure 2.1.
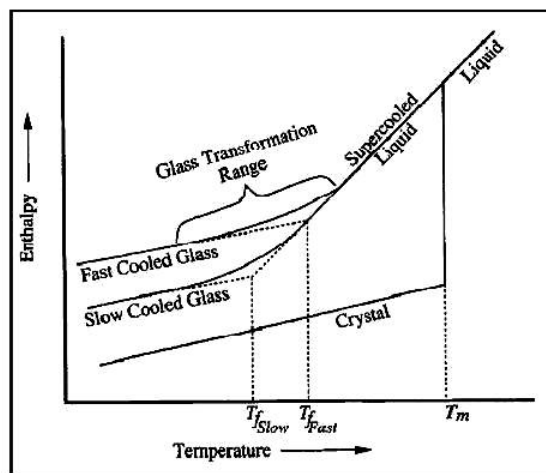
Figure 2.1: Variation in enthalpy/volume of a glass forming melt with temperature [31].

The crystallization process is manifested by an abrupt change in extensive thermodynamic variables like enthalpy (H) or volume (V) at melting point (T_m), whereas glass formation is characterized by a gradual change in slope line. The temperature range over which the change of slope occurs is called the *glass-transformation range* as shown in Figure 2.1. As the transition of liquid to the glassy state is continuous, the T_g cannot be defined. However, for convenience, the T_g is expressed as fictive temperature (T_f); the temperature obtained by intersection of the extrapolated liquid and glass curves as shown in Figure 2.1 and it depends on the cooling rate of the super cooled liquid. The slower the rate of cooling, the larger is the region in which the liquid may retain super cooled state, implying lower T_f or T_g, thus the T_g of a glass is not an intrinsic property but depends on its thermal history [31]. Dependence of T_g on the cooling rate q is given as:

$$q = q_0 e^{-\frac{1}{c}\left(\frac{1}{T_g}-\frac{1}{T_m}\right)} \tag{2.1}$$

where c and q_o are constants [31]. The experimentally measured value of T_g is not unique and depends on the time scale of the experiment used to observe it.

The relaxation process is also important aspect of glass transition which is related with configurational changes. The relaxation process becomes slow as the temperature decreases because at T_g, the material shows a solid like behaviour for observation time (t_o) which is smaller than the structural relaxation time (t_r). For $t_r <$ t_o, the material behaves like a liquid. A transition has taken place when the parameters corresponding to liquid like behaviour differ significantly from solid like ones, in case of heat capacity. In other words, T_g should occur when $t_o = t_r$.

The glass transition can also be expressed as a phenomenon in which a solid glassy phase shows immediate change in the derivative thermodynamic properties such as thermal expansion coefficient (TEC) at the transition temperature or heat capacity [31]. The order of a phase transition in *Ehrenfest scheme* is defined as the order of the lowest derivative of Gibbs free energy (G), which shows a discontinuity at the transition point [31]. In liquid to crystal transition at freezing or melting temperature, the volume and enthalpy, which are the first derivative Gibbs free energy, are discontinuous. Hence, liquid to crystal transition is a first order transition. However, for liquid to glass transition the thermodynamic variables such as volume, enthalpy and entropy are continuous and the quantities such as thermal expansion (α_T) compressibility (K_T) and heat capacity (C_P), which are the second order derivative of Gibbs free energy, are discontinuous. Hence, the glass transition is a manifestation of a second order phase transition. However, this simple model is unable to explain the change in T_g values, depending on the thermal history of the glass samples. Therefore, the glass transition is not a simple second-order phase transition. However, without involving a second-order thermodynamic transition, Prigogine & Defay (1954) showed that the ratio R defined as follows:

$$R = \frac{\Delta K_T \Delta C_p}{TV(\Delta \alpha_T)^2} \tag{2.2}$$

where R = 1 is equal to unity if a single ordering parameter determines the position of equilibrium in a relaxing system, but if R > 1 which is more than one ordering parameter is responsible, the latter case seems to describe most glasses [33].

Glass transition phenomenon has also been explained by invoking the free volume theory [34]. In this model a glass is assumed to consist of hard spheres. The total volume of the glass is divided into two parts namely the one occupied by molecule or spheres, V_{oc} and another part, V_f, in which molecules are free to move. For a glassy material, free volume is independent of temperature and gets frozen at certain locations when glass is formed. For liquids, with decrease in the temperature both free and occupied volumes decrease and there occurs a redistribution of free volume. According to free volume theory, the glass transition occurs when the free volume of a liquid is decreased below a critical value. The fractional free volume is given by the expression:

$$V_{ff} = \frac{V_{fg}}{V_g} = T_g \times \Delta\alpha_T \qquad (2.3)$$

where V_{fg} is the free volume of the glass, V_g is the volume of glass and $\Delta\alpha_T = \alpha_{TL} - \alpha_{Tg}$, where α_{TL} and α_{Tg} represent volume thermal expansion of liquid and glass respectively. It has been demonstrated that for several glasses, 10% of the total volume is free at T_g [35]. Free volume theory has been modified for wider applicability by incorporating percolation theory [36], which accounts for the exchange of free volumes between the nearest neighbour liquid like cells without any simultaneous change in the volumes of any solid like cells. In conclusion, these theories are qualitatively successful in explaining glass transition phenomenon for a variety of systems. Any complete theory describing the formation of a glass from the liquid state must therefore combine both relaxation and thermodynamic aspects in a natural way and the recent developments of free volume theory using percolation arguments perhaps point the way to this goal.

2.4   Structural aspects of glasses

The structural arrangements of atoms in matrix are the important part of glass system to understand its physical and chemical properties. The structure of crystalline materials is well established and is classified according to structure of the

unit cell. However, the lack of symmetry and periodicity in amorphous materials make such approach inapplicable for them. Even though there is lack of long range periodic order, these materials often possess considerable structural order over length scale of many angstroms, Å [37]. Therefore, a length scale may be arbitrarily defined, which separates by microscopic structures from macrostructure in amorphous solids phase [38].

Glass formation does not depend on the bonding types but the inorganic glasses with mixed covalent ionic bonds existing in metallic and organic glasses. Therefore, determination of structure for every class of glass is a wide scientific field with a number of different theories and experimental methods to confirm them. The most important structural model for oxide glasses was proposed by Zachariasen (1932) based on continuous random network (CRN) hypothesis by the existence of the polyhedral that are linked together to form an overall random network [39]. He suggested that the oxide crystalline and the glassy form should have the same type of oxygen polyhedral joined in a similar way except that in the glassy phase there is range of bond angles and bond lengths. Furthermore, the network should be sufficiently flexible to incorporate the disorder, which is characteristic of the glassy phase and the internal energy of both the crystalline and glassy phase should be comparable. The X-ray diffraction (XRD) studies of A_2O_3 carried out by Warren supported this theory [40]. The difference in structure of crystalline and glassy forms of a hypothetical two dimensional A_2O_3 is shown in Figures 2.2.
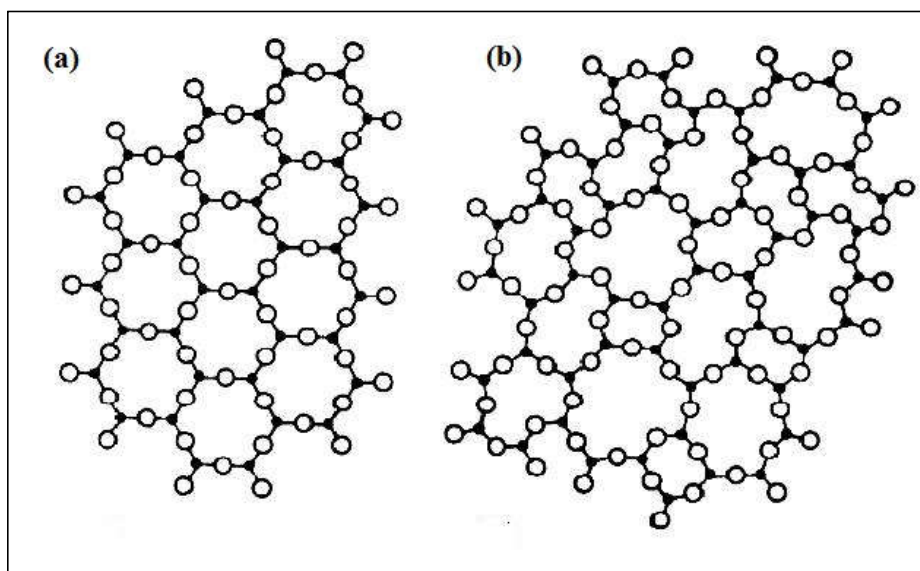
Figure 2.2: Atomic structural representation of (a) A_2O_3 crystal and (b) A_2O_3 glass (Filled circles are "A" = cations & hole circles are "O" = oxygen) [40].

Thus, both of the crystalline and glassy forms are composed of A_2O_3 triangles joined to each other at corners, except that the glassy form has disorder introduced by changes in the A−O−A bond angles and A−O bond length. The triangles or O−A−O angles themselves are not deformed much. Apart from that, network modifier oxides (e.g. Na_2O) depolymerize the perfectly connected continuous random network of glass formers (e.g. SiO_2). The action of the modifier is to break up the continuous silica network by introducing non-bridging oxygens (NBOs). This process is shown in Figure 2.3 and is not limited to silica glass only, but also can occur in other inorganic systems such as phosphate glass.
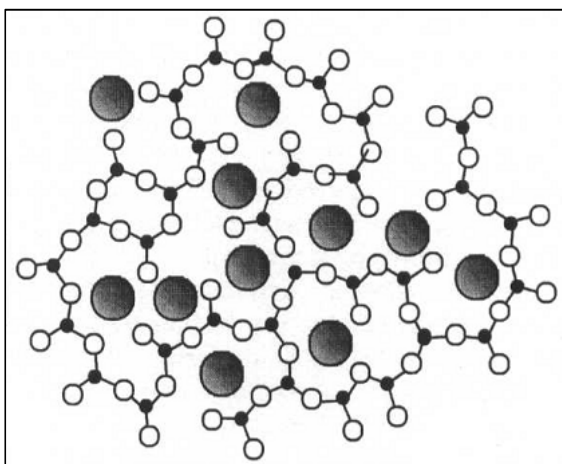
Figure 2.3: Two-dimensional schematic diagram of the silica glass structure in the presence of Na^+ and the formation of NBOs (Filled big circles = Na^+, filled small circles = Si^{4+} & hole circles = O^{2-}) [40].

The original CRN model of glass structure can also be extended to describe the structure of strongly ionic or covalent non-oxide glasses such as halides and chalcogenides, respectively. Contrariwise, the structure of organic glasses where molecular units are held by van der Waals forces requires a random-packing type of description, similar to the structure proposed for metallic glasses [41]. The lack of experimental information about the structure of glass and the difficulties in

describing the polymerized structure in the long range extent can be partially solved by the concept of atom specific structure elements [42].

2.5   Types of glasses

Glasses have been classified into two different categories; 1) Based on the actual components present in them and 2) Based on their end use. Glasses based on silicate, phosphate, borate, borosilicate and so forth, networks belong to the first category; whereas optical glasses, sealing glasses, laser glasses and so forth, correspond to the second category. In this study, the glass description was focus more on phosphate glass regarding the different structural aspects and properties of this glass where presented in the following section.

2.5.1   Oxide glasses

Oxide glasses are historically the oldest and industrially the most exploited. Human uses of these range from the ancient to the leading edge of new technologies of data processing and transmission such as lasers, optical fibre and semiconductor devices and also the long-term nuclear waste storage [43]. For example, Phosphate glasses are highly resistant to acid such as hydrofluoric acid and used as efficient heat absorbers when iron oxide is added [44]. Therefore, most researchers are working on oxides glasses based on its chemical compositions with special physical, chemical and thermal properties to be used in suitably applications.

Phosphate Glasses: Introduction

Glass having P_2O_5 as one of the major components are called phosphate glasses. Electronically phosphate glasses often have larger band gaps than silicates glass, therefore gives better ultraviolet transmission [45]. Phosphate glasses have comparatively low T_g making them easy to process and with high TEC well matched to those of metals especially with low melting and high expansion metals like Al, Cu and so forth [10]. Certain phosphate glass compositions (e.g. aluminium phosphate) have large rare-earth stimulated emission cross sections and low thermos-optical coefficients compared with silicate glasses and are the materials of choice, particularly for high power laser applications [46]. Phosphate glasses also have low dispersion and relatively high refractive indices compared with silicate-based glass

and are developed for achromatic optical elements. Phosphate melts have high solubility factors for heavy cations and anions which lead to a range of fast ion conductors for solid state electrolytes. These glasses have high ionic conductivity as well as thermal and electrochemical stability. Therefore, these glasses are extensively studied for solid-state ionic devices [47].

Pure P_2O_5 glasses are highly moisture sensitive and immediately react with water and hence are less practical importance. Like silicate glasses, the phosphate glasses are constructed from corner-sharing tetrahedral, with the important difference that these are three-fold rather than four-fold coordinated because of one of double bond oxygen. Schematic diagram representing different Q^n structural units present in phosphate glasses is shown in Figure 2.4.
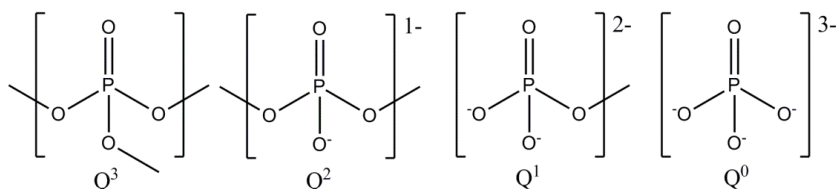
Figure 2.4: Phosphate tetrahedral units with Q^0 to Q^3 that could exist in phosphate glasses [10].

The properties that make phosphate glasses candidates for so many different applications are related to their molecular-level structures. Additionally, recent neutron diffraction studies of these glasses revealed that vitreous P_2O_5 contains two types of P-O bonds; 1) P-TO (TO = terminal oxygen bond) or P-NBO (NBO = non-bridging oxygen bond) and 2) P-BO (BO = bridging oxygen bond). Addition of modifying oxides to vitreous P_2O_5 results in the conversion of BO to NBO. Interpretation of structural aspects and physico-chemical properties of alkali phosphate glasses have to be made only after accounting for moisture contents in these glasses. Initially development and technological applications of phosphate glasses was limited by their poor chemical durability but eventually problem of durability solved by the inclusion of suitable chemicals like Al_2O_3, In_2O_3, Fe_2O_3 and so forth [48]. The moisture sensitiveness of phosphate glasses arises because of TO/NBO atoms present in it. These NBO atoms can be made to have strong covalent

linkages with other metal ions like Al^{3+}, Sb^{3+}, Bi^{3+} and etc, thereby reducing the hygroscopic nature of samples [48].

Background of Phosphate Glasses

The basic building blocks of crystalline and amorphous phosphates are the P-tetrahedra that results from the formation of sp^3 hybrid orbitals by the P outer electrons ($3s^2 3p^3$). The 5th electron is promoted to a 3d orbital where strong p-bonding molecular orbitals are formed with oxygen 2p electrons [49]. These tetrahedral links through covalent BOs and form various phosphate anions. The tetrahedral are classified using the Q^n terminology, where *n* value represents the number of BOs per tetrahedron as shown in Figure 2.4. The networks of phosphate glasses can be classified by the oxygen-to-phosphorus [O]/[P] ratio, which sets the number of tetrahedral linkages through BOs, between neighbouring P-tetrahedral [50].

Zachariasen in 1932 identified vitreous P_2O_5 as one of the prototypical *random network* glass formers as Q^3 tetrahedra. Hagg in 1935, however, challenged Zachariasen's idea that glass forming tendency relied upon the development of a random, three dimensional network, using the metaphosphate composition as an example of glass formation in which a large one-dimensional 'molecular' group are based on Q^2 tetrahedra inhibits crystallization [51]. However, the chromatography studies of Wazer and other researchers have reinforced the utility of the description of phosphate glass structures in terms of distributions of molecular species such as those proposed by Hagg. However, these two descriptions of glass structure are not incompatible because both predict local bonding similarities in glasses and crystals of identical composition. More importantly, these two models also illustrate the need to describe *glass structure* at different length scales. Having information about the local bond arrangements of the glass forming or modifying polyhedral will not necessarily complete the description of a glass structure because short-range information must also be coupled with longer range information, including how those polyhedral are linked to form larger structures, whether ordered or disordered, before a proper structural description is formed. Consequently, phosphate glasses can be made with a range of structures, from a cross-linked network of Q^3 tetrahedra (v-P_2O_5) to polymer-like metaphosphate chains of Q^2 tetrahedra to 'invert' glasses

based on small pyrophosphate (Q^1) and orthophosphate (Q^0) anions, depending on the [O]/[P] ratio as set by glass composition.

Vitreous P_2O_5

There are a number of polymorphs of crystalline P_2O_5, including a hexagonal, based on discrete P_4O_{10} molecules and two orthorhombic forms based on helices of PO_4 tetrahedra, each sharing three corners of oxygen bonds [49]. The tetrahedra in each polymorph are linked to three other tetrahedra through bridging (P-O-P) oxygens. The fourth bond is to a terminal oxygen P=O and is significantly shorter than the others, a consequence of its enhanced π-bond character, as confirmed by recent ab initio calculations [52]. In general, the P-TO bond lengths are shorter and the P-BO bond lengths are longer in the glass than in the different crystalline polymorphs.

Some of the details about the Q^3 tetrahedra in v-P_2O_5 can also be obtained by various spectroscopic techniques. Galeener and Mikkelsen reported the first Raman spectra from anhydrous v-P_2O_5. By comparing those spectra with ones collected from various gas phases, they were able to confirm the tetrahedral structure of the phosphate building blocks was associated the ~1390 cm^{-1} Raman peak with the short P-TO bond [53].

In summary, the basic building block for the structure of P_2O_5 glass is the Q^3 tetrahedron, possessing three covalent bridging oxygen bonds to neighbouring tetrahedra, and one short of P-TO bond to terminal oxygen. These tetrahedra are linked to form a three-dimensional network that appears to possess some similarities to the structure of P_4O_{10} molecules found in crystalline H-P_2O_5, although there remain uncertainties as to the details of such extended range ordering. That the density of v-P_2O_5 is intermediate to those of the H- and O-forms of crystalline P_2O_5 indicates that the glass likely contains longer-range structural similarities to both forms.

Binary Phosphate Glasses

The addition of a modifying oxide to v-P_2O_5 results in the creation of NBOs at the expense of BOs. The resulting depolymerisation of the phosphate network with the addition of alkali oxide, R_2O, can be described by the pseudo-reaction [50]:

$$2Q^n + R_2O \rightarrow 2Q^{n-1} \tag{2.4}$$

For binary xR_2O (or R'O) $(1-x)P_2O_5$ glasses (where R_2O is an alkali oxide and R' is an alkaline earth oxide), the concentrations of Q^n tetrahedra in Figure 2.4 generally follow simple predictions based on the glass composition. In the *ultraphosphate* region ($0 \leq x \leq 0.5$), the fraction of Q^2 and Q^3 tetrahedra are given by [50]:

$$f(Q^2) = \frac{x}{1-x} \tag{2.5}$$

$$f(Q^3) = \frac{1-2x}{1-x} \tag{2.6}$$

Anhydrous ultraphosphate glasses must be prepared in sealed ampoules because of the hygroscopicity and volatility of P_2O_5. The reactivity of Q^3 sites to water limits technical usefulness of ultraphosphate glasses even though they possess UV edges at shorter wavelengths compared to silicate glasses [54].

Metaphosphate glasses ($x = 0.50$) have networks based entirely on Q^2 tetrahedra that form chains and rings. The chains and rings are linked by more ionic bonds between various metal cations and the NBOs. Because of the difficulty in obtaining an exact stoichiometry, these compositions are usually more accurately described as long-chained polyphosphates. The term *metaphosphate* is reserved for cyclic anions of the exact $(PO_3^-)_n$ compositions [55].

Polyphosphate glasses ($x > 0.50$) have networks based on Q^2 chains terminated by Q^1 tetrahedra (one BO and three NBOs per tetrahedron). The average chain length becomes progressively shorter as the [O]/[P] ratio increases. At [O]/[P] $= 3.5$ (the pyrophosphate stoichiometry, $x = 0.67$), the network structure is dominated by phosphate dimers, two Q^1 tetrahedra linked by a common BO. Glasses for which [O]/[P] > 3.5 contain isolated Q^0 (orthophosphate units) tetrahedra. Between the metaphosphate ($x = 0.50$) and pyrophosphate ($x = 0.67$) boundaries, the fraction of Q^1 and Q^2 tetrahedra are given by [50]:

$$f(Q^1) = \frac{2x-1}{1-x} \tag{2.7}$$

$$f(Q^2) = \frac{2-3x}{1-x} \tag{2.8}$$

Between the pyrophosphate (x=0.67) and orthophosphate (x=0.75) boundaries, the fraction of Q^0 and Q^1 tetrahedra are given by:

$$f(Q^0) = \frac{3x-2}{1-x} \qquad\qquad (2.9)$$

$$f(Q^1) = \frac{3-4x}{1-x} \qquad\qquad (2.10)$$

Glass formation in binary xR_2O (or R'O) $(1-x)P_2O_5$ systems is typically limited to $x < 0.60$ (mole fraction) for conventional melt processing. Rapid quenching techniques have yielded Li-phosphate glasses with x as large as 0.70 ([O]/[P] ~ 3.67), having structures based on Q^1 and Q^0 tetrahedra [50]. Such glasses do not have a continuous random network of glass-forming polyhedra, as described by Zachariasen [39]. Instead, the glass structure consists of isolated tetrahedra and small molecular fragments linked through their NBOs by smaller valence cations. For binary glasses, the bridging-to-terminal oxygen ratio, for $0 \leq x \leq 0.75$, depends on composition according to:

$$BO/TO = 0.5(3 - 4x) \qquad\qquad (2.11)$$

The predictions represented by equations (2.4 - 2.11) can be tested using energy-dispersive X-ray spectroscopy, X-ray photoelectron spectroscopy and chromatography to provide quantitative descriptions of the phosphate glass network structures.

2.6   Preparation of phosphate glasses

Different techniques have been used to prepare phosphate glass by physical and chemical methods. Some of the methods are thermal evaporation [56], chemical vapour deposition [57], electrolytic decomposition [58], melt quenching [59], sol gel technique [60] and so forth. From listed, melt quench technique is the simplest and most widely used for the preparation of phosphate glass because of the several reasons; the glass preparation and handling are very easy, speedy preparations of innumerable compositions of the glasses are possible, bulk glasses can be prepared and simultaneously, both amorphous and crystalline nature can be obtained in the same melt. However, melt quench method gives unhomogenized composition within

the glasses. Hence, wet melting technique was used, which was modified from the melt quench technique to prepare phosphate glasses for RPLGD.

2.6.1 Wet Melting Method

Glass is prepared by a cooling process of the molten liquid form of the mixed materials compound. Cooling rate is a critical factor in determining glass phase formation with different phases for different material compounds and preparation method. For example, certain glass formers such as SiO_2, P_2O_5, B_2O_3 and so forth, will form glassy phase even under conditions of slow cooling ($1Ks^{-1}$) whereas to get metallic glasses cooling rates of the order of 104-106 Ks^{-1} are required [61].

The wet melting process include melting of material in suitable crucibles made of alloy (Pt-Rh, alumina, zirconia etc.) followed by pouring of the melt to the moulder shape. Effective cooling can be achieved by quenching the melt immediately after removing from the furnace and placing it in between conducting materials like copper or brass plates or pouring in graphite moulds.

A batch is prepared by mixing predetermined amounts of pulverized raw materials with water to attain the desired property in the crucible and placed in electrical furnace space, made of sodium carbide to be fused into a liquid at high temperature. Generally, the molten phosphate glass is kept at the temperature which corresponds to a viscosity of 1200-1300 °C for one hour in order to remove tiny bubbles and to enhance the homogenization of the melt through convection and the inter-diffusion of the constituent atoms.

The formation of a melt into a desired shape is carried out at a temperature corresponding to the viscosity of phosphate glass, by applying forming methods such as casting into a moulder shape. Hereafter, the high flexibility in the geometry of products, which is the most distinctive feature of this technique, is possible. Most of the formed glasses are usually annealed in a temperature range near the T_g (350-400 ºC) for phosphate glass to remove any thermal stresses which are developed during the forming and subsequent cooling due to the low thermal conductivity of a glass [62]. The advantage of this method is the large flexibility of composition.

2.7   Radiophotoluminescence glass dosimeter with silver

Radiophotoluminescence glass dosimeter uses glass compound as the luminescent material and applies different excitation method along with different readout technique. The colour centres were structured at the silver activated phosphate glass. The numbers of ionic silver relate to energy levels in colour centres and the numbers of electron trap(s). The numbers of electron trap(s) increase with increasing numbers of ionic silvers. Silver were chosen as the activator because it can interact with PO_4^{2-} base composition and produces colour centre within the forbidden band. Therefore, the formation and thermal tolerance of RPL centres are related to the molecular structure of phosphate glass. The characteristics of RPL centres can be partially controlled by the content of the linked metal cations such as alkali metals, alkali earths and aluminium.

2.8   Dosimeter

Radiation dosimeter is an instrument or system that measures either directly or indirectly, the quantities exposure, kerma (kinetic energy released per unit mass), absorbed dose or equivalent dose, or their time derivatives (rates) or related quantities of ionizing radiation. A dosimeter along with its reader is referred to as a dosimetry system. Measurement of a dosimetric quantity is the process of finding the value of the quantity experimentally using dosimetry systems. The result of measurement is the value of a dosimetric quantity expressed as the product of a numerical value with an appropriate unit.

To function as a radiation dosimeter, the dosimeter must possess at least one physical effect that is a function of the measured dosimetric quantity and can be used for radiation dosimetry with proper calibration. In order to be useful, radiation dosimeters must exhibit several desirable characteristics such as accuracy and precision, dose or dose-rate dependence, linearity, directional dependence, energy response and spatial resolution. There are two main uses of dosimeter; for human radiation protection and for environmental measurement such as in both medical and industrial processes.

2.8.1 Solid state dosimetry

Solid state dosimeters are useful for three main reasons; 1) Their high density (800 to 4000 times more atoms per cm^3 than air) can lead to small sizes, e.g. in semiconducting devices, 2) Changes induced in solids by radiation may persist for long periods, enabling total dose to be estimated at a convenient time after the irradiation and 3) Solid systems showing an obvious visible change are useful for localizing beams of radiation and for enabling spatial variations in dosage to be measured.

So far, some types of solid state dosimeter or luminescent detectors have been developed not only for personal monitoring but also for environmental background radiation monitoring. For instance, a thermoluminescence (TL) dosimeter has been studied to monitor the environmental background radiation [63]. Recently, new passive solid state dosimeters utilizing optically stimulated luminescence (OSL), direct ion storage (DIS) and radiophotoluminescence (RPL) phenomena have been developed to monitor the personal and environmental radiation [63].

2.8.2 Radio Photoluminescent Glass Dosimeter

Development of RPLGD Material

In 1949, Wely, Schulman, Ginther, and Evans manufactured the first RPLGD system [64]. Schulman applied this system in radiation dose measurement in 1951 [6]. The luminescent material used by Schulman was a compound glass of 25% of KPO_3, 25% of $Ba(PO_3)_2$ and 50% of $Al(PO_3)_2$, with proper amount of $AgPO_3$ to form silver activated phosphate glass. It is very difficult to measure dose under 1 mGy with Schulman's RPLGD system, because it has a high pre-dose. Pre-dose is the phosphorescence light emitted from RPLGD without any irradiation and excitation process. It is the lowest irradiation dose can be measure with RPLGD. Besides, because of the pre-mature luminescence measurement technique and the poor quality of excitation source for colour centres, the measurement accuracy with Schulman's RPLGD is very poor.

In the early 1960s, fluoro glass dosimeter (FGD) material was further developed. The glass consisted of phosphorus, aluminum, lithium, silver,

magnesium, and barium oxides. The property of the early lithium borate glasses was their naturally low energy dependence, but there were also handling problems due to the composition of the material [65]. The kinetics of the material is dependent on the element compounds; for example, after irradiation, radiation energy accumulated more rapidly in the basic element of $LiPO_3$ than in $Al(PO_3)_3$ material [65]. It was also observed that reducing the content of the alkali metals decreased the sensitivity of RPL dosimeters due to low silver ion mobility in glasses [66]. The concentration of silver was much higher in early glasses than in more recently used materials [66]. The concentration of silver and sodium in the basic element material is responsible for the background luminescence (pre-dose) in the material [66]. Some magnesium oxide (MgO) and aluminium oxide (Al_2O_3) are added to provide for a better chemical durability. Besides, boric oxide helps to reduce melting temperatures, increase thermal resistance and mechanical strength, and enhance aqueous and chemical durability.

Sensitivity, pre-dose, and energy dependence were subsequently improved with advantages to personnel monitoring. The improvements were necessary because the early glasses were not suitable for low-dose measurements [65]. The more recently used glass material was improved by replacing lithium with sodium [67]. Likewise, the element composition of the glass material affects the capability of UV spectrum to penetrate the glass material. Therefore, reduced silver and aluminum concentrations could improve the excitation of luminescent centres by UV laser [66].

Radiophotoluminescence Mechanism of RPLGD

Radiophotoluminescence (RPL) dosimetry is based on luminescence phenomena. Luminescence is divided into two phenomena; phosphorescence and fluorescence. Phosphorescence decay to ground state is considerably longer than that of the fluorescence. The luminescence process in RPL is fluorescence. Fluorescence is defined as luminescence that persists only for as long as the exciting radiation is present, while the after-glow if detectable by the human eye after the cessation of excitation is called phosphorescence [5].

RPLGD is a mixture of inorganic amorphous solid and does not have lattice structure and lattice luminescence centres (molecular-level structures). Therefore the

RPL model can be establish based on the energy of the excitation source and the energy of the released visible light. Moreover, the colour or luminescence centres were structured at the silver activated phosphate glass. The numbers of silver compounds are relating to energy levels in colour centres and the numbers of electron traps. The numbers of electron traps increase with increasing numbers of silver compounds [18]. However, excessive numbers of silver content decrease the penetration efficiency of the UV light and increases energy dependence. Therefore, a proper ratio of silver composition is required for the best luminescence and excitation efficiency.

When the RPLGD is irradiated, the electron-hole pairs are formed and the mechanisms are shown in Figure 2.5(A). The electrons (e^-) lift up into the conduction band where some of them are immediately trapped by positively charged silver ions (Ag^+) and formed a colour centres. Holes (h^+) are trapped by negatively charged phosphate ions (PO_4^-). Another colour centre is formed by hole-phosphate compounds towards the positively charged silver ions [18] as shown in Figure 2.5(B). The forbidden energy level close to the conduction band is called electron trap while the one which close to the valence band is called hole-trap as shown in Figure 2.5(C).

The absorbed energy in the material is directly proportional to the number of traps formed [18]. The RPLGD which are metastable absorption and emission bands are created by ionization radiation permitting the quantification of the dose delivered to the glass [18]. After excitation of the luminescence centres by UV light with a specific wavelength, a visible orange light of fluorescence emission is observed with wavelength between 600-700 nm as shown in Figure 2.5(C). The intensity of the fluorescence emission is proportional to the dose delivered to the dosimeter [18]. From the emitted lights, the energy gap between the excited energy levels which electrons jump to and the energy levels at colour centres is between 1.78 and 2.07 eV using band Plank's relation equation [5]. The dosimeters can be reused after an annealing procedure. The duration time between 30-90 min of annealing treatment at 370 °C will empty the dose in the dosimeter by releasing electrons from the traps back to the valence band [68] as shown in Figure 2.5(D). The annealing time is dependent on the dose level in the dosimeter [18].
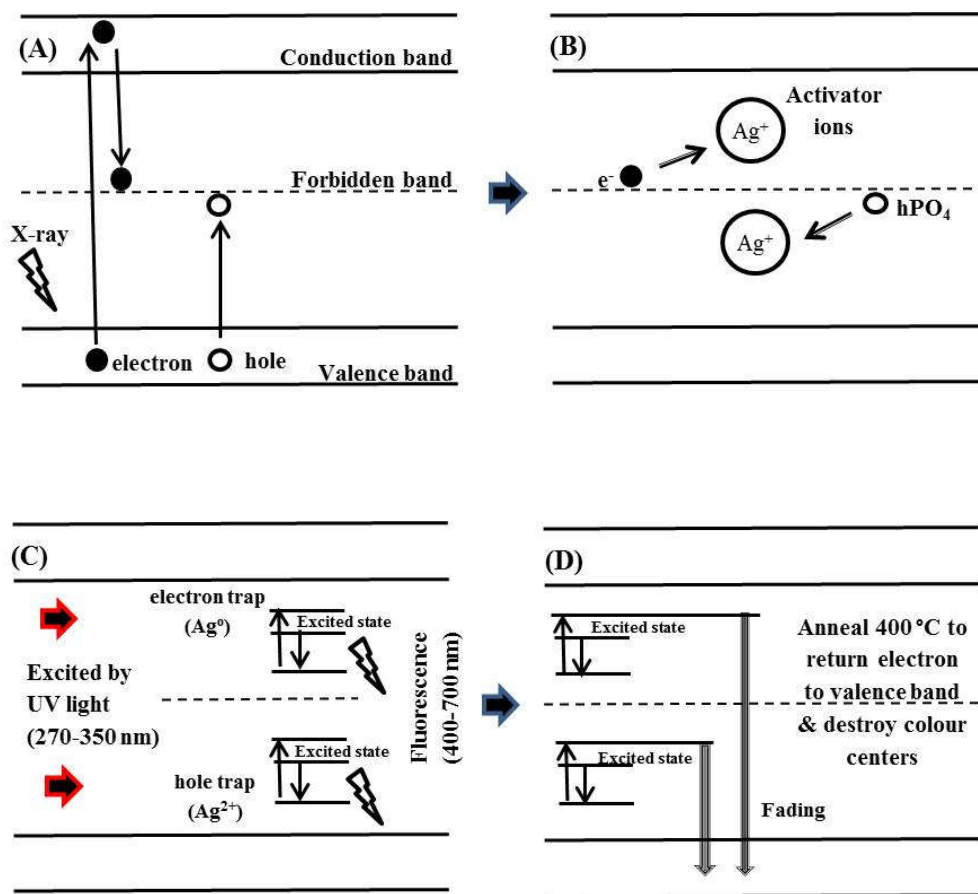
Figure 2.5: A) and B) Schematic of stable colour centres (Ag°, Ag²⁺) creation of by X-ray, C) Fluorescence emission after UV excitation and D) Re-empty dosimeters by annealing at 400 °C [5 & 69].

Luminescent Centres in RPLGD Material

The luminescence processes of RPLGD can be divided into two parts: the processes mainly related to the phosphor host and silver activator. RPLGD material contains of a glass substrate incorporating with silver (Ag^+) and phosphate (PO_4^{3-}) ions. The location of these ions represents as defects in the lattice of the dosimeter glass [18]. Irradiation releases electrons in the dosimeter material resulting in electron-hole pairs which are caught by Ag^+ and PO_4^- ions, generating colour centres such as Ag° and Ag²⁺in the forbidden band as shown in Figure 2.6, which are defined as electron trap:

$$Ag\text{-}PO_4 \rightarrow Ag^+ + PO_4^- \tag{2.12}$$

$$PO_4^- + h^+ \rightarrow hPO_4 \tag{2.13}$$

$$Ag^+ + e^- \rightarrow Ag^o \tag{2.14}$$

and for the hole trap as [70]:

$$Ag^+ + hPO_4 \rightarrow Ag^{2+} + PO_4 \tag{2.15}$$

The Ag-PO_4 in RPLGD can be viewed as Ag^+ and PO_4^-. When the tetrahedron of PO_4^- is exposed to the radiation, it loses one electron and forms a positron hole, hPO_4. The electron released from the PO_4^- will combine with Ag^+ to form an Ag^o. Similarly, hPO_4 will combine with Ag^+ to become an Ag^{2+}.
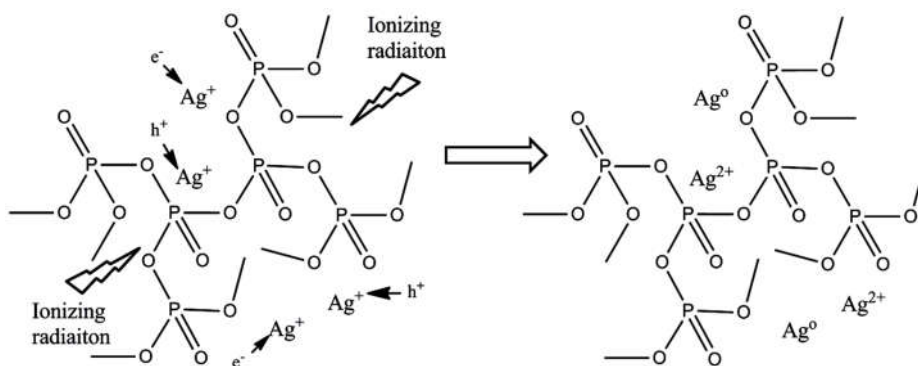
Figure 2.6: RPLGD material consists of a glass substrate incorporating with silver (Ag^+) and phosphate (PO_4^{3-}) ions. Schematic representation of stable colour centres (Ag^{2+}, Ag^o) generated in phosphate glass by ionization radiation [5].

Huang and Hsu [5] mentioned in their article that there are many continuous energy levels at the colour centres of the RPLGD, as shown in figure 2.7. It shows the electrons in the valence band are excited to the conduction band after irradiation processes. When electrons return to the valence band, portions of electrons are captured by the electron traps located at P shell and Q shell to form colour centres. RPLGD is manufactured via the process of melting various compounds under high temperature. Hence, the colour centres of PRLGD are not built at the lattice. Therefore, the colour centres of RPLGD were structured among the orbital electrons in the compound. The various continuous energy levels are formed with different bonding structures among elements. However, the diffusion flux occurs by silver ions in the phosphate glass composition as describe on Fick's first law. It postulates

that the flux goes from a region of high concentration to a region of low concentration across a concentration gradient.
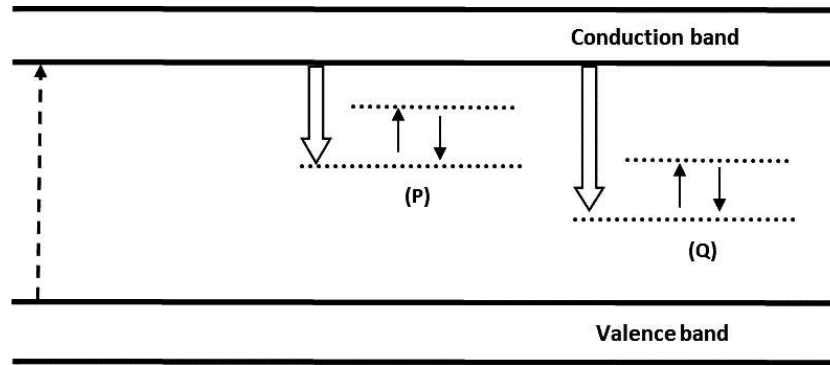
Figure 2.7: Continuous energy levels in RPLGD colour centres [5].

As previous discussion, the traps are stable in the sense that the energy required to remove the electron or hole from the trap to the conduction or valence band must be much larger than the binding energy of the electron in the trap. The negligible fading in a dose absorbed into the RPL dosimeter material is caused by the colour centres of Ag^o and Ag^{2+} ion [18 & 70]. During the irradiation of the silver-activated phosphate glass, colour centres begin to form. However, the formation of these centres does not appear immediately, because some of the electrons are caught in ineffective traps which do not produce luminescence. After several days stored at room temperature, 90% to 99% of the total dose of the dosimeter is reached, respectively. This phenomenon is known as the build-up effect and requires a stabilization treatment by heating in 70-100 °C for one hour [68]. The electrons diffuse faster than holes in the glass material, and the accumulation speed of Ag^o is thus higher than that of Ag^{2+}. The heating treatment causes faster accumulation of Ag^{2+} in the irradiated dosimeter and is responsible for the creation of the main RPL centres [71]. After the heating procedure, the luminescent centres remain relatively constant in room temperature over an extended period, and dosimeters permit repeated measurements free from the fading effect [18].

Stable colour centres can absorb and release energy; this is used as the principle in the dosimeter readout system [18]. When the colour centres are irradiated

by pulsed UV laser (270-350 nm), electrons are excited into a higher energy state. The centres return to a stable energy level by emitting visible light (420-700 nm) known as fluorescence [70]. The fluorescence is measured with a photomultiplier system, and the amount of fluorescence is directly proportional to the dose absorbed into the dosimeter [71]. The electrons in colour centres will not return to the valence band of the glass material directly because the energy gained by electrons from the UV light is not high enough to let electron escape from colour centres.

Energy Dependence and Compensation

In radiology, relatively low energies between 10 keV and 140 keV are used. At these energies, the relative response of the dosimeter is high because of the strong dependence between the effective atomic number and the photoelectric effect [16]. A minimal energy dependence or deviation of response with changing energy is required from the dosimeter. This is particularly required in the dose measurement of the continuous spectrum. The relative energy response of the dosimeter material can be expressed as the ratio between peak and minimum response energy [17]. Usually, the minimum response energy is defined at 1 MeV at the Co-60 energy of 1.33 MeV. The peak response is the highest dose determined with the energy spectrum [17]. The peak response is determined in RPLGD glass material at about 30-45 keV [17]. The energy dependence of the dosimeter is defined as the ratio of the absorbed energy at two reference points on the energy axis.

The mass energy absorption coefficient of the RPLGD is higher than that of soft tissue and almost similar to bone in the energy region used in radiology [72]. If the mass energy absorption coefficients for mixtures and compounds are assumed to be homogenous, they are calculated as:

$$\frac{\mu_{en}}{p} = \sum_i W_i \left(\frac{\mu_{en}}{p}\right)i \tag{2.16}$$

where W_i is the fraction by weight of the ith atomic constituent and $(\frac{\mu_{en}}{p})I$ values are from the NIST Standard Reference Database, 126 NISTIR 5632 [73].

Although previously used dosimeter materials have been improved, they still have a higher effective atomic number (Z_{eff} =12.0) than soft tissue (Z_{eff} =7.4). The

interaction between radiation and RPLGD material occurs through the photoelectric effect. The ratio of the mass energy absorption coefficient is determined as being up to four-fold between RPLGD material and water [74] and between RPLGD material and air [75].

Dose measurement range

The RPLGD material has a linear relationship between the fluorescence intensity and the absorbed dose caused by ionizing radiation [16]. The low dose limit is dependent on the pre-dose, which is meant to quantify the level of background effects that are inherent within the glass. The challenge is to separate the RPL emission band from the unwanted predose luminescence. The predose is a function of both glass and reader technique [18].

In the 1990s, an automatic readout system was created, which uses pulsed UV laser excitation and pre-dose suppression [16]. After the development of the readout system, the detection of small doses in the 10-30 µGy range was possible with sufficient accuracy [76]. The technique is based on electronic discrimination of signals from the pre-dose and the actual dose due to their different fluorescence decay times [76]. After pulsed UV laser (337.1 nm) excitation, electrons return to a stable energy level in the luminescence centre by emitting fluorescence light (620 nm). The fluorescence emission is imaged by a lens onto a photomultiplier (PM) as shown in Figure 2.8. A timing circuit triggers the main RPL emission, measuring time at 2-7 µs (t_1) and long decay pre-dose at 40-45 µs (t_2) as shown in Figure 2.9. RPL emission (*M*) was calculated as:

$$M = \int_{t_1}^{1} I(t) - fps \int_{t_2}^{1} I(t)dt \tag{2.17}$$

where *I(t)* is fluorescence intensity at time t and *fps* is a correction factor for the pre-dose in the glass itself [77].
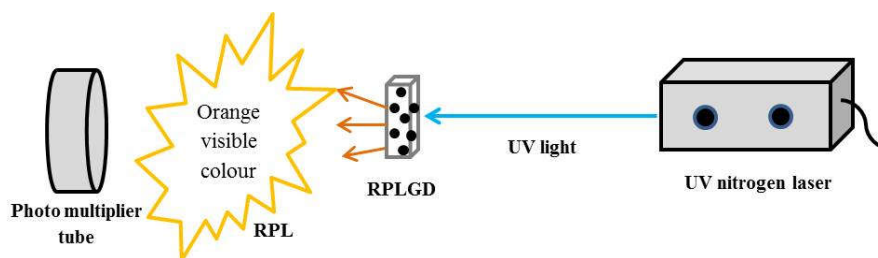
Figure 2.8: Radiophotoluminescent dosimeter system [78].

The dose is reported to be linear up to at least 30 Gy, becoming sub linear at higher doses [18]. The point where sub linearity occurs depends on the glass dimensions and material, the reader technique, and the spectral region in which the fluorescence is measured [16].
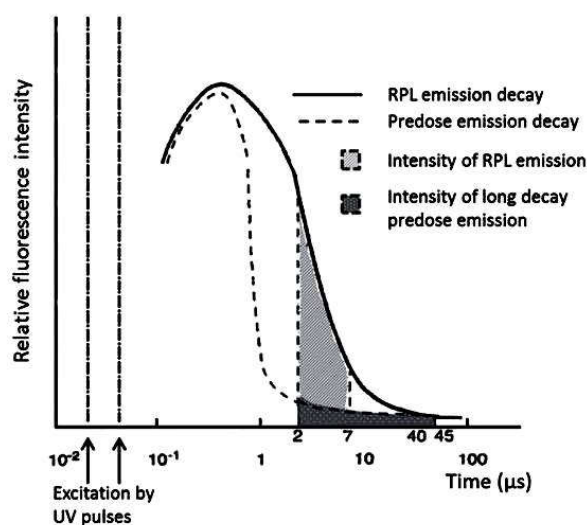
Figure 2.9: Schematic representation of excitation by UV pulses, predose and RPL emission and their various fluorescence decay times [78 & 79].

2.8.3   Dosimetric Properties

An understanding of the dosimetric properties of a glass dosimeter is crucial to its successful employment in the field. It is a prime consideration to potential users in order to justify the use of glass dosimetry. Although progress has taken place in the background, with more recent work being involved with developments in system automation and reader design, it has been founded on a comprehensive understanding of the fundamental dosimetric properties of glass and other luminescent materials.

Kinetics

The term of kinetics is used to describe the movement or growth and decay of the colour centres formed by the ionizing radiation. The effect of these changes is to alter the efficiency or sensitivity of the dosimeter [18]. The signal will vary as function of time between exposure and read-out in a non-linear measurement and is affected by several other factors.

Band model

Theoretical band models such as the one proposed by Becker in 1965 have been put forward to describe the migration and formation of colour centres. Figure 2.10 demonstrates the model principle, where the following processes are assumed to take place. The action of ionizing radiation lifts electrons up into the conduction band where some of them are immediately trapped by the positively charged silver ions to form Ag^o centres which are colour centres. A proportion of the electrons is at first held in traps of a variety that are ineffectual for glass fluorescence but which later drift, as a result of the absorption of thermal energy, to form additional RPL centres, so causing a signal build-up. This model explains why a change in the ratio of the number of colour centres to the number of ineffective traps is one of the factors that affect the build-up rate.

This model, while not being very specific in identifying the actual centres involved, is nevertheless consistent with the later findings of Yokota and Imagawa, who revealed the structure of the principle RPL centres and the mechanism of their formation [19].
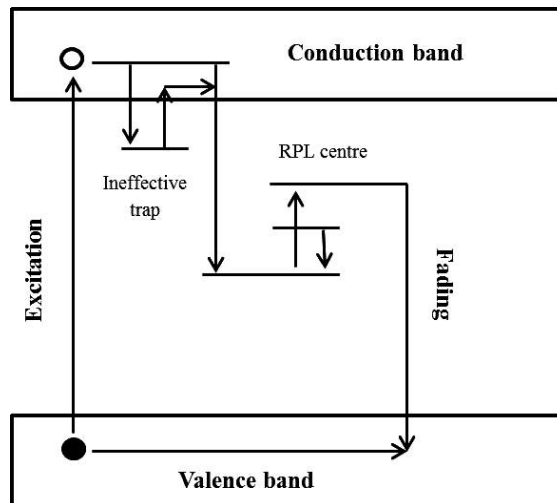
Figure 2.10: Simplified theoretical band model for signal build-up and fading [80].

Build-up Effects

Before irradiation, the glass dosimeter consists principally of a substrate incorporating positively charged of activator such as silver ions (Ag$^+$) and negatively charged of host compound such as phosphate ions (PO$_4^{3-}$). The locations of these ions in the lattice are represents as defects and are able to absorb and release energy by becoming excited and de-excited accordingly. These defects are referred to as colour centres; because they exhibit luminescence and they possess their own absorption and emission spectra, typically between 230 and 380 nm spectrum bands respectively [80].

Upon radiation, the formation of colour centres begins, but the final number of colour centres does not form immediately because of insufficient energy. The various type of center responsible for RPL phenomenon appear at varying rates and are under the influence of many factors such as heating treatment [80].

Fading Effects

The same factors that influence build-up apply to fading. A higher ambient storage temperature increases the recombination rate of trapped electrons with holes in the valence band, thereby destroying the colour centres and preventing the maximum signal level that would have occurred at a lower temperature. To prevent significant fading of the glasses, elevated temperatures are avoided for extended

periods of time. If glasses are given a stabilization treatment of the RPL and then turning down to room temperature, the RPL will be stable over extended periods [80].

The effect of silver concentration upon fading is similar to the effect upon build-up. Therefore, higher silver concentrations induce a more rapid build-up, but this is followed by an increased fading rate. However, at lower silver concentrations, the signal level would have achieved more slowly but it's retained longer, which overall results in larger RPL maxima. After stabilization treatment, the effect is much less noticeable, so that only those glasses with the higher silver content exhibit fading after several weeks. The fading effect also has related to the base component of the glass but it is difficult to predict the kinetics of different base compositions since particular metals phosphates have a greater quenching effect [80].

Temperature Effects

Temperature is an important factor that affects the rate of build-up and fading process. On the basis of the RPLGD, the higher the ambient temperature, the more energy, in the form of increased amplitude of lattice vibrations, is available to transfer free electrons to colour centres. The storage temperatures affect the RPL signal and it is evident that increasing the storage temperature produces a more rapid build-up, at least up to about 100-150 ºC. However, fading effects start to take over significantly after day one to about 100 °C, indicating that the centres are not thermally stable. At even higher temperatures (~200 °C) the RPL does not reach the same level as at 100 °C before being reduced considerably by fading losses. At 300 °C there is no build-up and at 400 °C the RPL is promptly quenched but begins to reform slowly, demonstrating the build-up of a new species of center. Additionally, the effect of temperature on annealing process has no effect on the pre-dose, sensitivity or kinetic properties, except perhaps if either too high the annealing temperature is used or if the dosimeter has been exposed to very high dose levels [81].

Compositional Effects

Another prominent factor which controls the kinetics of a particular glass is its chemical composition. This is usually considered in two parts, activator and base composition in which the activator lies. Besides, the requirement of a fast build-up would dictate a relatively high activator concentration, but the fading rate is also

correspondingly higher. However, too high concentration of activator's concentration reduces sensitivity because there is then a larger density of centres from which recombination of holes and electrons can take place. Therefore, the activator concentration must be sufficiently high to provide a large enough population of potential colour centres, yet low enough to avoid introducing any of the aforementioned problems [18].

In practical, the choice of matrix or base for the activated silver has a marked effect on the build-up. Lithium (Li) content makes the RPL signal reach a maximum quickly in comparison with no Li compound. With a higher concentration of aluminium (Al), the build-up is slower indicating the importance of base compositions. Base composition affects build-up due to the various diffusion rates of the liberated electrons through the lattice. Different bonding arrangements and the specific grouping of localized charges within the lattice will modify the electrostatic forces causing the electron drift. However, an analysis of the component forces within a glass would be very involved.

Bleaching Effects

The effect of optical radiation on glasses will depend mainly upon the pre-irradiation of the glass. As with increased temperature, infrared (IR) radiation increases both build-up and fading rates because it stimulates lattice vibrations, but light of normal ambient intensity has little or no effect unless it is directed in such a way as to raise the temperature of the surrounding significantly. UV radiation which used for fluorometric evaluation does cause a slow destruction of the centres (bleaching), but since the total time for which the glass is exposed to the stimulating radiation is small, its effect can be ignored. Continued exposure to bright sunlight, however, may cause a considerable loss in RPL intensity due to the joint effect of the UV and IR components [80]. However, indirect natural window-glass-filtered room illumination causes no observable effects and neither do the usual sources of artificial light such as tungsten and fluorescent strips. It has also been observed [80] that the bleaching caused by a constant-intensity UV source is quite rapid at first but becomes smaller with increased time.

Overall Stability

Long term studies by Cheka on three commercial dosimeter glasses showed excellent stability at room temperature over period between 1 hour and about one year after exposure and also between 6 hours and after 10 years [82 & 83]. He found that during 10 years of storage at room temperature, readings from the two low-dose glasses remained constant within ±10% if measures between 2 hours and several years after exposure. The maximum RPL was reached after 10 days, with all readings normalized after one day.

In any occurrence, stabilization has a levelling effect, such that once it's completed; the gradual fluctuations with time are reduced, thereby allowing long-term storage of dosed glasses. Certainly the practicalities of implementing the development procedure will not detract from its use, since it can easily be conducted in larger batches and is akin to developing monitoring films.

Chapter 3

3. Materials and General Methods

3.1 Introduction

This research was carried out at the Department of Nanoscale Science and Technology of Flinders University, Australia and Nuclear Science Department, National University of Malaysia (UKM), Malaysia. A brief overview of the experimental techniques that have been employed for the preparation and characterization of radio-photoluminescence glass dosimeter (RPLGD) is discussed in this chapter. The relevant theories and working principles are also elaborated. First preparations of glasses including silver nanoparticles and their subsequent conversion to glass are described followed by methods used to characterize them.

The various properties of the RPLGD were determined. Thermal properties were studied using differential scanning calorimeter (DSC) instruments and mechanical properties using Rockwell hardness tester. Some optical properties of phosphate glasses were measured using Ultraviolet-Visible (UV-Vis) and photoluminescence spectrometers. The structural and chemical bonding characterization of glasses was carried out using X-ray diffractometer (XRD) and Fourier-transform infrared (FTIR) spectroscopies.

3.2 Chemicals and reagents

All chemicals were purchased from chemical supplier in Australia and Malaysia and have been used as received without further purification as listed in Table 3.1.

Table 3.1: List of chemicals and reagents

Chemical name	Chemical formula	CAS number	Molar mass (g/mol)	Supplier	Purity (%)
Silver nitrate	$AgNO_3$	7761-88-8	169.87	Sigma-Aldrich	≥ 99.0
Phosphorus pentoxide	P_2O_5	1314-56-3	141.96	Acros organics	≥ 99.0
Sodium hydroxide	NaOH	1310-73-2	40.00	Fluka	≥ 97.0
Lithium carbonate	Li_2CO_3	554-13-2	73.89	Merck	≥ 99.0
Aluminum hydroxide	$Al(OH)_3$	21645-51-2	78.00	Merck	≥ 98.0
Sodium nitrate	$NaNO_3$	7631-99-4	84.99	Merck	≥ 99.0
Titanium dioxide	TiO_2	13463-67-7	79.87	Sigma-Aldrich	≥ 98.0
(3-Mercaptopropyl) trimethoxysilane	$C_6H_{16}O_3SSi$	4420-74-0	196.34	Sigma-Aldrich	≥ 95.0
Boric acid	H_3BO_3	10043-35-3	61.83	Merck	≥ 98.0
Hydrogen peroxide	H_2O_2	7722-84-1	34.01	Chem-Supply	30 wt.%
Sodium borohydride	$NaBH_4$	16940-66-2	37.87	Sigma-Aldrich	≥ 97.0
Trisodium citrate	$Na_3C_6H_5O_7$	6132-04-3	294.10	Sigma-Aldrich	≥ 99.5
Potassium bromide	KBr	7758-02-3	119.00	Sigma-Aldrich	≥ 99.0
Poly(sodium 4-styrenesulfonate)	$(C_8H_7NaO_3S)_n$	25704-18-1	70 000	Sigma-Aldrich	≥ 99.0
Poly(ethyleneimine)	$(C_2H_5N)_n$	9002-98-6	750000	Sigma-Aldrich	50% w/v

3.3   Methodology

Methodology part were divided into three part, which are 1) synthesis silver nanoparticles, 2) preparation of phosphate glass with different base component and 3) preparation of phosphate glass with different sizes of silver activator. The flowchart methodology of this research is available in the Figure 3.1.
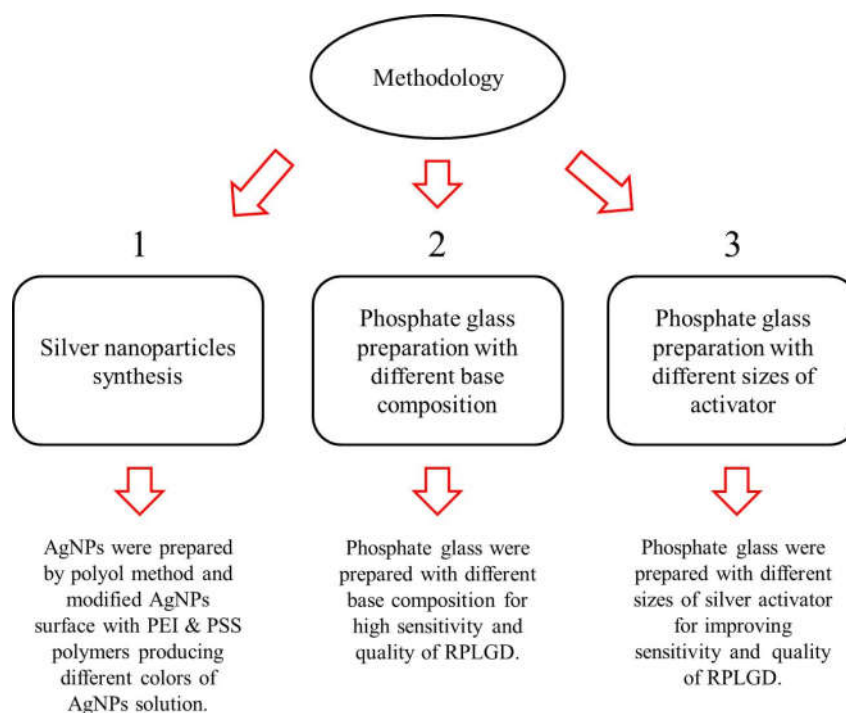
Figure 3.1: The flowchart methodology of this research

3.3.1 Silver nanoparticles synthesis

Before synthesizing the AgNPs-doped phosphate glass, silver nanoparticles (AgNPs) was firstly prepared. To obtain the AgNPs, aqueous mixtures of silver nitrate, $AgNO_3$ (0.375 mM, 180 mL), Trisodium citrate, $Na_3C_6H_5O_7$ (12.5 mM, 72 mL) and hydrogen peroxide, H_2O_2 (50 mM, 180 mL) were prepared. The bulk sample was divided into two parts and a potassium bromide, KBr solutions (1 mM; 180 & 360 μL) was added to each solution and stirred for one hour to make different sizes of AgNPs, respectively. Subsequently, sodium borohydride, $NaBH_4$ (5 mM, 25-30 mL) was injected to each mixed solution and the reaction was initiated. The stirring was continued for another one hour to complete their reaction. The different colour of solution products roughly confirms the formation of AgNPs with different sizes [84]. The synthesized AgNPs dispersions showed no changes in the position of their optical absorption bands and intensity even after two months of storage at room conditions. The AgNPs produced were characterized and their properties were discussed in details in the next chapter.

3.3.2 Phosphate glass preparation

Phosphate glass for the solid-state dosimetry was prepared from reagent grade powders of anhydrous P_2O_5 (60-90 wt.%), Li_2CO_3 (0-15 wt.%), $Al(OH)_3$ (0-10 wt.%), $NaNO_3$ (0-15 wt.%), MgO (0-2.5 wt.%), TiO_2 and H_3BO_3 (0-10 wt.%). Silver metals (0-10 wt. %) was used as the main component for the RPLGDs. Ag-doped phosphate glasses were prepared by the wet melting method. The weight chemical composition of the glass dosimeters was weighted using a digital weighing machine with an accuracy of ±0.01 g, then mixed with deionized (DI) water and the well-mixed liquid batch was preheated at 120 ºC for 24 h in an alumina crucible to evaporate water. After that, the liquid batch was melted in an alumina crucible which was placed in an electrical heated furnace in atmosphere. Depending on the chemical composition of glass compounds, the melting temperature was between 1200 and 1300 ºC. Systematically, at a heating rate of about 10 ºC/min, the temperature was gradually increased up to 600 ºC and kept at this temperature for 5 h for calcination process. Once the mixture was liquidized, the temperature was then increased again to 1200-1300⁰C and left for one hour to obtain the appropriate viscosity. After the refining process, the molten liquid was cast into a preheated cylindrical shape graphite mold which had been preheated at 400 °C for 30 min. At this point it then takes 6 hours to complete the annealing process at 360 °C in a second furnace to remove thermal strains in the glass. Finally, the resulting glass was polished and cut for the required measurements. All the detailed steps are discussed below.

3.4 Wet Melting Method

All the phosphate glass samples with different chemical composition and different sizes of silver particles in the present work were prepared by wet melting method. To obtain homogeneous, transparent and bubbles free glasses, a four-step procedure was used; dilution, calcination, melt quenching and annealing process and these are discussed in the following section.

3.4.1 Dilution

Starting batches were prepared by weighing calculated amounts of initial precursors based on the composition of the glass using a digital weighing machine

with an accuracy of ±0.01 g. Analytical grade reagents in the form of oxides, phosphates, nitrates or carbonates were used as starting precursors. The reagent powder (30-40 g batch) was thoroughly mixed together using DI water and the well-mixed liquid batch was preheated at 120 ºC for 24 h in an alumina crucible to evaporate water before calcination process.

3.4.2 Calcination

Calcination is a process to convert precursors into their respective oxides. This process was carried out in an electrical heating furnace having a programmable of proportional, integral and derivative (PID) temperature controller (MTI corporation: KSL-1200X) with a temperature accuracy of ± 0.5 °C. An exhaust system is connected to the furnace for removing gases like NO_2, CO_2 and NH_3 during calcination. For calcination, each batch samples were heated in a furnace at a controlled rate (1-3°C/min) to respective decomposition temperatures (600-800 °C) of various precursors. A dwell time (5-10 h) was provided at each decomposition temperature to allow a complete calcination. After the calcination, measurement of weight loss ascertained a proper decomposition of the precursors. If weight loss was less than expected, indicating an incomplete conversion of the precursors to oxides, then the batch was re-calcined in the same manner process. Figure 3.2 shows the furnace uses for calcination process.

Figure 3.2: Electrical furnace model KSL-1200X for calcination and annealing process

3.4.3   Melt quenching

The calcined batch was melted in an alumina crucible using another electrical box furnace (Berkeley-Scientific 1700 °C) as shown in Figure 3.3. To prevent the volatilization of precursors, the crucible was covered with an alumina lid. The glass batch was melted in an air ambient, at temperatures ranging from 1200 °C to 1300 °C depending on the chemical compositions. The melting temperature of glass is decided such that melt viscosity at this temperature is low enough to allow easy pouring. The glass melt was held for one hour, for thorough mixing and homogenization. When the glass melt was thoroughly homogenized and attained a desirable viscosity, it was poured into preheated graphite molds to obtain the glasses in the bulk form

Figure 3.3:   **Electrical furnace model Berkeley-Scientific 1700 °C for melting process**

3.4.4   Annealing

Quenched phosphate glasses generally have thermal stresses due to the thermal shock during the quenching process. Therefore, annealing is necessary to relieve the thermal stresses in the melt quenched glasses. Generally annealing is carried out at near T_g (generally 10-20 °C below T_g) to allow a rapid removal of

thermal stresses. In an annealing procedure, the glass is held at a constant temperature for some time period and cooled to room temperature at a slower rate. In the present work glasses were annealed in an annealing furnace same as calcination furnace (KSL-1200X), in which temperature is control precisely by a PID temperature controller. For annealing, the melt quenched glasses in graphite molds were immediately transferred to the preheated annealing furnace. Annealing was carried out at 350-370 °C, usually 5 to 12 hours depending upon the glass composition to relieve the thermal stresses, generated during quenching. The annealed glasses were then cooled to room temperature at the rate of 10-20 °C/h and switch off the furnace once everything was cooled down.

3.5 Application

All RPLGD samples were irradiated with γ-radiation, performed using a Co-60 source delivered at 1.8 kGy/h (27/10/2014) by Gamma cell 220 excel as shown in Figure 3.4. In this part, the samples were irradiated with different level of absorbed dose in the range of 5 Gy to 2 kGy for personal and working area RPLGD dose requirement.

Figure 3.4:   Overall view of Gamma cell 220 Excel

The Gamma cell 220 Excel is a Cobalt-60 irradiation facility manufactured by Atomic Energy of Canada Limited for use in an unshielded room. It is a self-contained γ-irradiator and self-shielded making it operation safe. Dose calibration for this cell is important for samples irradiation. The unit basically consists of an annular source permanently enclosed within a lead shield, a cylindrical drawer, and a drive mechanism to move the drawer up or down along the source centre-line automatically. The drawer has a chamber to carry samples to be irradiated from outside the shield to the source. Samples up to approximately 6 inches in diameter and 8 inches in height can be accommodated in the chamber. Liquid, gaseous, electrical or mechanical connections can be introduced into the sample chamber through an access tube in the upper portion of the drawer. An electrically powered digital timer automatically raises the drawer at the termination of a sample irradiation. Times may be pre-set to a maximum of 999.9 hours.

3.6 Thermo-Physical Characterization

3.6.1 Density

Density (ρ) of phosphate glass samples was measured using Archimedes principle and DI water was used as the immersion liquid. Measurement of weight loss of the sample upon immersion in a suitable liquid allows estimation of the density according to the following formula:

$$\rho = \rho_t \frac{w_\alpha}{(w_\alpha - w_l)} \tag{3.1}$$

where w_α and w_l are samples weights in air and liquids, respectively. The parameter ρ_t is the density of the immersion liquid. Therefore, (w_α - w_l) is the weight loss of the sample upon suspension in the liquid. The choice of immersion liquid is based on convenience and the chemical durability of samples. DI water was used to measure density of phosphate glass in the present study. In glasses, the density is an additive property and the density of the glass is the weighted average of the densities of individual components. Crystallization of a glass can significantly alter the density, when the density of the crystalline phase was different from the residual glass. The molar volume V_m of the glass samples can be calculated from the following relation:

$$v = \frac{M.W}{\rho} \tag{3.2}$$

where ($M.W.$)is the molecular weight of the glass sample. In this study, the reported density values are the average of at least three independently measured values.

3.6.2 Hardness

Hardness is the resistance of a material to permanent deformation under contact loading. The hardness of the glasses is a function of the strength of individual bonds and the density of the packing of atoms in the structure. One of the most common techniques for hardness measurement is the Rockwell indentation technique. This technique measures the permanent depth of indentation produced by a force/load on an indenter. A Bench (Rockwell) hardness tester TH320 as shown in Figure 3.5 was used for hardness measurement for the phosphate glass in the present study.

Figure 3.5: A Photograph of Bench (Rockwell) hardness tester TH320

The sequence of the Rockwell method is simply described here; 1) the tested surface is exposed to the penetrator and the first minor load, preload F_o usually 10 kgf is applied as shown in Figure 3.6(A). A small indentation appears. At this point, the meter is set to zero. 2) The major load F_1 (60 kgf of diamond cone) is slowly

applied additionally without shocks. Together with the preload this is defined as total test load, **F** as shown in Figure 3.6(B). 3) The indicator of the meter finally stops moving, the additional load F_1 is removed until the preload is applied respectively. This way, the penetrator remains in the imprint and all elastic deformations, which were caused by the application of the total test load, are eliminated; thus, the meter only shows the remaining penetration depth (as difference between preload and total test load) as shown in Figure 3.6(C). To calculate the Rockwell hardness number, the application of the additional major load is used and the permanent increase in depth of penetration was measured. Equation 3.3 was then used to obtain the Rockwell hardness number from the length of the diagonals of the indent. The HRA values reported in this thesis are the average values of at least 10 independent indents made on each sample under identical loading conditions.
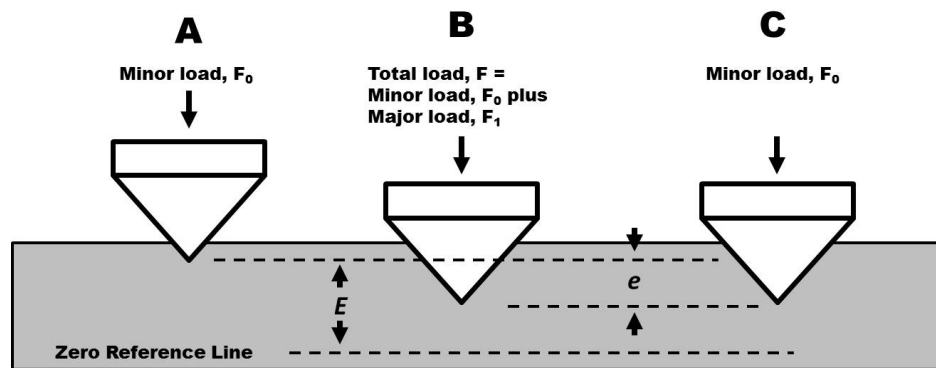
Figure 3.6: **The principle of Rockwell hardness measurement**

$$HR = E - e \tag{3.3}$$

where HR is a Rockwell hardness number, **E** is a constant depending on form of indenter and **e** is a permanent increase in depth of penetration due to major load F_1.

3.6.3 Differential scanning calorimetry

Differential scanning calorimetry (DSC) analysis is one of informative method in physical characterization of glass compound using a thermos-analytical technique in which monitors heat effects associated with phase transitions and chemical reactions as a function of temperature. A DSC model Mettler Toledo as

shown in Figure 3.7 was used for thermos-analytical measurement for the glass in the present study.

Figure 3.7: The differential scanning calorimetry model Mettler Toledo (DSC 822e)

In DSC, the difference in heat flow to the sample and a reference at the same temperature is recorded as a function of temperature. The reference is an inert material such as alumina or empty aluminum pan. The temperature of both the sample and reference are increased at a constant rate. Since the Differential Scanning Calorimeter is at constant pressure, heat flow is equivalent to enthalpy changes:

$$\left(\frac{dq}{dt}\right)p = \frac{dH}{dt} \tag{3.4}$$

where dH/dt is the heat flow measured in mcal/sec. The heat flow difference between the sample and the reference is:

$$\frac{\Delta dH}{dt} = \left(\frac{dH}{dt}\right) sample - \left(\frac{dH}{dt}\right) reference \tag{3.5}$$

and can be either positive or negative depending on their processes. In an endothermic process, heat flow to the sample is higher than that to the reference. Hence ΔdH/dt is positive. Besides, in an exothermic process such as crystallization, cross-linking processes, oxidation reactions or decomposition reactions, the dH/dt is negative.

The main application of DSC is studying the glass phase transitions, melting and exothermic decompositions. These transitions involve energy or heat capacity

changes that can be detected by DSC with great sensitivity. When the glass sample undergoes a physical transformation such as phase transitions, heat will need to flow to it than the reference to maintain both at the same temperature. Whether high or low heat flow to the sample is depends on the process whether it is exothermic or endothermic. By observing the difference in heat flow between the sample and reference, DSC used to measure the amount of heat absorbed or released during such glass transitions.

The result of a DSC experiment is a curve of heat flux versus temperature or versus time. This curve can be used to calculate enthalpies of transitions. This is done by integrating the peak corresponding to a given transition. It can be shown that the enthalpy of transition can be expressed using the following equation:

$$\Delta H = KA \qquad\qquad\qquad (3.6)$$

where ΔH is the enthalpy of transition, K is the calorimetric constant and A is the area under the curve. The calorimetric constant will vary from instrument to instrument, and can be determined by analyzing a well-characterized sample with known enthalpies of transition.

3.7 Structural characterization

3.7.1 Dynamic light scattering

Dynamic light scattering (DLS) is a technique that can be used to determine the size distribution profile of small particles such as AgNPs and AgNPs-polymer in suspension or polymers in solution. DLS is based on the Brownian motion of dispersed particles. When particles are dispersed in a liquid they move randomly in all directions. The principle of Brownian motion is that particles are constantly colliding with solvent molecules. These collisions cause a certain amount of energy to be transferred, which induces particle movement. The energy transfer is more or less constant and therefore has a greater effect on smaller particles. As a result, smaller particles are moving at higher speeds than larger particles. In brief, a single frequency laser is directed to the sample contained in a cuvette. If there are particles in the sample, the incident laser light gets scattered in all directions. The scattered light is detected at a certain angle over time and produce signal to determine the

diffusion coefficient and particle size by the Stokes-Einstein equation as shown in Figure 3.8.
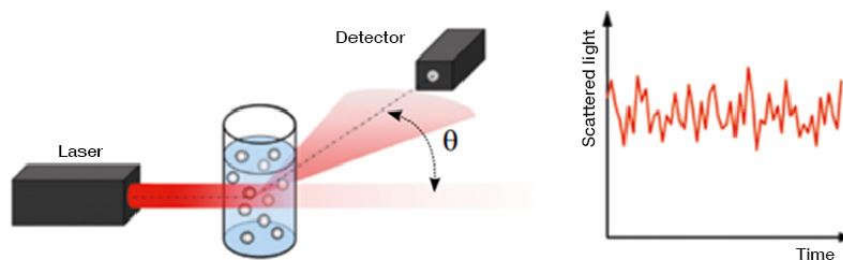
Figure 3.8: Basic setup of a DLS measurement system. The sample is contained in a cuvette. The scattered light of the incident laser can be detected at different angles [85].

In the present study, AgNPs solutions were used to measure the sizes of nanoparticles. The samples were recorded on Nano ZS zetasizer system as shown in Figure 3.9. The particle sizes in liquid suspension were both measured at 25 °C. A 633 nm, He-Ne laser was used as the light source while an avalanche photodiode (APD) served as the detector. The signals were collected and the data were analysed using Zetasizer Software.
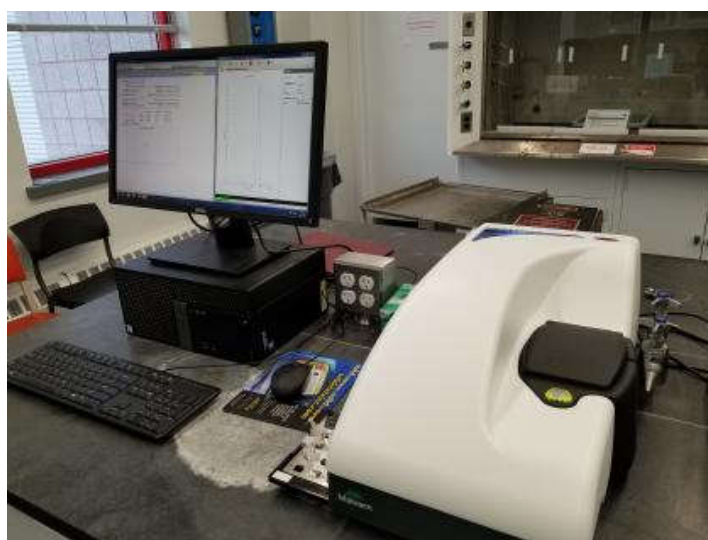
Figure 3.9: Dynamic light scattering model Nano ZS zetasizer system Malvern Instrument

3.7.2   X-Ray diffractometer

X-ray diffractometer (XRD) is an indispensable tool for material characterization. It is a non-destructive technique and widely used in phase identification and structure delineation for diversified materials from crystalline to amorphous states. The principle of XRD technique is based on scattering of X-rays by a crystal consisting of well-defined array of atoms, ions and molecules. Since the crystal lattice consists of parallel arrays of atoms equivalent to the parallel lines of the diffraction grating, the inter-planar spacing could be successfully determined from the separations of bright fringes of the diffraction pattern. These inter-planar distances are of the same magnitude as the wavelength of X-rays (0.5 to 2 Å) and hence, crystal planes act as diffraction gratings. Interaction of X-rays reflected by a set of parallel planes satisfying Bragg's condition lead to constructive interference only at a particular angle. The Bragg equation for the occurrence of such diffraction can be written as:

$$n\lambda = 2d \sin\theta \tag{3.7}$$

where λ is the wavelength of X-rays, θ is glancing angle, d is the inter-planar distance and n is order of diffraction. A typical block ray diagram of a powder diffractometer is shown in the Figure 3.7.

The XRD characterization can be carried out either from single crystals or polycrystalline samples powder for qualitative and quantitative phase identification, refinement of structure solutions of crystalline materials and for determination of particle size and strain in materials. In XRD, powdered sample either as smeared layer or compact flat pack is exposed to monochromatic beam of X-ray and the diffracted beam intensity is collected in a range of angles (2θ with respect to the incident beam). For crystalline material, the intensity corresponding to a constructive interference of the diffracted beam from crystallographic plane is observed as a peak corresponding to the Bragg angle (θ), giving sharp peaks in their diffraction pattern. However, diffraction pattern of glasses is characterized by a broad hump because glasses have short range order rather than long range periodicity and there is considerable distribution of bond length and bond angles between the constituent atoms.
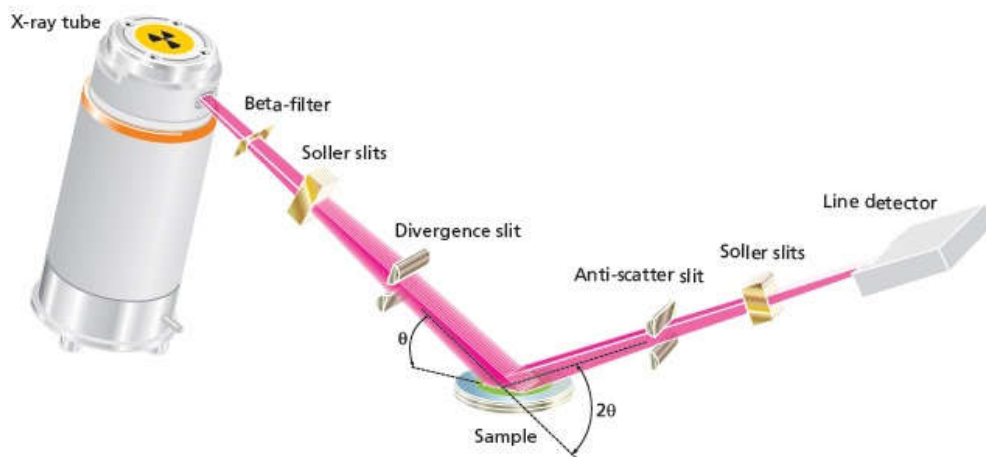
Figure 3.10: A schematic diagram of an X-Ray Powder Diffractometer [86].

In the present study, powder XRD was used to verify the amorphous nature of the phosphate glasses. The diffractograms of all the samples were recorded either on Bruker D8 Advance XRD as shown in Figure 3.8 based on the Bragg-Brentano reflection geometry. Data were collected using Ni filtered Cu-Ka (1.54 Å) radiation in the $5° \leq 2\theta \leq 80°$ range at a scanning speed of $1°.min^{-1}$. The observed diffraction patterns were compared with JCPDS (Joint Committee on Powder Diffraction Standards) files or references journal available for reported glass samples.
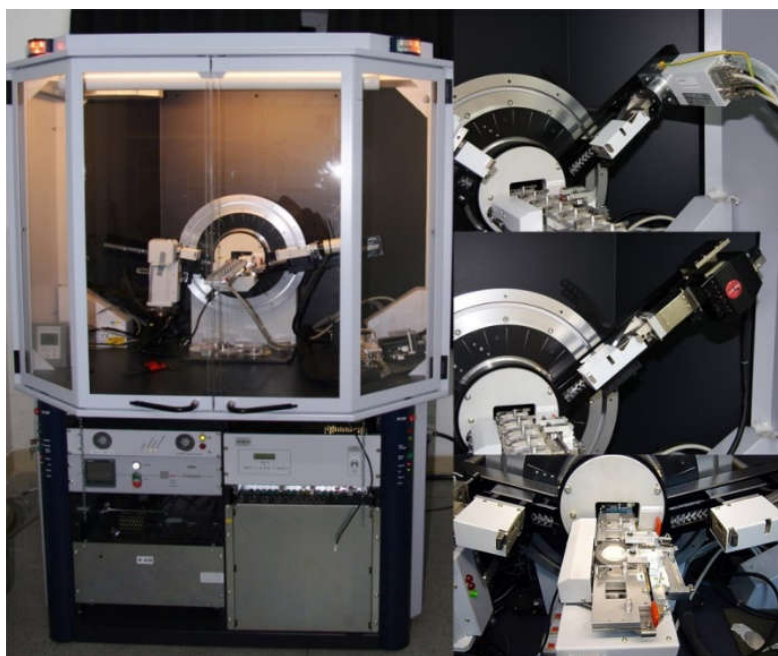
Figure 3.11: A photograph of XRD model Bruker D8 Advance

3.7.3   Scanning electron microscopy

The scanning electron microscopy (SEM) is a versatile electron microscopic technique that provide at one end surface information such as texture, topography and dimension up to a length scale of few tens of nanometres and on the other hand provides a three-dimensional effect to the images due to depth of focus of the SEM instruments. The SEM provides image of a sample at much higher magnification, higher resolution and depth of focus compared to optical microscopy due to very low wavelength of accelerated electrons. Two types of interactions occur in the SEM between the electron beam and the specimen. These interactions may be either elastic, if the electron beam strikes the sample and there is a change in its direction without change in its energy (backscattered electrons), or on inelastic interaction, which occurs when the beam of electrons strike an orbiting shell electron of the specimen, causing the ejection of secondary electrons, characteristic photon radiation (x-ray or visible radiation) and other types of events from the specimen interaction volume. The backscattered electrons allow element distribution analysis since the intensity of scattering is Z (atomic number) dependent. The secondary electrons on the other hand are liberated from a small volume in the vicinity of the surface. Therefore, the secondary electrons can be used to study the surface of samples. The schematic of a typical SEM instrument is shown in Figure 3.12.
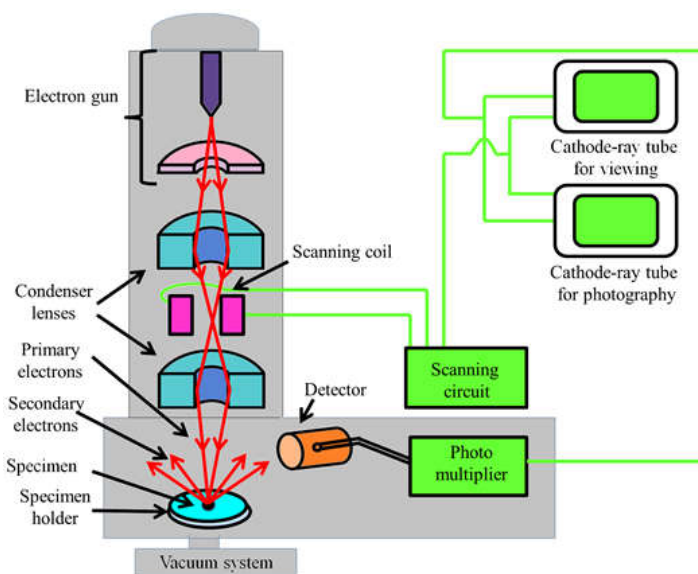
Figure 3.12:   A simplified schematic diagram of a scanning electron microscope.

In this instrument, a well-focused mono-energetic (~25 keV) electron beam is incident and scanned over the sample surface by two pairs of electro-magnetic deflection coils. The signals generated from the surface of the specimen by secondary electrons (SE) and backscattered electrons (BSE) are detected and fed to a synchronously scanned cathode ray tube (CRT) as intensity modulating signals [87]. Thus, the specimen image is displayed on the CRT screen. SEM instrument is generally operated in three prominent modes namely secondary electron mode, backscattered electron mode and X-ray radiation mode. In secondary electron (SE) mode, scintillator photomultiplier is used as the detector. In this mode energies of secondary electrons are quite low and its strength depends on the beam size, beam current, angle of incidence, the topography and the atomic number of the sample. In backscattered electron (BSE) mode, a scintillator photomultiplier is used as a detector but the escape depth is comparatively large (1000 Å) because of the large energy from the back scattered electrons. In X-ray radiation mode, the X-rays produced due to interaction of the electron beam with the samples are used to characterize the sample. The characteristic X-ray gives an idea about the element present in the sample qualitatively and also quantitatively. Besides, X-rays may be collected either in wavelength dispersive or energy dispersive mode. In energy dispersive mode, a liquid nitrogen cooled Li drifted silicon or germanium detector along with multi-channel analyzer is made use of to detect all the elements simultaneously. Nowadays, in SEM instruments, Energy dispersive X-ray (EDX) attachment is also available for compositional analysis. The SEM images presented in this work such as AgNPs-PEI and AgNPs-PSS were taken on a CamScan MX2500 SEM fitted with an EDX detector (CamScan Electron Optics Limited, UK) using the secondary electron detector as shown in Figure 3.13.

Figure 3.13: Photograph of a SEM model CamScan MX2500

The sample to be probed by SEM should be vacuum compatible ($\sim 10^{-6}$ mbar or less). Besides, the sample to be analysed need to be electrically conducting, otherwise there is a charge build up due to the impinging electrons which gives rise to jumping of beam and hence intensity. The surfaces of non-conductive materials are made conductive by coating with a thin film of gold or platinum or carbon. Therefore, prior to imaging each glass samples were sputter coated with 10 nm of platinum or gold to render the surface conducting using an Emitech K575X (Quorum Technologies, UK) as shown in Figure 3.14. The sample was then imaged by an electron beam of energy within range of 10-25 keV and micrographs were recorded at different magnifications from 1kx to 60 kx.
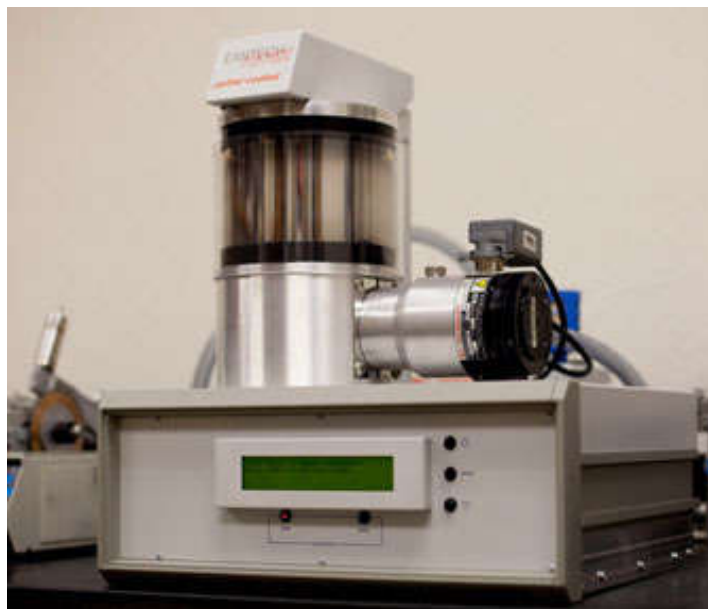
Figure 3.14: Emitech K757X Sputter coater at Flinders University.

3.7.4 Transmission electron microscopy

Transmission electron microscopy (TEM) is a microscopy technique in which a high-electron beam is transmitted through an ultra-thin specimen to observe features in the structure like dislocations and grain boundaries. An image is formed from the interaction of the electrons transmitted through the specimen and magnified then focused onto an imaging device, such as a fluorescent screen on a layer of photographic film. The TEM images presented in this work such as AgNPs-PEI and AgNPs-Pss were taken on a Tecnai G2 20 S-Twin, FEI as shown in figure 3.15.

Figure 3.15: The HRTEM model Tecnai G2 20 S-Twin, FEI

The TEM operates on the same basic principles as the light microscope but uses electrons instead of light. Because the wavelength of electrons is much smaller than that of light, the optimal resolution attainable for TEM images is many orders of magnitude better than that from a light microscope. Thus, TEMs can reveal the finest details of internal structure as small as individual atoms. Figure 3.16 shows a schematic diagram of the path of a beam of electrons in a TEM from just above the specimen and down the column to the phosphor screen. Generally, TEM is divided into two main parts: illumination and imaging system. As the electrons pass through the sample, they are scattered by the electrostatic potential set up by the constituent elements in the specimen at the illumination system. In details, the beam of electrons is focused into a coherent beam using the condenser lens. The beam then strikes and passing through the specimen. The electromagnetic objective lens which focuses all the electrons scattered from one point of the specimen into one point in the image plane at the imaging system. Optional objective apertures can be used to enhance the contrast by blocking out high-angle diffracted electrons. The image then passed down the column through the intermediate and projector lenses, is enlarged all the way. The image strikes the phosphor screen and light is generated, allowing the user to see the image. The darker and lighter areas of the image represent those areas of the sample that fewer and more electrons are transmitted through.
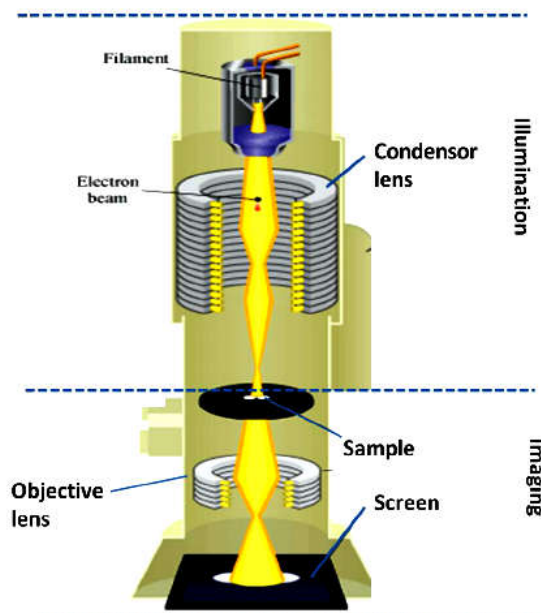
Figure 3.16: Schematic diagram of a TEM.

3.7.5   Raman spectroscopy

Raman spectroscopy has been used for the identification and characterization of materials by Raman scattering in which samples are irradiated with light and the scattered light is measured. Raman scattering is an inelastic scattering of electromagnetic radiation (mainly visible) from any excited states (mainly vibrational states) in the material. In Raman spectroscopy, a monochromatic incident radiation of frequency V_o (typically from some type of laser) is scattered inelastically from different vibrational states of the sample. Most of the incident light scattered elastically (Rayleigh scattering) and only a small fraction of incident light (1 in 10^7 photons) is scattered inelastically at frequency V_o-ΔV or V_o+ΔV. The small change infrequency of the Raman or inelastically scattered light is called Raman shift, corresponds to the energy required to excite vibration in a molecule.
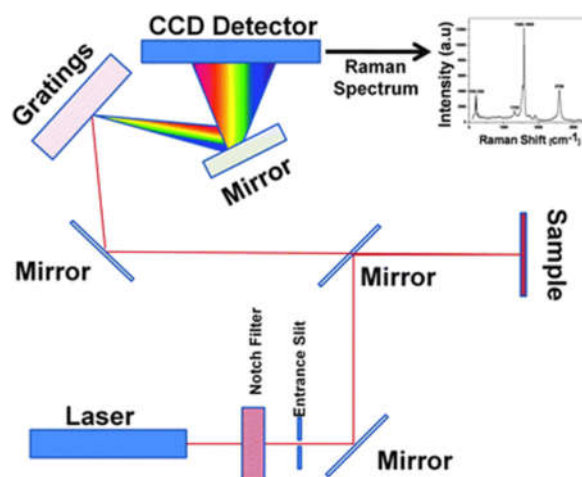
Figure 3.17: Schematic of Raman Spectrometer.

Raman scattering setup consists of an excitation source, spectrometer, detector and electronics system with output device as shown in Figure 3.17. Highly monochromatic, directional and high power density excitation radiation in visible range is required for Raman spectroscopy. Therefore, lasers are suitable excitation sources. The Raman scattered light is analysed using a scanning grating spectrometer. The principal requirement of Raman spectrometer is its stray light rejection capacity, which is the Rayleigh scattered radiation which always accompanies the Raman scattered light and is $\sim10^3$-10^5 times stronger. A notch filter having high and sharp absorption about the laser light is used in front of the entrance slit in single stage spectrometer to block the stray light. Raman signals are very weak and low noise detector is of primary importance. The detectors employed in the multichannel spectrographs are charge coupled devices (CCD) with a 2D array of potential wells (known as pixels), which stores the information generated by photoelectron.

The main advantage of this technique is that an ambient atmosphere can be used and no special sample preparation is required for analyzing samples. The intensity of bands in the Raman spectra of a compound are governed by the change in polarizability, α, occurs during the vibration and given by following expression:

$$I_{Raman} = KI_L(V_o - V_i)^4 x(\frac{d\alpha}{dQ})^2 \tag{3.8}$$

where I_L is the power of the laser at the sample, V_o & $V_i$are the frequencies of the incident and scattered lights respectively and $d\alpha/dQ_i$ is change in the polarizability with the normal coordinate of the vibration. The constant of proportionality (K) is dependent on the optical geometry, collection efficiency, detector sensitivity and amplification.

In this study, Raman spectra were recorded on a DeltaNu 633 Raman spectrometer using 633 nm lines from HeNe laser as shown in Figure 3.18. The Raman spectra of glasses in particular have a strong frequency and temperature dependence. Therefore, the intensity at lower frequencies has an unwanted scattering component, which can be taken care by appropriate corrections. Raman spectra have been corrected by multiplying the correction factor 'R' for the unwanted scattering component by employed the equation below [88]:

$$R = V_o^3 (1 - e^{\frac{-v}{kT}}) \frac{v}{(v_o+v)^4} \tag{3.9}$$

where V_o and V are the frequencies (in cm^{-1}) of excitation line and Raman shift, respectively. A baseline correction has been employed. Since, the glasses exhibit broadband features, the instrumental line width does not include in the analysis.

Figure 3.18: A photograph of Raman spectrometer model DeltaNu' 633

3.7.6   Fourier transforms infrared spectroscopy

Vibrations of bonds and groups, which involve a change in the dipole moment, result in the absorption of IR radiation, which form the basis of the IR spectroscopy. In FTIR instrument, all the frequencies are used simultaneously to excite all the vibrational modes of different types of bonds/linkages present in the sample. The FTIR technique is based on a Michelson interferometer, which is an optical device consisting of a fixed mirror, movable mirror and a beam splitter. The interferometer shifts the phase of one of the beam with respect to another by moving one of the mirrors and keeping the other mirror at a fixed position as shown in Figure 3.19. When the two beams overlap, depending on whether they are in phase or out of phase, constructive and destructive interference takes place. If the light source is monochromatic, the intensity of the interference pattern will rise and fall periodically and the detector will measure a sinusoidal signal as a function of the optical path difference.
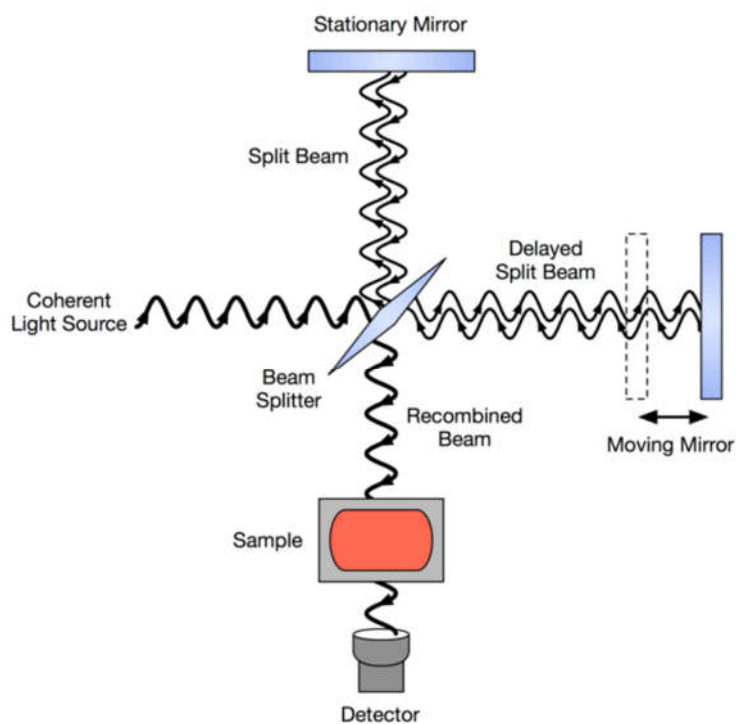
Figure 3.19: Schematic diagram of a FTIR

In the present study, all infrared experiments were carried out using a FTIR model Perkin Elmer Frontier (Figure 3.20) with a resolution of 4 cm^{-1} having a range

of 4000-400 cm^{-1} proprietary KBr beam splitter and deuterated triglycine sulphate (DTGS) as the detector. FTIR transmittance spectra were recorded at room temperature on samples in the pellet form.
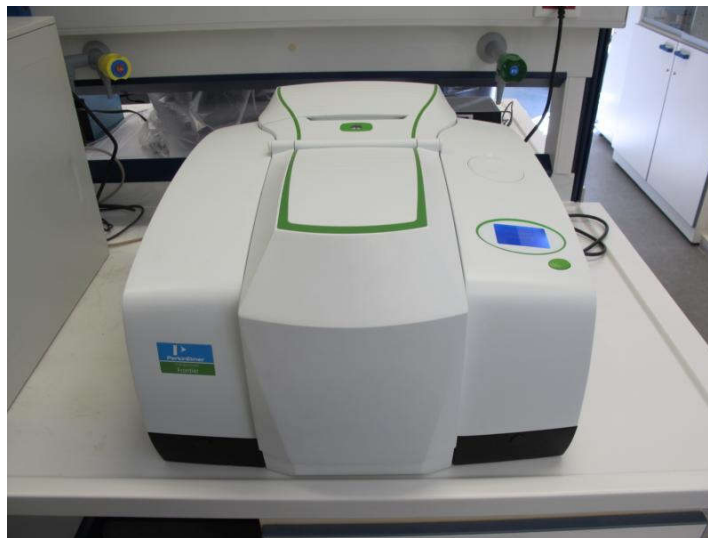
Figure 3.20: A photograph of a FTIR model Perkin Elmer Frontier at UKM

3.8   Optical Characterization

3.8.1   Ultraviolet-Visible spectroscopy

Ultraviolet-visible spectroscopy (UV-Vis) is the instrument used to measure the transmission and absorption of sample based on the attenuation of a beam of light after it passes through or reflection from surface of samples. Oxide glasses generally absorb strongly both in the range of infrared and ultraviolet spectral region. The former is associated with the interaction of light with the molecular vibrations and the latter with the electronic transitions between the valence and conduction band or between the excitation levels. Most of the oxide glasses are highly transparent in the visible region with a broad absorption edge in the UV region. The position and shape of the absorption edges depend on the composition as well as the nature of the network former and modifier cations in glass matrix.

The absorption coefficient (α) of a transmitting medium can be expressed by Lambert-Beer law:

$$I = I_o e^{-\sigma l N} \tag{3.10}$$

where I_o is the intensity of the incident light, I is the intensity of the light transmitted through a sample of length (l), σ is an absorption of cross-section and N is the number density of attenuator. The transmissivity (ability to transmit) of sample is expressed in terms of an absorbance, A which is defined as:

$$A = -\ln(\frac{I}{I_o})$$ (3.11)

This indicates that the absorbance value becomes linear with the concentration or number density of attenuators according:

$$A = \sigma l N$$ (3.12)

Optical absorption spectra of glassy material are characterized by a broad absorption edge. The onset of optical absorption can be obtained from the extrapolation method and can be correlated with the $E_{optical}$ values of the glasses.
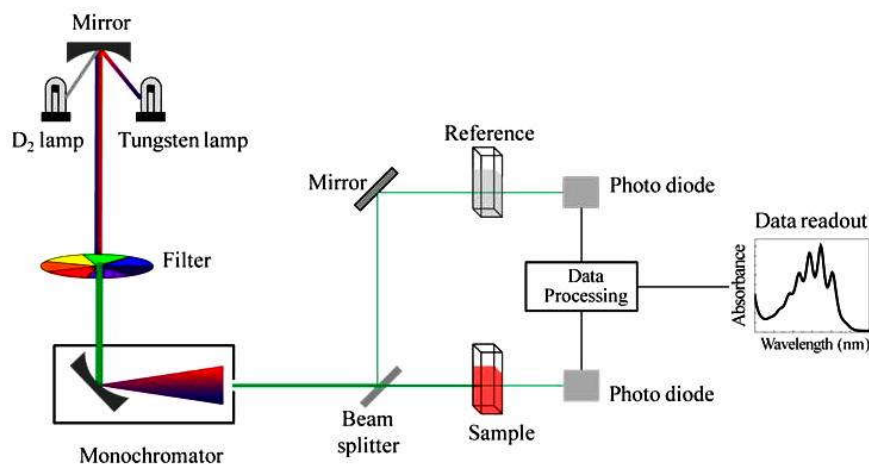
Figure 3.21: A Schematic diagram of UV-Vis spectroscopy

In a commercial UV-Vis spectrometer usually a deuterium discharge lamp is used as light source for UV measurements range and a tungsten-halogen lamp as light source for visible measurements range of samples. The instruments automatically switch lamps when scanning between the UV and visible regions of samples. A holographic grating in monochromator used to disperse the wavelengths of those continuous light sources. Next, the spectral band pass is then determined by the monochromator slit width or by the array-element width in array-detector spectrometers and optical components are optimized to reject stray light, which is

one of the limiting factors in quantitative absorbance measurements. Photodiode, phototube, or photomultiplier tubes (PMT) are commonly used as detector in UV-Vis spectrometer. A Schematic diagram of UV-Vis spectroscopy is shown in Figure 3.21.

A commercial UV-Vis spectroscopy model Pelkin-Elmer lambda 950 was used in the present study for recording the absorption curves of glass samples as shown in Figure 3.22. The glass samples in the form of a disc having diameter more than 10 mm with 30 mm length and thickness in the range 2-4 mm were prepared and polished with 0.3 μm alumina powder for optical measurements. The optical absorption and transmission measurements were carried out in the 200-900 nm range with 2 nm resolution.

Figure 3.22: A photograph of UV-Vis spectroscopy model Pelkin Elmer lambda 950

3.8.2 Photoluminescence spectroscopy

Photoluminescence (PL) is a process, in which a substance absorbs photons and then re-emits photons of lower energy. Quantum mechanically, this can be described as an excitation to a higher energy state by absorption of photon and then a return to a lower energy state accompanied by the emission of a photon. The schematic of spectrofluorometer is shown in Figure 3.23. The light from an excitation source passes through a monochromator and strikes the sample. A proportion of the incident light is absorbed by the sample and then fluoresces. The fluorescent light from samples is then emitted in all directions and some of this fluorescent light passes through a second monochromator and reaches to a detector,

which is normally placed at 90° to the incident light beam to minimize the risk of reflected incident light reaching the detector. Numerous light sources may be used as excitation sources such as photodiodes, lasers and lamps (xenon arcs and mercury-vapor lamps). The most common type of monochromators utilizes a diffraction grating, which is collimated light illuminates a grating and exits with a different angle depending on the wavelength. The monochromator can then be adjusted to select which wavelengths to transmit. The most commonly used detector is photomultiplier tube.
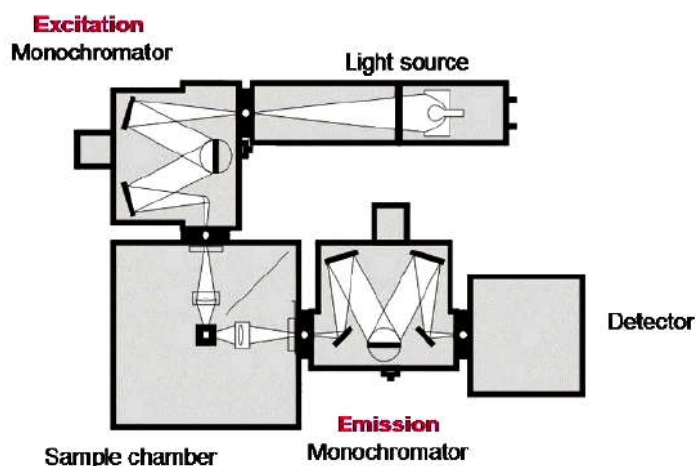
Figure 3.23: Schematic diagram of photoluminescence spectroscopy

The dual monochromator spectrofluorometer and continuous excitation light source can measure both excitation and emission spectrum simultaneously. The wavelength of the excitation light is kept constant when measuring emission spectrum, preferably at a wavelength of high absorption and the emission monochromator scans the spectrum. For excitation spectrum measurement, the wavelength passing through emission monochromator is kept constant and the excitation monochromator is subjected to scan. Generally the excitation and absorption spectrum results are identical.

In the present study, all luminescence measurements were carried out at room temperature by using a Varian Cary Eclipse photoluminescence spectroscopy (Figure 3.24). The glass samples were stuck on the slide holder in the sample chamber of the instrument. Emission spectra were recorded with a resolution of 5 nm and all emission spectra were corrected for the detector response.

Figure 3.24: A photograph of photoluminescence spectroscopy model Varian Cary Eclipse with Peltier temperature controller and front surface accessory.

Chapter 4

4.   Adsorption of Polyelectrolyte Layers on AgNPs Surface: Synthesis and Hue Changing Study

4.1   Introduction

Nowadays, nanoparticles provide a unique and useful opportunity for a great potential application in medical [89], optical [90], or electronic devices such as solar energy panel [91], drug targetry system [92], optical sensor [93] and so forth due to their special characteristics of high surface to volume ratio and nanometric size. Among those nanoparticles, silver has recently attracted great attention because it has strong optical absorption in the visible region due to localized surface plasmon resonance (LSPR) of free electrons which can be tuned by controlling the particles size and shape [94], enabling the monitoring of their evolution and colour formation by UV-Vis measurements. Moreover, biomedical advancement using silver nanoparticles (AgNPs) are interesting topics to be explored as AgNPs have continually been used for both biomedical [24] and imaging applications [95]. However, the instability of nanoparticles gives rise to aggregation which deters its use for specific applications. The surface charge and colour solution of AgNPs, an essential desired feature remains a key challenge. There are ways to overcome these using surface modification treatments such as citrate [96], chitosan [97], silanization [98] and polymer [99] coating through steric or depletion stabilization. Besides, polymer coatings have been found to protect AgNPs and more suitable in bio-related labelling applications [100]. Therefore, the interest in surface treatment or coating is because combination of the properties of two or more materials involved with the emphasis on the fact that one of the materials (shell) will determine the surface properties of the particle while the other i.e. the core is completely encapsulated by the shell.

In this study, the preparation of AgNPs from aqueous solutions of Ag^+ salts by chemical reduction at room temperature using citrate as protecting agent and focus more on modified AgNPs surface with a protic polyethyleneimine (PEI) and

aprotic poly(sodium 4-styrene sulfonate) (PSS) polymers has been reported. PEI and PSS polymers with different functional groups were chosen for inorganic-organic complexes such that nanocomposite complexes formation could be compared. PEI is a branched chain polymer with a ratio of 1:2:1 for primary: secondary: tertiary amine groups and two carbons aliphatic CH_2CH_2 spacer.

Moreover, under extreme nanoconfinement of AgNPs-polymer, the physical confinement has a more significant impact than the polymer–nanoparticle interactions on the viscosity of unentangled polymers, measured through infiltration dynamics, as well as the glass transition temperature. These findings will provide fundamental frameworks for designing processes to enable the fabrication of nanoparticles in glass with a wide range of nanoparticles and polymers as well as good distribution of nanoparticles in glass [101].

Besides, PSS was chosen because of their antimicrobial properties and generally used for sexually transmitted diseases prevention [102] or as proton exchange membranes in fuel cell applications [103]. PSS is also a branched chain polymer containing phenyl and sulfonate functional group with a strong anionic polyelectrolyte, possessing several negative charges along its backbone chain which directly replaces citrate shell from AgNPs core, forming intermediate charged clusters. Due to this, PEI and PSS are of special interest because it can control and stabilize both AgNPs and clusters along the polymeric chains with high stability with time [104]. Another part of this study was to demonstrate the formation of colloidal complexes resulting from the spontaneous association of AgNPs and polymers functional groups that could changes or reduces its sols' colour. The AgNPs-polymer complexes formed were characterized using UV-Vis, dynamic light scattering (DLS), Raman spectroscopy, scanning electron microscopy (SEM) and Fourier transform infrared (FTIR).

4.2   Experimental

4.2.1   Chemicals

The materials used were as follows: an aqueous hydrogen peroxide solution (H_2O_2 content 30 wt.%) was purchased from Chem-Supply, Bedford St, Gillman SA,

Australia. Branched polyethyleneimine (PEI), 50% (w/v) aqueous solution (average Mw = 750 000) and poly(sodium 4-styrene sulfonate) (PSS), powder form (average Mw = 70 000), silver nitrate ($AgNO_3$ purity >99%), sodium borohydride ($NaBH_4$ purity > 97%), trisodium citrate ($Na_3C_6H_5O_7$ purity > 99.5%), potassium bromide (KBr ACS reagent > 99%) were bought from Sigma-Aldrich Chemie, Steinheim, Germany and used without any further purification. All aqueous solutions were prepared using deionized water with millipore grade (resistivity > 18.2 $M\Omega cm^{-1}$).

4.2.2   Synthesis of silver nanoparticles

Five portions of each PEI and PSS of 0.1, 0.5, 1.0, 1.5 and 2.0 % wt. stock solutions were made by dissolving 0.02, 0.1, 0.2, 0.3 and 0.4 g of each polymer in 20 mL deionized water at room temperature, respectively. The solutions were magnetically stirred for one hour. Meanwhile, aqueous mixtures of $AgNO_3$ (0.375 mM, 120 mL), $Na_3C_6H_5O_7$, Na_3CA (12.5 mM, 48 mL) and H_2O_2 (50 mM, 120 mL) were prepared. The bulk sample was divided into two parts and a KBr solutions (1 mM; 180 & 360 µL) was added to each solution described above and stirred for a further one hour to produce different sizes of AgNPs, respectively. Subsequently, $NaBH_4$ (5 mM, 25-30 mL) was injected to each mixed solution and the reaction was initiated. The stirring was continued for another one hour to complete the reaction. The different colour of solution products confirms the formation of silver nanoparticles with different sizes [105]. The synthesized AgNPs dispersions showed no changes in the position of their optical absorption bands and intensity even after two months of storage at room conditions. A large quantity of such solution was made and served as the stock solution for AgNPs/polymer hue changing studies.

4.2.3   Coating of AgNPs by polymers

Polymeric composites of Ag-PEI and Ag-PSS were prepared by mixing the aqueous solutions of the respective polymers and the colloidal suspension of preformed AgNPs. The coating process of AgNPs by protic polymer PEI and aprotic polymer of PSS were performed by addition of 0.67 mL of each wt.% PEI and PSS to 15 mL (0.125 ppm) of each AgNPs sols making it 20 samples in total excluding control samples. The solution was stirred continuously during and after addition and it was observed that the shifting of AgNPs sols colour takes place within a minute.

The yellow-shift occurred for AgNPs/PSS samples after 5 min and the sols shifted to colourless for AgNPs/PEI samples with same procedure as polymer concentration is increased. Thin films of these solutions were casted on glass plates for further analysis especially for Raman and SEM characterizations.

4.2.4 Kinetic study

To determine the rate of the AgNPs colour shifting, the samples were prepared by adding freshly prepared polymer, PEI and PSS at varying concentration by vigorous shaking the solutions of AgNPs which contains different colour/sizes of particles in tube vessels as shown in Figure 4.2. The progress of the hue changing was followed via UV-Vis spectrum, recording at definite 20 min intervals until 120 min using UV-Vis Spectrophotometer, with 1 cm quartz cuvettes by measuring the absorbance of AgNPs sol formation at 200-800 nm (λ_{max} of each sol colour). The apparent rate constants (k_{obs}, min^{-1}) were calculated from the initial part of the slopes of the plots of ln (A_o/A_t) versus time with a fixed time method as shown in Figure 4.6. The pH of the reaction mixture was also measured at the beginning and end of each kinetic experiment.

4.2.5 Methods of characterization

All the samples products; AgNPs and the AgNPs/polymer complexes were characterized by UV-Vis Spectrometer (Pelkin Elmer Lambda 950) with scanning window from 200 to 800 nm band was used. The size distribution of AgNPs in the colloids was measured using a Nano ZS Zetasizer system (Malvern Instruments). The chemical bonding and interaction between AgNPs and 2.0 wt.% polymer complexes were analyzed using Surface Enhanced Raman Spectroscopy (SERS) and were recorded using Witec Alpha 300R instrument, equipped with the appropriate (×50 and ×100) objective lens and 532 nm He-Ne laser with output power up to 70 mW over the range of 3500-400 cm^{-1}. Finally, AgNPs with 2.0 wt.% of polymer micrographs were obtained using scanning electron microscopy (CamScan MX2500) and from the SEM results, the selected samples were further characterized with high resolution transmission electron microscopy (HRTEM, 200kV Tecnai G2 20 S-Twin, FEI). The FESEM samples were mounted on the stub and coated with a thin film of 5

nm platinum before observations. Structures of different polymers used for coating of silver nanoparticles are shown in Figure 4.1.

(PEI)   (PSS)
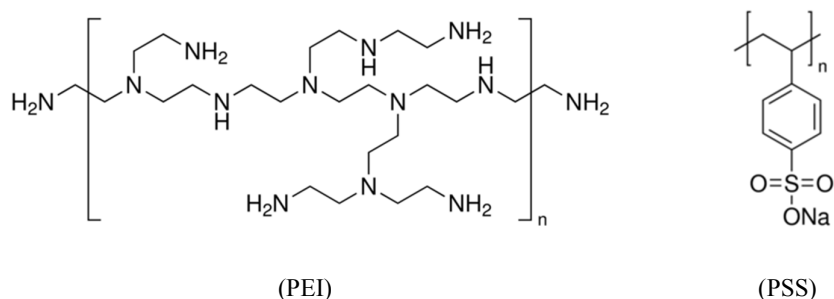
Figure 4.1: Molecular structures of polyethyleneimine and poly(sodium 4-styrene sulfonate).

4.3 Results and Discussion

4.3.1 General considerations

The first consideration in the preparation of different sized AgNPs is the pH of a reaction mixture. Therefore, controlling the pH value is a crucial task that addresses first by adding sodium borohydride ($NaBH_4$) making it alkaline (pH: 8.5±0.5). The pH value was found to be nearly constant even with increasing PSS and PEI concentration. Secondly, stability of AgNPs strongly depends on the protective agent that prevents the aggregation of AgNPs. Adsorption of citrate ions on particles surface create a first protective layer that plays a key role in stabilizing growing silver in the working solution [106]. Potassium bromide (KBr) salt was used to shield the negative charges of citrate ions from allowing the particles to clump together with another AgNPs surface and form aggregates. To make sure silver nanoparticles fully stabilized, another surface treatment was made by using polymers (PEI & PSS) as a layer for AgNPs core to prevent particles from aggregation [107]. The nucleated AgNPs/citrate with anionic surface charge is efficiently stabilized against flocculation by the strong coulomb interaction due to the inherent high cationic density of the protic PEI [108]. On the other hand, aprotic PSS with a strong anionic polyelectrolyte, possesses several negative charges along its backbone chain which can bind directly towards metallic cations of silver surfaces was used in this experiments as comparison to PEI [109].

Preliminary observations showed that the reduction of Ag+ ions with different KBr concentration by fresh borohydride at room temperature turns the colourless mixture to different colour as the reaction time increases. Therefore, with different size and colour of AgNPs, we choose citrate and polymers as the stabilizing and protecting agents in the present studies. The appearances of different colours were due to different visible light reflectance caused by the surface plasmon resonance of silver nanocrystals in the visible region [110]. With this goal, a unique adsorption mechanism between AgNPs and polymers (PEI & PSS) were primarily found to be responsible for the formation of stable AgNPs/polymer in sols. Extinction and shifting of AgNPs sols color were observed in the range of 0.1, 0.5, 1.0, 1.5 and 2.0 wt.% of PEI and PSS. Furthermore, different sizes of AgNPs solutions (~2 & ~17 nm) were used to observe the reaction rate of Ag-polymers complexes.

4.3.2 Effect of the polymer addition

One of the major findings of the present study was the significant influence of the polymer concentration on the final colour of each sample. Due to its functional groups in water solution, the binding of each functional groups target with AgNPs surface was made possible, forming AgNPs-polymer complexes wherein a replacement or binding together with citrate on AgNPs surface took place. Moreover, polymers concentration plays a key role for the stabilization of AgNPs along the polymeric chains, controlling their size and shape. In fact, the multicolour AgNPs map illustration in Figure 4.2 demonstrates that at an appropriately polymer concentration (0.5-2.0 wt.%), stable AgNPs were generated, showing different sol colours with different reaction time and polymer concentrations. In my observations, there is some colour change with time for almost all samples although it cannot be seen for the 18 nm AgNPs with PSS at low concentrations. AgNPs with PSS changes seem to be largely complete after 1 hour but AgNPs with PEI changes take 1 day to become colourless, which is presumably the absorption moving to lower wavelengths and going into the UV range.

It is important to note that at 0.1 wt.% PSS, shows no colour changes even after a week because of low attractive contact strength or surface coverage between AgNPs and PSS, therefore no bound PSS layers form on the AgNPs surface [111].

Conversely, the AgNPs sols colour changes for PEI treatment even 0.1 wt.% but in term of stability, its only stands just for a week depending on AgNPs primary sizes due to polymer bridging between PEI chains [111]. Those AgNPs with 0.5 to 2.0 wt.% of each polymer showed no changes in the position of their optical absorption bands even after two months completing the reaction and stabilized. Our study demonstrates that by increasing the polymers concentration from 0.1 to 2.0 wt.%, a yellow and colourless-shifted of sols' colour for AgNPs/PSS and AgNPs/PEI with a variety of hues perceived by the naked eye was obtained with a high stability versus time as shown in Figure 4.2. It was found that the polymers formed by coatings absorbed polymers on AgNPs form aggregates in the solution and remains stable for least 3 months.
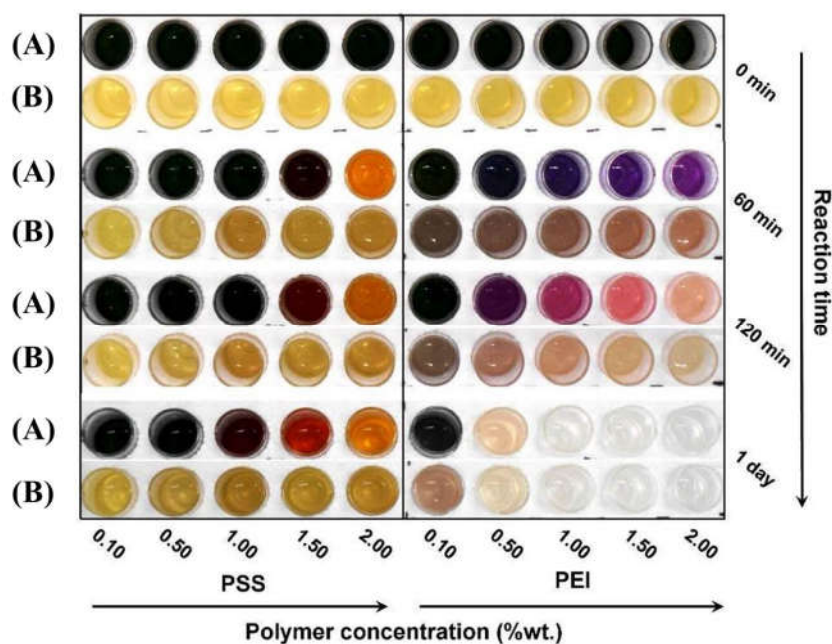
Figure 4.2: Photograph of multicolour AgNPs map obtained as function of variables PSS and PEI with AgNPs at different reaction times. AgNPs: (A) 17 nm & (B) 2 nm.

Based on the colour map in Figure 4.2 above, the samples were stable within a specific period and temperatures. The green (AgNPs-1 = 17 nm) and yellow (AgNPs-2 = 2 nm) sols are supposed to be in spherical shape characterized by vertices which produce wide covering spectra of red and violet wavelength regions, indicating the presence of several surface plasmons of high multipolar order [105]. Contradictorily, the assemblies of AgNPs/polymer relationship are more complex to

distinguish because of steric stabilization with hydro-dynamically and affinity attraction between functional group of each polymer and AgNPs surface, respectively.

A unique adsorption mechanisms between AgNPs and polymers (PEI & PSS) are primarily found to be responsible for the formation of stable AgNPs/polymer in sols and have been observed using Raman spectra (Fig. 4.9). Extinction and shifting of AgNPs sols colour were observed in the range of 0.1, 0.5, 1.0, 1.5 and 2.0 wt.% of PEI and PSS. At higher PSS concentration, the reaction mixture shifted to yellow colour but in the PEI case, the mixture turns colourless, because steric stabilization dominates between cationic amine group of PEI and anionic citrate, thus perfectly covering silver surface and neutralized negative charge of citrate on the AgNPs surface [107]. Nevertheless, there is no change in colour at low concentration of PSS because of insufficient amount of PSS to cap AgNPs surface as well as replacing citrate shell [111]. Apart from that, precipitates appeared at the bottom of PEI vials samples at a relatively low concentration (0.1 wt.%) because surface coverage was much below the saturation, suspensions may be destabilized due to polymer bridging occurring at this stage [111 & 112]. Therefore, different sizes of AgNPs solutions were used to observe the reaction rate of Ag-polymers complexes base on the shifting colour solutions of both samples.

4.3.3 Effect of KBr, PEI and PSS on mechanism of Ag-polymers complexes

The dependence of the AgNPs sols colour formation kinetics with the polymer (PEI) and (PSS) were studied between $0 \leq$ (PEI & PSS) ≤ 2.0 wt.% at fixed $(AgNO_3) = 0.375$ mM, $(Na_3CA) = 12.5$ mM, $(NaBH_4) = 5$ mM, $(H_2O_2) = 50$ mM and controlled $(KBr) = 1$ mM: 180 & 360 µL. KBr salt with different volumes use to shield or neutralise the negative charge of citrate ions on the AgNPs surface from allowing the particles to clump together to form aggregates [117]. Therefore, increasing the amount of KBr proportionally reduce negative charge of citrate/borohydride ions, which then caused plasmon shift to lower wavelength as the small size of AgNPs (yellow sol) were produced [94]. Figure 4.3 shows the UV-Vis spectra for different polymers (PEI & PSS) concentrations, from 0 to 2.0 wt.%, when others reaction condition was kept constant. The absorbance spectra shown in Figure 4.3(a & b) suggests that adsorption of PEI on the AgNPs surface results decrease in

the maximum absorption intensity at violet region around 400 nm band and the absorption intensity decreased gradually with time as the PEI concentration was increased due to decreases of surface plasmon resonance [94]. Moreover, the decrease behaviour (hypochromic shift) of absorbance after a definite time may be explained in terms of polymer adsorption onto the AgNPs surface. Besides, citrate-capped AgNPs with negative charge were brought in contact with cationic aqueous PEI, forming thick layer around AgNPs core as proved in Raman (Figure 4.10). Thus, we concluded that the PEI screen off AgNPs surface and reducing its surface plasmon resonance.

Figure 4.3(c & d) was also plotted to show a clearer picture of the evolution of optical absorption bands (regions 1 & 2) when the concentration of PSS was increased. An absorption band located at red region (region 2: 600-700 nm) of Figure 4.3(d) with small size of AgNPs obviously shifts to violet wavelength (400 nm) and slightly decreased in intensity peak in region 1 (violet region) as the PSS concentration is increased compared to bigger size of AgNPs with the resulting yellow colour indicates the excitation of the LSPR of spherical shapes and well dispersed in the solution due to the dielectric properties of the surrounding environment changed as shown in Figure 4.3c [118]. Another reason is PSS with strong anionic sulfonate functional group could replace citrate ions and attracted electrostatically towards AgNPs surface due to high affinity of positively charge compared to citrate, resulting in greater charge neutralization of AgNPs surface and produces stronger van der Waals force between AgNPs/PSS [119]. In addition, when the PSS weight concentration is increased, the generation of new colours is achieved as shown in Figure 4.3(c & d) with yellow-shift of sols' colour as refer in figure 4.2. These changes in sols' colour from green (AgNPs-1) and bright yellow (AgNPs-2) to dark yellow (higher PSS concentration) in all samples including AgNPs-1 and AgNPs-2 can be perfectly controlled during the addition of polymer in the initial solution.
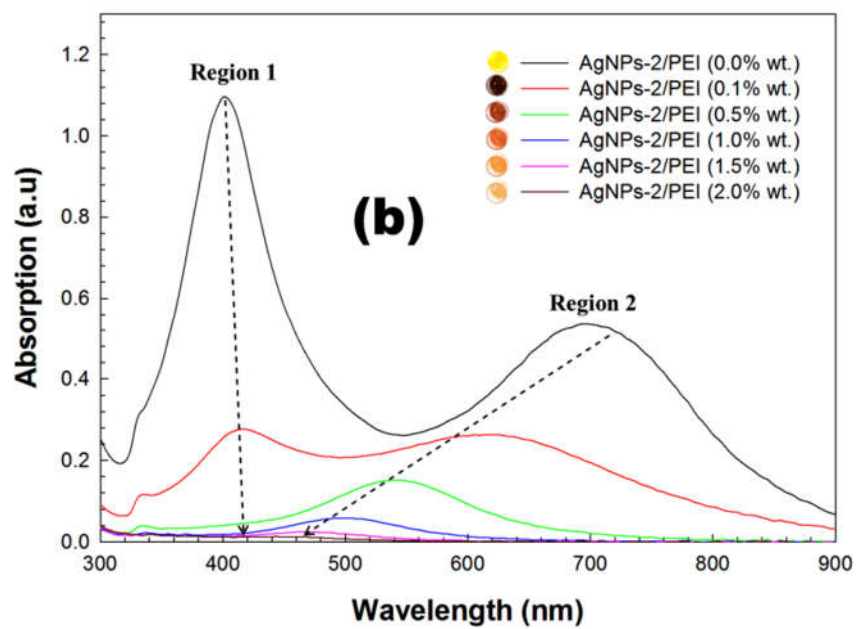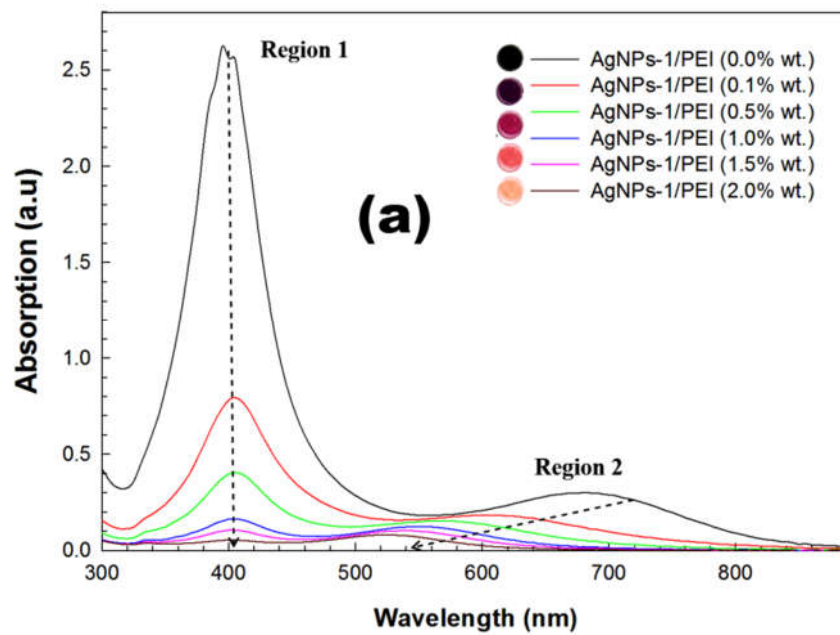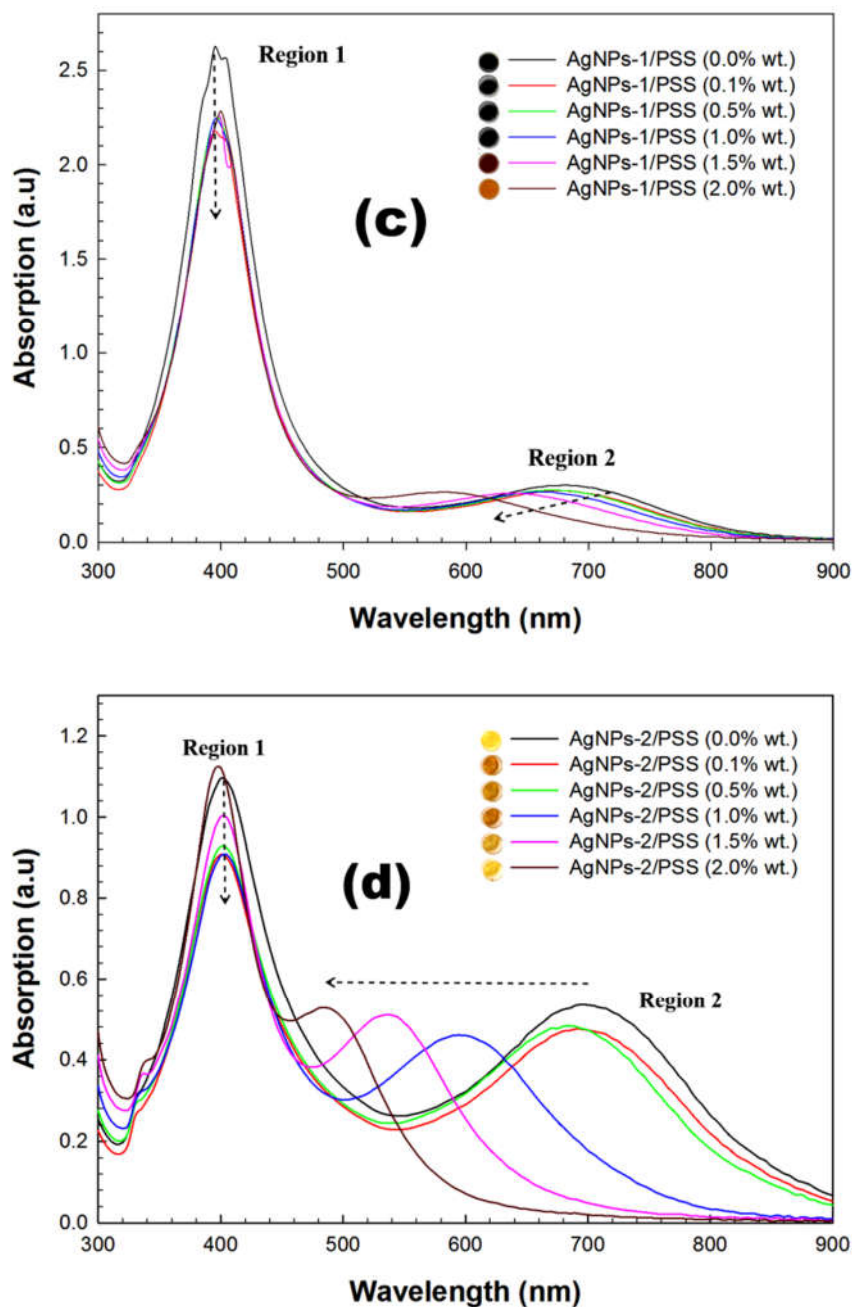
Figure 4.3: Evolution of UV-Vis absorption spectra of AgNPs sols with different (PEI & PSS) weight concentrations; (a) AgNPs 1-PEI, (b) AgNPs 2-PEI, (c) AgNPs 1-PSS and (d) AgNPs 2-PSS sols formation at 120 min after polymers addition (AgNPs sols photograph can refer the AgNPs multicolour map at figure 4.2).

The effect of PEI concentrations was further studied in order to understand the colour extinction of silver sols due to adsorption onto its surface. The observed results are depicted in Figure 4.4 as percentage reduction of absorbance

AgNPs/PEI's series. From the reduction curve, there is only slight decrease to 75% for AgNPs-1/PEI compared to 77% for AgNPs-2/PEI of 0.1 wt.% PEI but shows 99% of reduction for both at 2.0 wt.% from maximum absorption after chemical reaction for 120 min. 120 min was chosen as a control time measurement because the AgNPs-polymer only need 120 min to complete the reaction, which is the colour solutions fully change. Apart from the graphs, at the constant sol of AgNPs, the curves clearly demonstrate that AgNPs-2/PEI exhibit better reduction of absorbance peaks compared to AgNPs-1/PEI curves, respectively. Lower reaction rate of AgNPs-1/PEI may be attributed to bigger particles size compared to AgNPs-2/PEI that might need more time to cover AgNPs' surface. Furthermore, with increasing PEI concentration in solution, the reaction rate and colour extinction would increases spontaneously as shown in Figure 4.4.
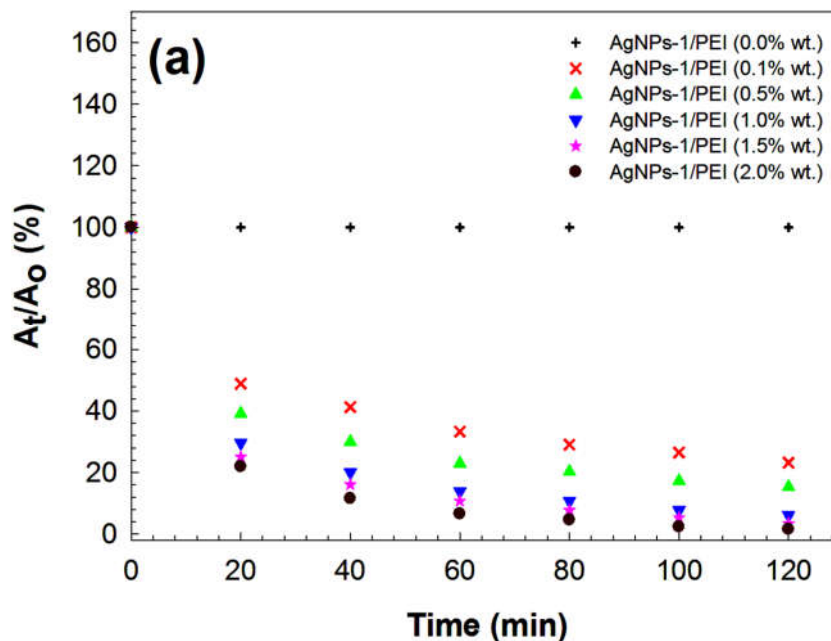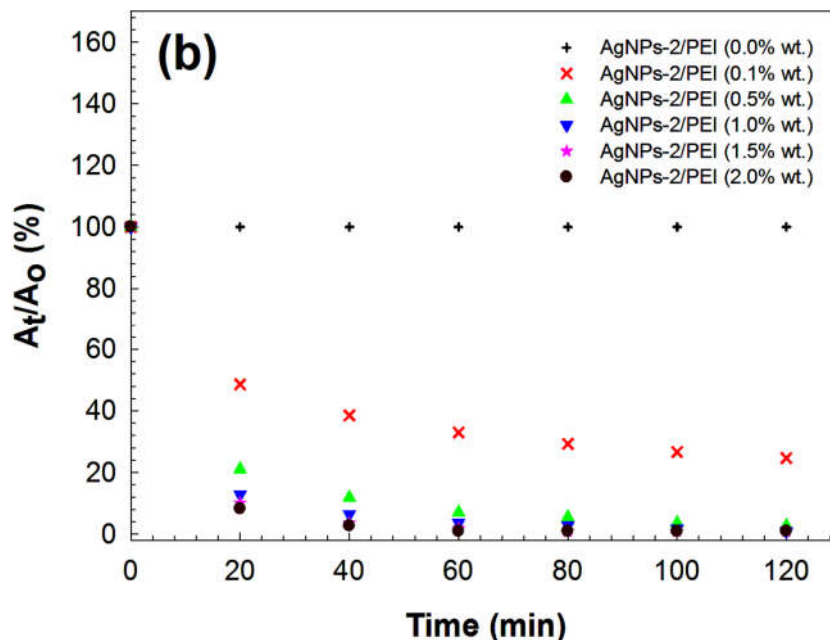
Figure 4.4: Effects of PEI addition on the absorbance peak at 400 nm of (a) AgNPs-1 and (b) AgNPs-2 sols formation at different time intervals. Reaction conditions: (+) = 0.0 wt.%, (×) = 0.1 wt.%, (▲) = 0.5 wt.%, (▼) = 1.0 wt.%, (☼) = 1.5 wt.% and (●) = 2.0 wt.%.

4.3.4 Characterization of silver nanoparticles

Size distribution of silver nanoparticles

In order to investigate the dimension of AgNPs, PEI, PSS, AgNPs/PEI and AgNPs/PSS particles, dynamic light scattering measurements were conducted at room temperature. Figure 4.5 depicts the variation of DLS volume-hydrodynamic size distribution of the AgNPs, polymer (PEI & PSS) and AgNPs/polymer complexes. The measurements were made by calculating average of three measurements for each sample and show AgNPs-1 with 17 nm and AgNPs-2 with 2 nm. On top of each graph legends where no addition of polymer at all in the solutions, AgNPs formed which both demonstrated that the effective sizes for AgNPs-1 and AgNPs-2 were formed due to its sol's colour as shown in Figure 4.5(c)-4.3(f) [105]. One of the possible reasons for the difference in size of AgNPs produced could be attributed to different concentration of $NaBH_4$ interacting with silver precursor, with different nucleation rate according to Lamer and Dinegar model [113].
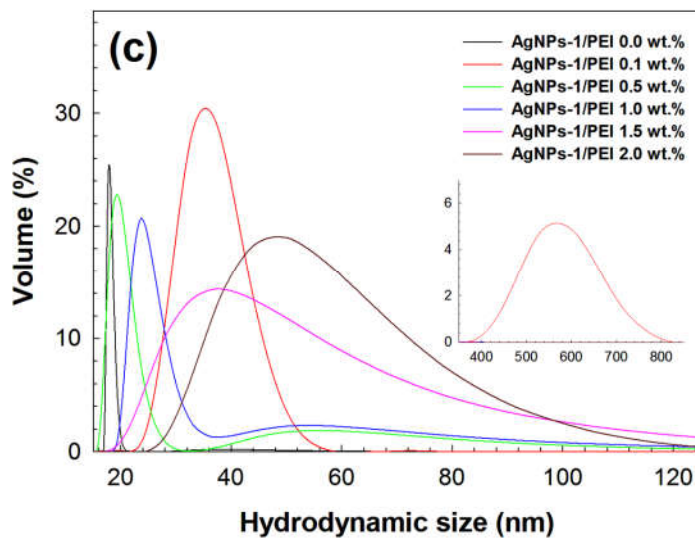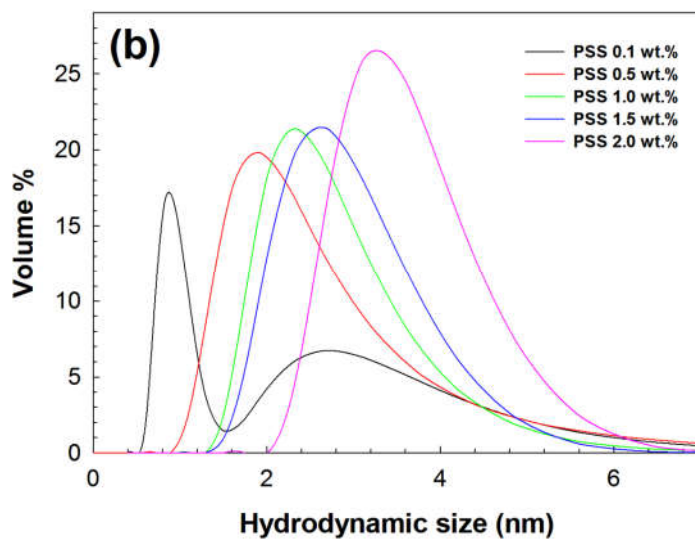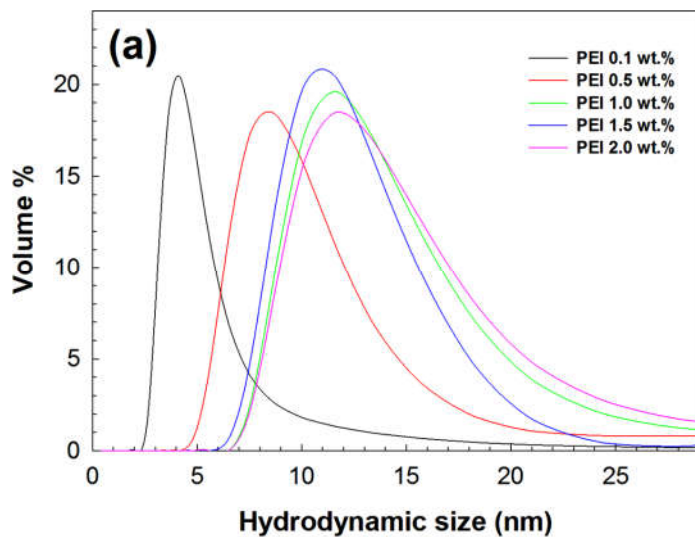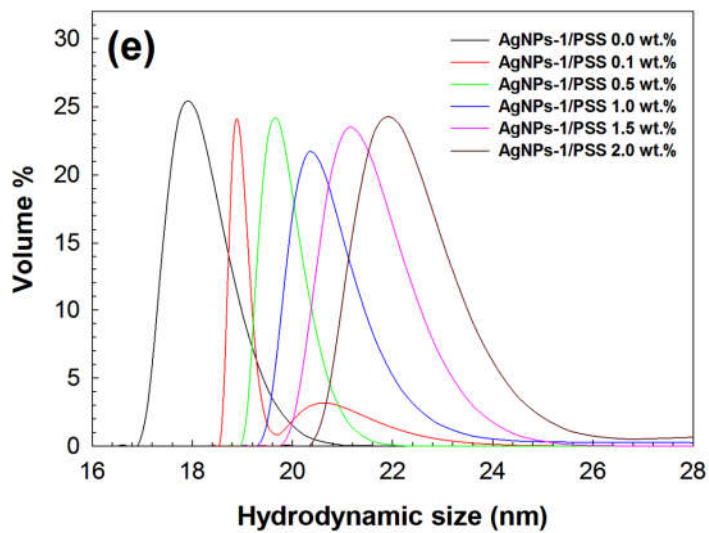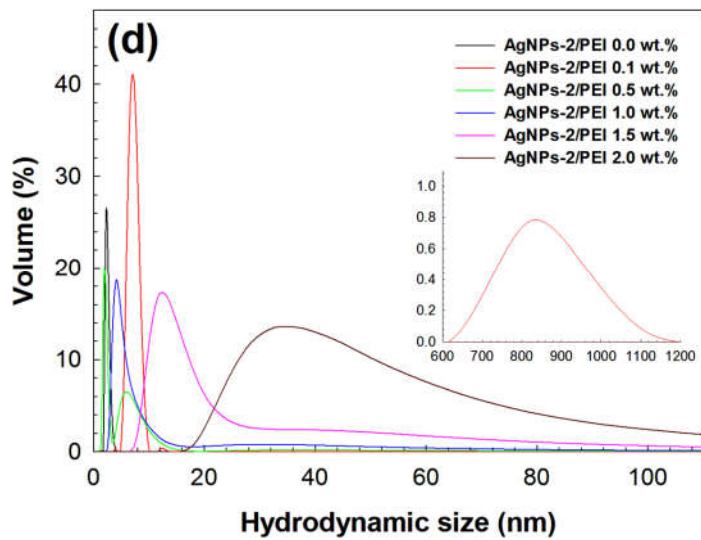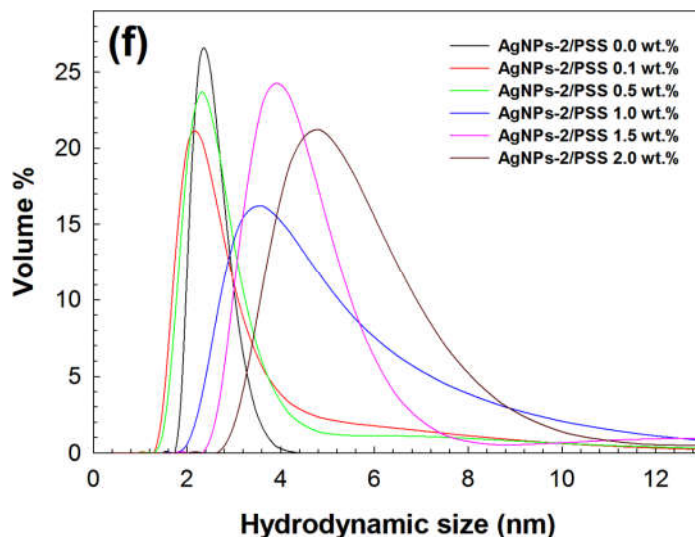
Figure 4.5: DLS size distribution of AgNPs/polymers complexes at 120 min. Control sample: (a) PEI and (b) PSS. From (c) to (f), the final concentration of polymers (PEI & PSS) was 0, 0.1, 0.5, 1.0, 1.5 and 2.0% wt. with the different effective particle sizes of AgNPs/PEI and AgNPs/PSS, respectively. The inset graphs represent (c) AgNPs-1 PEI 0.1 wt.% and (d) AgNPs-2 PEI 0.1 wt.%.

The DLS results of the hydrodynamic size of PEI and PSS colloids of control samples are shown in Fig. 4.5 (a & b). Another results obtained by mixing monodisperse of both AgNPs-1 and AgNPs-2 with polymers are shown in Fig. 4.5(c-f). According to the DLS spectra, there was a range of nanoparticles present, with hydrodynamic diameters including polymer from about 8 nm to 1.2 μm, assuming a hydration layer of polymer surrounding the AgNPs.

There were also a small proportion of aggregates present for 0.1 wt.% AgNPs/PEI sample as shown in Fig. 4.5c and 4.5d (inset). It is notable that DLS characterization can measure AgNPs sizes including singular and aggregation forms, which is the effective hydrodynamic diameter of AgNPs/polymer complexes that rose to larger sizes upon increasing the amount of polymer in the solution, therefore reflecting a wider particle size distribution due to the association of AgNPs with discrete polymer complexes although a minor particle aggregation cannot be ruled out [114].

Absorption of Silver Nanoparticles
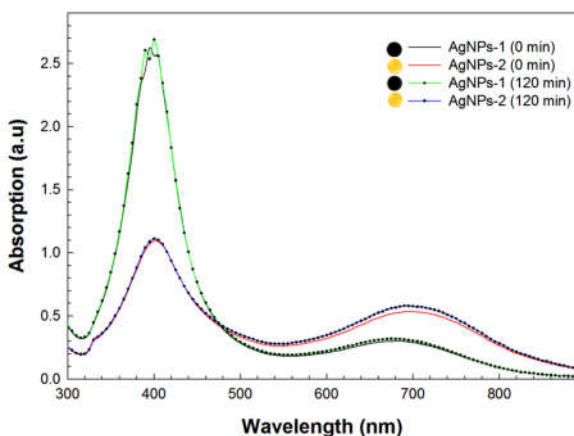
Figure 4.6: UV-Vis spectrum of silver nanoparticles (AgNPs) absorption with different size/colour at 0 and 120 min.

A fine control of AgNPs exhibit colourful range, depending on the shape and size of the particles and dielectric constant of the surrounding medium due to excitation of surface plasmon resonance band in the visible spectrum, which give rise to such intense colours [94]. As the borohydride solution was mixed with aqueous solution of the silver nitrate and citrate, it started to produce the colour due to reduction of silver ion (Ag+); which indicated the formation of AgNPs [105]. It is generally accepted that UV-Vis spectroscopy could be used to examine size and shape-controlled nanoparticles in aqueous solution by comparing between UV-Vis spectra fitting of the colloidal nanoparticles and theoretical calculation of absorption spectra [115]. Figure 4.6 shows the UV-Vis spectrum recorded from the reaction medium without polymer concentration and its stable for months.

The absorption spectra of AgNPs sols in Figure 4.6 shows two spectral regions consisting a single sharp surface plasmon resonance band at 400 nm (region 1: corresponds to spherical shape AgNPs) and broad peak at 700 nm (region 2: corresponds to rod, triangle, or hexagonal shapes AgNPs) [94]. The two width regions of this spectrum are due to the presence of more than one SPRs related to transverse and longitudinal electron oscillations. The most characteristic part of AgNPs sol is a narrow plasmon absorption band observable in the wide range of energy in the range of 350-550 nm regions [94]. The peak appearing at 700 nm band is indicative of new shape forming new localized surface plasmon resonance spectra [105]. Moreover, the

differences in intensity are consequence of the proportionality of the optical efficiency to the volume of the nanoparticles. Besides, size effects also have an influence over the intensity because surface plasmon resonance damping becomes more relevant as its governed by the electronic surface spill-out as the size of the AgNPs becomes small [116].

4.3.5 Role of polymers and reaction site to the growth of Ag-nanocrystals

Polymers can stabilize the particles through electrostatic forces [120], hydrogen bonding [121] and van der Waals forces [122] between functional groups and inorganic particles. Thus, various properties such as oxidation-reduction potentials [123], quantum efficiencies [124], reaction mechanisms [120], size [94], and shape [105] of inorganic chemicals are changed in the presence of polymers. In the present study, the role of polymers (PEI & PSS) could be explained by incorporation of polymers onto the surface of AgNPs through schematic shown in Figure 4.7. Equation 4.1 represents the formation of Ag^+-citrate complexes by silver nitrate and trisodium citrate reaction. In the second reaction (Equation 4.2), with controlling pH level in the solution by $NaBH_4$ making Ag^+-citrate complex decomposes in one step one-electron oxidation reduction mechanism to produces AgNPs/citrate and shield the AgNPs surfaces. In the final step, the polymerization of the formed AgNPs/polymer complexes with PEI and PSS occurred by replacing or binding together with citrate shell and seal onto AgNPs surfaces (Equation 4.3). The sulfonate group of PSS adsorbs onto AgNPs surface via electrostatic interaction of R-COOO-/Ag+ resulting yellow-shift in RCOOO-AgNPs sols colour as shown in HrTEM Figure 4.9(b). Apart from that, amine groups in PEI chains have strong tendency to coordinate with AgNPs or AgNPs-citrate forming AgNPs/PEI or AgNPs/citrate/PEI complexes as shown in Figure 4.9(a). Therefore, AgNPs are attached at the primary and secondary amine groups of PEI through protonated process as shown in Equation 4.3. The sols' colours turn to colourless once the reaction between AgNPs @ AgNPs-citrate and PEI functional groups completed. The proposed mechanism is further supported by the Raman spectrums in Figure 4.10.

(4.1)

(4.2)

(4.3)
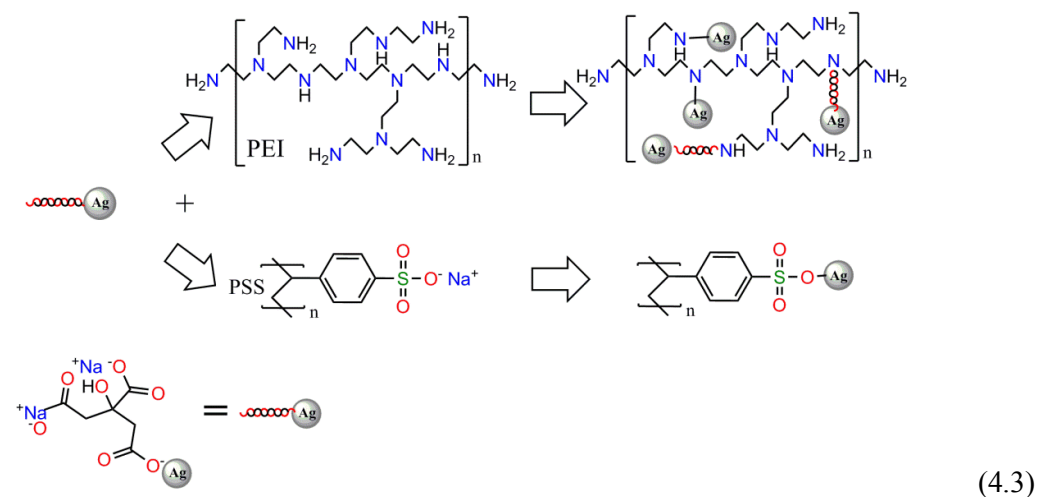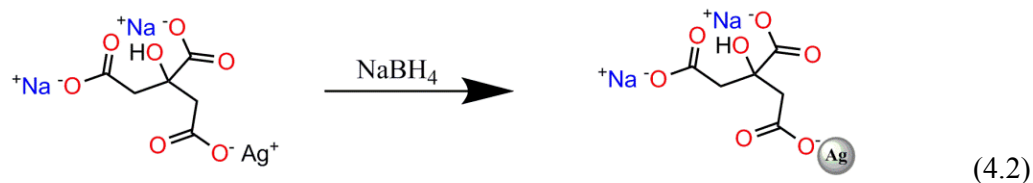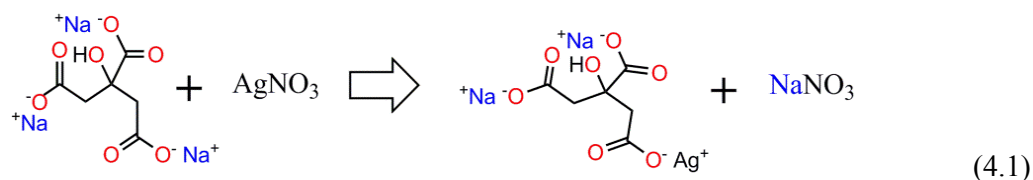
Figure 4.7: Schematic illustration for AgNPs/PEI's and AgNPs/PSS's complexes

Basically, the aspect in hue change is the polymer segment and AgNPs attractive contact strength, the absolute value of which controls the aggregation state. There are three levels of the polymer segment and nanoparticles attractive contact between AgNPs and polymer; at low attractive contact strength values or surface coverage is much below the saturation, suspensions would be destabilized due to polymer bridging and depletion attractions making AgNPs aggregate into compact clusters, therefore thin layer of sediment appeared at the bottom of vials after complete the reaction (1 day) [125]. At the intermediate interfacial cohesion strength, a net repulsive interparticle potential of mean force (PMF) between the AgNPs and polymer produces thermodynamically stable "bound polymer layers" form around nanoparticles, making it stable and fully dispersed at all particle volume fractions [125]. At the large values, polymers form tight bridges between the AgNPs, resulting in phase separation or formation of non-equilibrium polymer particle networks [125].

With a steady increase in hydronamic volume with polymer concentration, a tight bridges imply multiple particles in a single hydronamic space and phase separation occur but 2.0 wt.% is not enough to form phase separation in this case. Therefore, in this experimental system, there is favourable adsorption energy for polymers on AgNPs surfaces as PEI and PSS adsorbs to the AgNPs surfaces proportional to polymers concentration as the polymer-particle attraction strength in low concentration is much weaker than in high polymer concentration.

4.3.6   Morphology of AgNPs

SEM studies were performed to confirm further the AgNPs in the polymer, as presented in Figure 4.8. The low-magnification SEM images in Fig. 4.8 (a & c) prove that larger-sized nanoparticles (AgNPs-1) can produce a more sensitive signal [106].
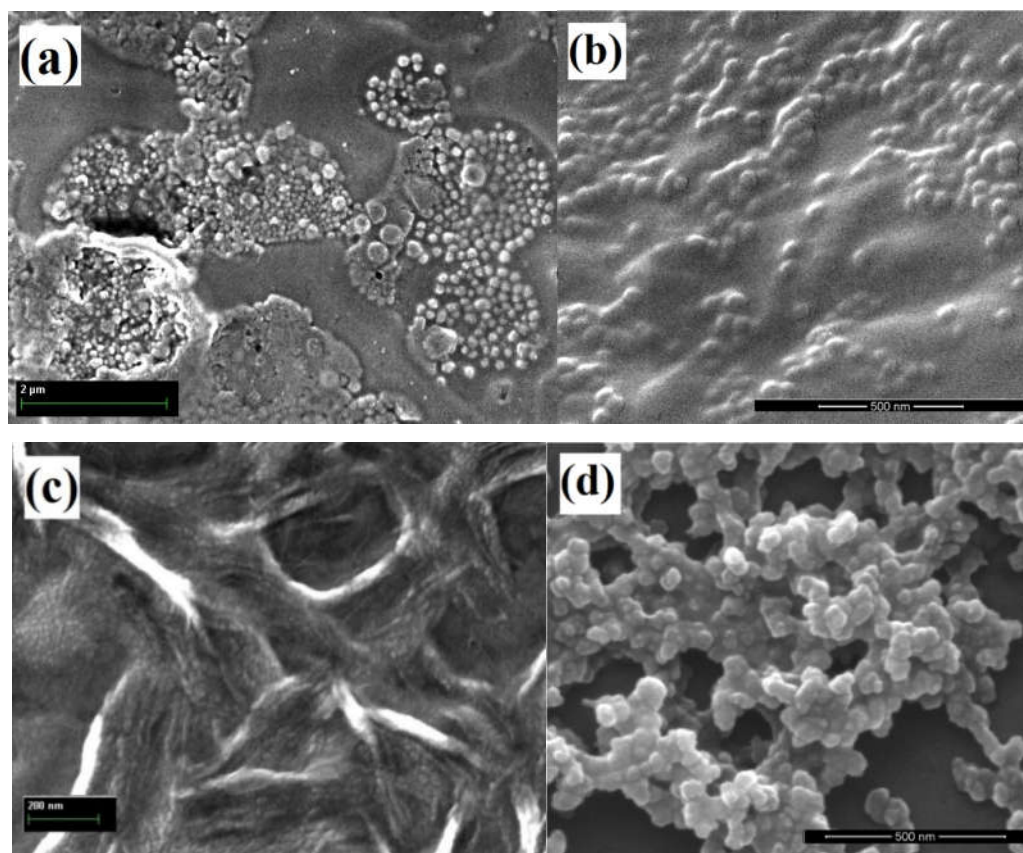
Figure 4.8: SEM micrographs that show the formation of AgNPs/polymer's complexes with different AgNPs sizes and 2.0% wt. of polymer concentration: (a) AgNPs-1/PEI, (b) AgNPs-2/PEI, (c) AgNPs-1/PSS and (d) AgNPs-2/PSS.

The aggregates may be produced from the nanoparticle aggregation when the colloid was drying. It is interesting to note that the hydrodynamic diameters of AgNPs in the presence of PEI and PSS measured by dynamic light scattering (DLS) experiments were much smaller than the SEM measured diameters of AgNPs/polymer, indicating the formation of a much bigger volume of PEI & PSS-involved assembly structures and many AgNPs were contained in such AgNPs/polymers assembly structures. Hence, the arrangement of AgNPs in the polymer layer will be confirmed using HRTEM micrographs as shown in figure 4.9.
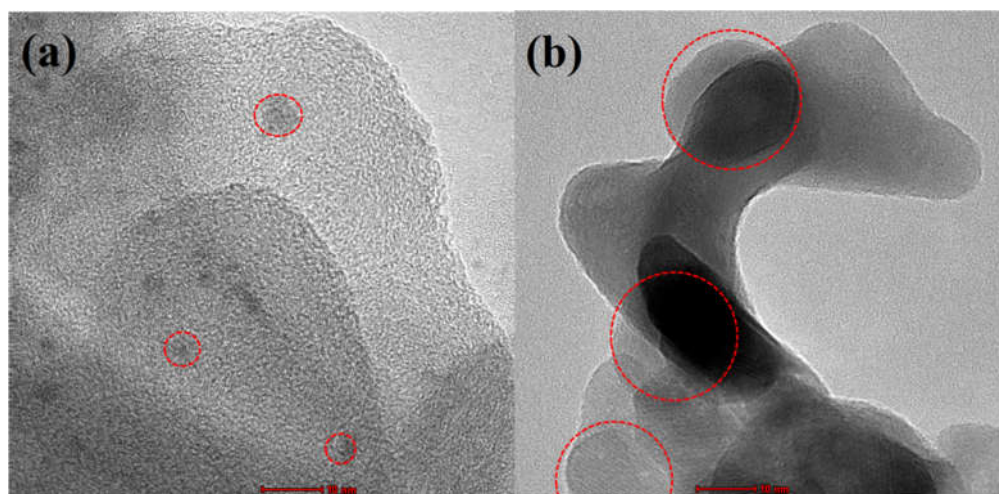
Figure 4.9: HRTEM micrographs that show the selected formation of AgNPs/polymer's complexes with different AgNPs sizes and 2.0% wt. of polymer concentration: (a) AgNPs-2/PEI and (b) AgNPs-1/PSS. (200 kx)

HRTEM micrographs were characterized to further investigate the AgNPs in the polymer, as shown in Fig. 4.9. Here, the diameters of AgNPs-1 and AgNPs-2 in the presence of PEI and PSS show the scale are slightly different from DLS measurements, as the refraction index of the formed complex is unknown and due to the fact that the sample distribution is not perfectly monodisperse [126]. Furthermore, the reason for the gradual reduction of absorbance peaks (UV-Vis) of AgNPs/PEI's series in Fig. 4.6 could be explained due to the adsorption of thick PEI layer onto its surface as shown in Fig. 4.9(a). Meanwhile, strong van der Waals forces between the AgNPs surface and PSS functional group results in the particles packed close to each other as shown in Fig. 4.9(b). This result is supported by Raman spectra as shown in Fig. 4.10.

4.3.7 Chemical bonding
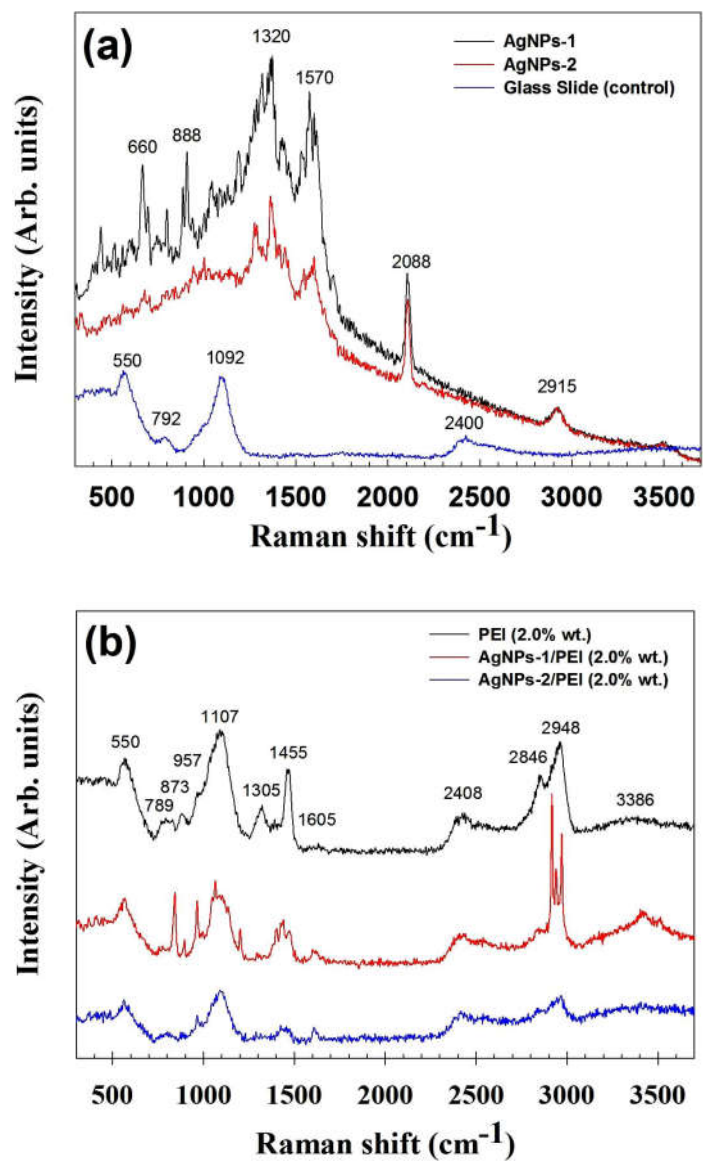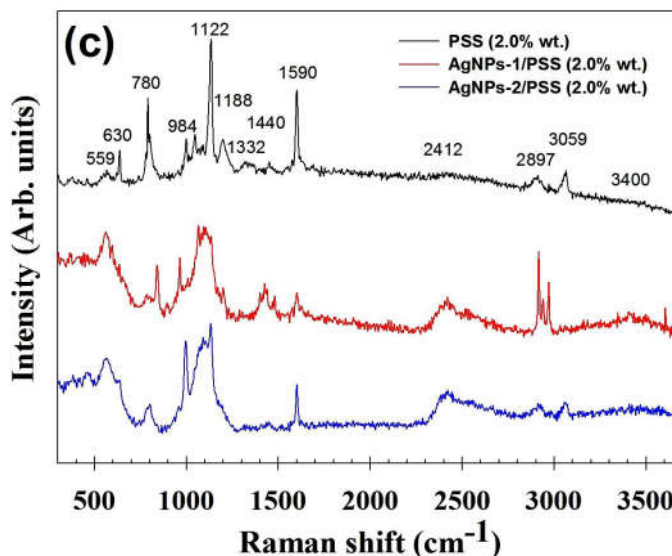
Figure 4.10: SERS spectra with 532 nm laser excitation for (a) AgNPs & Borosilicate glass slide (control), (b) AgNPs/PEI and (c) AgNPs/PSS.

Figure 4.10 shows the SERS spectra of the polymer adsorbed on AgNPs surface acquired using a 532 nm laser beam. The SERS spectrum for single PEI 2.0% wt. The SERS intensity spectrum obtained for both AgNPs in Figure 4.10(a) are quite high due to resonance effect induced by a possible charge transfer attributed to the interaction of citrate ions with the AgNPs surface [135]. The existence of a charge transfer responsible for the resonant effect observed in Fig. 4.10(b & c) as the intensity peaks reduced in the spectra is additional proof demonstrating the establishment of a strong interaction between amine groups (PEI) and sulfonate group (PSS) with the AgNPs and thick layer of both shell leading to a change in the PEI protonation state and functionalized sulfonate groups for PSS. Apart from that, AgNPs structural marker bands mainly appear at 450 and 1570 cm^{-1} attributed to υ(Ag-O) and COO-Ag vibrations [136]. The band features at 2088 cm^{-1} was attributed to the ν(C-N) symmetric stretches shifted to lower wavenumbers that corresponded to -NO$_3$ functional group, resulted of replacing citrate with amine group [129]. The principal band is at 1320 cm^{-1}, which is assigned as the carboxylate symmetric stretching mode from citrate, ν_s(COO) [136]. When compared with the Raman spectrum of trisodium citrate in solution (~1417 cm^{-1}), this band is broadened and blue-shifted, indicating interactions between the carboxylates and the AgNPs surface [136]. This is also supported by the intensity decrease of the bands at 1291 and 1243

cm^{-1} which are associated with the carboxylate deformations, $\delta(COO)$ [136]. The bands at 888 cm^{-1} are assigned to the $\upsilon(C-C)$ aliphatic chain and $\upsilon(C-O-C)$ symmetry vibrations modes also from citrate. Furthermore, the peaks in the 2830-3000 cm^{-1} regions are attributed to the symmetric and asymmetric C-H stretching modes of the -CH$_2$ and -CH$_3$ groups [129]. The band appear at 660 cm^{-1} (AgNPs 1-Black line) due to $\upsilon(C-Br)$ vibration modes, which is ionic bromine from KBr interact with citrate at the same point [135].

Figure 4.10(b)-black line displays an intense band at 1455 cm^{-1} that is clearly attributed to $\delta(CH_2)-\delta(CH_3)$ asymmetry bending. Other bands appearing at 1305, 1107, and 957 cm^{-1} are also attributed to methylene groups, in particular to CH$_2$ wagging and twisting motions, because these bands are also found in Raman spectra of polyethylene [127] and ethylene diamine [128]. The band of CH$_2$ appears at 1305 cm^{-1} for black line of figure 4.10(b) become flat when the polymer is adsorbed on the AgNPs surface due to aliphatic moieties [129]. The band at 550 cm^{-1} can be attributed to the C-N bond, which together with the 1107 cm^{-1} band intercepted with borosilicate glass slide of $\upsilon(Si-O-Si)$ band (see Fig. 4.10(a)), making it one of the higher intensity peaks in the spectrum. The weak bands observed at 789-873 and 1605 cm^{-1} appear due to the rocking vibrations of ethylene groups and the amine bending ($\delta(NH_2)$) from the PEI chains [130]. The weak band appeared at 3386 cm^{-1} assigned to N-H stretch vibration of PEI demonstrated that PEI was successfully grafted to AgNPs surface. However, the adsorption of PEI on AgNPs surface could create the formation of a Lewis acid-base interaction between the amine groups and the AgNPs metal, thus leading to a marked change in the Raman spectrum [130].

The asymmetric (ν_{as}) and symmetric (ν_s) stretching motions of C-H bands are slightly shifted up and downwards in AgNPs/PEI spectrum due to the presence of amino groups in its complexes structure (Figure 4.7). These modes appear at 2846 and 2954 cm^{-1} shifted when the polymer is adsorbed on the AgNPs's surface. Furthermore, the shift of the amino band between 1400 and 1610 cm^{-1} in the spectrum suggests a change in the protonation state of these groups as a consequence of the interaction with the AgNPs surface, indicating that an aminolysis reaction or an electrostatic interaction had taken place between both sides [130]. Moreover, the above bands may be due to $\delta(NH^{2+})$ in protonated secondary amines or $\delta(NH^+)$ in

protonated tertiary amines [130]. This interaction mechanism is the most probable one considering that the residual charge of the AgNPs surface is negative as treated with citrate and the positive charge of the PEI is localized on the amino groups. The band shifts observed at the spectra suggest the existence of different amino groups (primary, secondary, and tertiary) of PEI on the AgNPs surface could be either adsorbed onto the AgNPs surface forming ionic pair (through electrostatic interaction with negative charges existing on the surface together with citrate or a coordination complex direct with the AgNPs surface) or surrounded by aliphatic groups with a different conformation [131]. The amide bond linking the citrate to PEI generally comes in the near region of 1605 cm^{-1} as shown in Figure 4.10(b) (AgNPs 1-red line) attributed to COO-Ag vibrations. In the present spectrum, it appears to be overlapped with the N-H bending mode as the number of amines is comparatively higher in the compound. Thus, the reason why the AgNPs-PEI solution could not hold the sols' colour is because of interaction between citrate and amine group of PEI.

Figure 4.10(c) is the prominent SERS spectrum of AgNPs and PSS 2.0% wt., with two sharp bands at 1122 and 1590 cm^{-1} corresponding to υ(C-C) aliphatic chain and υ(C=C) vibrations of aromatic ring, could be clearly observed in the PSS spectrum attributed to molecular benzene, respectively [132]. Other than that, the bands at 2897 and 3059 cm^{-1} also attributed to benzene ring due to υ(C-H) and υ(=(C-H)) vibrations, respectively [133]. Other bands appearing at 630 and 780 cm^{-1} are attributed to υ(C-S) aliphatic vibrations due to sulfonate functional group [134]. Moreover, the band at 1100 cm^{-1} corresponds to the υ(C-S) aromatic vibrations also found in the spectrum [134]. The peak at 1440 cm^{-1} can be assigned to C_α=C_β symmetric vibrations and 1332 cm^{-1} to C-C stretching deformations of PSS [134]. At the same concentration, some features of PSS are underneath the major peaks of AgNPs/PSS. These SERS peaks of AgNPs/PSS broadening agree well with the result of AgNPs and adsorbed PSS coexistence (red & blue lines).

4.4   Conclusion

In summary, we have successfully synthesized and observed a hue changing of AgNPs sols as a function of PEI and PSS concentrations with a constant

concentration of silver precursor using a chemical reduction method. It has been demonstrated that a fine control of both PEI and PSS concentrations in different sizes of AgNPs made it possible to changes or reduces its color due to interaction between AgNPs and specific polymer functional groups. Moreover, the plasmonic resonance of AgNPs will depend on several parameters which are the size of the AgNPs, the geometry of the AgNPs (not include in this study) and the physical properties of the medium in which the AgNPs are dispersed (polymer addition). Thus, the reaction sols of AgNPs shift to yellow and colorless quickly at higher polymers concentration. Additionally, the rate of color shifting also depends on the concentration levels of polymers addition. Based on the comprehensive SERS experiments, it is concluded that the existence of different amino groups of PEI adsorbed onto AgNPs surface either by interaction with citrate that react as a linker between AgNPs and PEI or a coordination complex direct with the AgNPs surface. In contrast, the SERS peaks of AgNPs/PSS broadening around sulfonate group agree well with the result of adsorbed PSS onto the AgNPs surfaces. SERS results were supported by absorbance spectra, which suggest that adsorption of PEI and PSS on the AgNPs surface results in a decrease in the maximum absorption intensity at violet region due to decreases of surface plasmon resonance, resulting in colorless and yellow sols of both AgNPs/PEI and AgNPs/PSS at the end of experiments due to ligand substitution depending on the relative strength of the AgNPs-amine or AgNPs-sulfonate bonds, and the stability of the departing and incoming ligands.

Chapter 5

5. Impact of Composition on Radio-Photoluminescence Glass Dosimeters

5.1 Introduction

Radiation is one of the energy and all humans are exposed to radiation every day direct or indirectly. Therefore, radiation exposure levels must be measured to prevent everyone from exceed dose limit and protect against possible detrimental effects of radiation. Other radiation affects include ionization, scintillation, and luminescence when radiation interacts with matter. By detecting these phenomena from the response of dosimeters after exposure, one can acquire an understanding of the types and the intensity of the radiation. For that to happen, a radiophotoluminescent glass detector (RPLGD) was developed by Schulman and co-workers in 1951. In brief, RPLGD is a prospective tool intended for dosimetric control and a solid-state dosimeter produced based on glass random network model. They possess linear dose sensitivity in a wide gamma and X-ray spectral region. It is reported that in phosphate glasses, linkages like P-O-…Na^+ or P-O-…Li^+ form and these linkages act as localized levels in the optical gap of the glasses and can trap the electrons. Such levels are generally known as luminescence centres (L-centres) or colour centres [64]. Recombination of electrons form this level with the holes in the lower levels leads to light emission. In a multi-component glass, there can be a variety of colour centres depending upon their concentration in the glass where a broad emission spectrum is observed. For that reason, phosphate based glass was chosen due to its ability to accommodate large concentrations of active ions without losing their useful properties of the material [136]. Moreover, phosphate glasses are relatively easy to prepare and offers a large range of compositional possibilities, which facilitates in tailoring the physical, chemical and optical properties of interest for dosimetric applications [4]. The RPLGD made of silver-activated phosphate glass is an accumulation-type detector of ionizing radiation [4]. RPL centres produced in bulk by ionizing radiation have high stability, except against thermal annealing. Once

trapped, the centres of luminescence will never disappear unless the glasses are annealed at high temperatures of about 400 °C. Therefore, this product gives some excellent features such as repeatable measurement [4]. The relationship between dose and response will be a function of the trap density, partly governed by the activator concentration and the mobility of free electrons/holes within the lattice or forbidden energy level. Basically, when the glass is exposed to ionizing radiation, electron-hole pairs are produced and will be trapped within forbidden energy level to form luminescence centres in the phosphate glass [64]. After a preheating process at an appropriate temperature [137], RPL photons of approximately 635 nm in wavelength which is orange light are emitted upon exposure to UV light. Then, they will return to luminescence centres because it is a stable molecular energy level. The phenomenon is called radiophotoluminescence (RPL). Radiation dosage is measured with the formation of a RPL centre that is associated with activator ions exposed to ionizing radiation at room temperature. The RPL glass detector has some advantages compared to thermoluminescent detectors [16]. Based on the Cheka report [83], a long-term experiment confirmed that the RPLGD would not cause a fading effect. Therefore, RPLGD is suitable for long-term dose monitoring or environmental radiation detection. In addition, the RPLGD could be read infinitely because the UV laser light does not eliminate colour centres in glass substance of RPLGDs. Moreover, the RPL response exhibits a high sensitivity and linearity over a wide dose range [135]. The RPL measurement can be performed repeatedly without fading [16]. When errors occur, RPLGD signals can be re-analysed to ensure the reliability of results. Therefore, the research on RPL glass arouses people's interests with the extensive application of ionizing radiation such as in medical, industrial and aerospace application.

Less is known about the effects of activator content on phosphate glass properties, including dosimetric properties. Andreeva and group (1985) elucidated the influence of activator concentration on the dosimetric properties of RPL glasses [138]. The activator content of the phosphate glass has an important effect on the build-up performance; in general, increasing activator content accelerates the build-up, while a decreasing content retards build-up. In Yokota and Imagawa report, they found that phosphate oxide hole center (POHC) is transferred to Ag^+ ion (activator

ion) and this process is the main reason of RPL build-up [19]. The numbers of Ag^+ ions are related to energy levels in RPL centres and the numbers of electron trap(s). The numbers of electron trap(s) increase with increasing numbers of Ag^+ ions. However, lower activator content may be required to reduce the effective order of magnitude, so that heat treatment before dosimeter assessment may become necessary in any case. Moreover, excessive activator contents will decrease the penetration efficiency of the ultra-violet laser and increases energy dependence. Therefore, a proper ratio of activator content is required for the best luminescence and excitation efficiency [19]. In this study, different activator compound was added to a phosphate base glass to determine the characteristic properties suitable for RPL glass dosimeters. Furthermore, the influence of glass composition on the sensitivity to ionizing radiation and the RPL 'build-up' kinetics were also investigated in the present work. Therefore, improving dosimetric sensitivity and quality of glass by improving the design of base and activator composition in phosphate oxide glass was the main objective in this study. Thus, RPLGDs were prepared from reagent powders of P_2O_5, Li_2CO_3, $Al(OH)_3$, $NaNO_3$, $MgSO_3$, H_3BO_3, $Ti(OCH(CH_3)_2)_4$ with activator compound of $AgNO_3$ using wet melting method. Finally, the physical, optical, chemical properties and their correlation with the glass composition were investigated.

5.2   Experimental

5.2.1   Synthesis of radio-photoluminescence glass dosimeters

Here, all series phosphate glass dosimeters were prepared from reagent grade powders of anhydrous Ag, P_2O_5, Li_2CO_3, $Al(OH)_3$, $NaNO_3$, $MgSO_4$, TiO_2 and H_3BO_3. Phosphate glasses of an appropriate composition as given in Table 5.1 were synthesized. All samples were set with different nominal composition range (wt.%) to study differences of each element to glass properties. Control sample was set with Abd. Rahman's composition wt.% of glass [139].

Table 5.1: Chemical composition for making radiophotoluminescent glass dosimeter

No	Chemical content	Nominal composition range (wt.%) & label								
		A	AA	AB	AC	AD	AE	AB1	AB2	control
1	P_2O_5	60	71	73	75	77	90	73	73	74.4
2	Li_2CO_3	15	10	5	5	4	1	6	9	7.3
3	$NaNO_3$	8	5	2	2	1	1	3	4.5	2
4	$MgSO_4$	2	1	0	2	2.5	0	0	0	0
5	$Al(OH)_3$	4	5	6	8	9.5	5	7	7.5	9.3
6	H_3BO_3	1	1.5	1.5	2.5	3	1	2	2	2.7
7	TiO_2	3	2	8.5	2	0	0	5	0	0
8	$AgNO_3$	7	4.5	4	3.5	3	2	4	4	4.3
	Total	100	100	100	100	100	100	100	100	100

Glasses were prepared following the procedure as described in methodology in Chapter 3. Systematically, each glass dosimeters contain different weight composition of Na, P, O, Al, Li, Mg, Ti and activator Ag, weighed using a digital weighing machine with an accuracy of ±0.01 g. The batch powders were mixed with DI water and the well-mixed liquid batch was preheated at 120 ºC for 24 h in an alumina crucible to evaporate water. After that, the liquid batch was melted in an electrical heated furnace in atmosphere at a heating rate of about 10 ºC.min^{-1}, the temperature was gradually increased up to 600 ºC and kept at this temperature for 5 h. Once the mixture was liquidized, the temperature was then increased again to 1250 ºC and left for one hour to obtain the appropriate viscosity. After the refining process, the glass liquid was then poured onto a preheated graphite cylinder moulder and plate. At this point it then takes 12 h to complete the annealing process at 400 ºC to avoid internal mechanical stresses developed during solidification process. The phosphate glass series melting temperature program is illustrated in Figure 5.1.
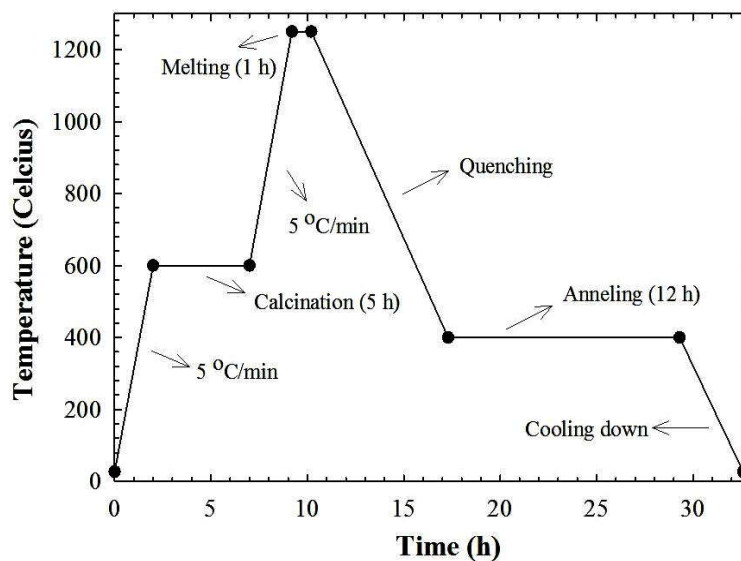
Figure 5.1: The fabrication of phosphate glass dosimeter series melting temperature program

For dosimetric measurement, the samples were irradiated with γ-radiation, delivered at 1.37 kGy/h (24/10/2016) using Gamma-cell (Gamma-excell-220, UKM) using a Co-60 source. In this work, the samples were irradiated such that the absorbed dose at 50, 100, 200 and 500 Gy were used for characterization. The glass samples were kept in a desiccator to prevent possible occurrence by moisture before further characterization. A schematic diagram of RPLGDs preparation was illustrated in figure 5.2.
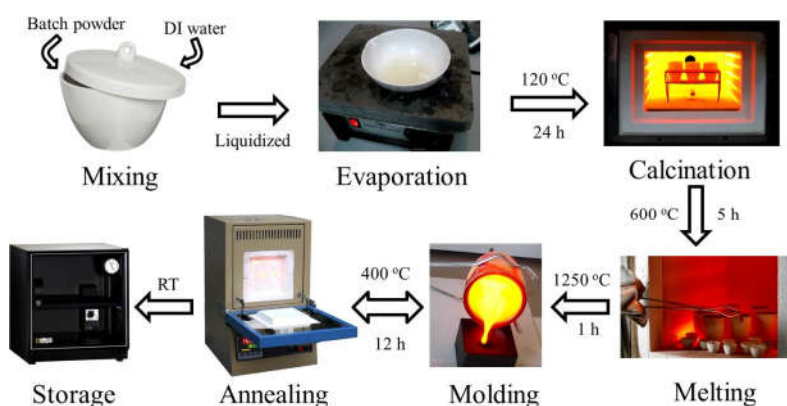
Figure 5.2: A schematic diagram of all series self-fabricated phosphate glass dosimeters preparation

Phosphate glass for the solid-state dosimetry was prepared from reagent grade powders of anhydrous P_2O_5, Li_2CO_3, $Al(OH)_3$, $NaNO_3$, MgO, TiO_2 and H_3BO_3 using a wet chemical method as shown in Figure 5.2. In brief, the weight chemical composition of the glass dosimeters was weighted using a digital weighing machine with an accuracy of ±0.01 g, then mixed with deionized (DI) water and the well-mixed liquid batch was preheated at 120 ºC for 24 h in an alumina crucible to evaporate water. After that, the temperature was gradually increased up to 600 ºC and kept at this temperature for 5 h for calcination process and the liquid batch was melted in an alumina crucible at melting temperature was between 1200 and 1300 ºC. Once the mixture was liquidized, the molten liquid was cast into a preheated cylindrical shape graphite mold which had been preheated at 400 °C for 30 min. At this point it then takes 6 hours to complete the annealing process at 360 °C in a second furnace to remove thermal strains in the glass. Finally, the resulting glass was polished and cut for the required measurements.

5.2.2   Thermo-Physical characterization

On this section; density, hardness and thermal properties measurements of each glass samples at room temperature were carried out as described in chapter 3. Cut and polished glass samples were used for these measurements.

Density

The densities of the glass samples (A, AA, AB, AC, AD & AE) were measured at room temperature using the Archimedes principle, and distilled water was used as the immersion liquid with an accuracy of ± 0.03 g/cm^3. Molar volume of the glass was also obtained from the density.

Hardness

The hardness of each phosphate glass samples was measured by the Rockwell Time TH320 in the present study. In this part, the control sample was used and one of the base components was manipulate to study the effect of aluminum and phosphorus pentoxide for glass hardness as this element were play as a key for glass hardness. Mirror polished surface of the sample to be indented was used for the measurement. The phosphate glass surface was penetrated by 10 kgf preload

followed by 60 kgf of major load addition without shocks. The HR values reported in this thesis are the average values of at least 10 independent indents made on each sample under identical loading conditions.

Differential Scanning Calorimetry

The chemical reactions and phase transition of glasses substance as a function of temperature were measured using differential scanning calorimetry (DSC 822E) technique. In this part, the control sample was used and one of the base components was manipulate to study the effect of aluminium, phosphorus pentoxide, sodium and silver for thermos analytical of glass as these elements were play as a key for measurement the glass phase transitions and decompositions temperatures. The difference in heat flow to the sample and a reference at the same temperature is recorded as a function of temperature. The reference is an inert material such as alumina or empty aluminium pan. The temperature of both the sample and reference were increased at a constant rate.

5.2.3 Structural characterization

For structural characterization, the powder forms of each glass samples were used for X-ray diffractometer (XRD) and Fourier-transform infrared spectroscopy (FTIR). The samples glasses were ground with mortar before characterization. The samples preparations were carried out as described in section 3.7, Chapter 3.

X-ray diffractometer

The structure of the phosphate glass samples were investigated using X-ray diffraction (Advance-8 Bruker X-ray diffractometer). A-series were used for observation and AB-series was chosen for comparison between before and after γ-irradiation with 200 Gy because only AB-series shows RPL after irradiation treatment. Each sample was made into a fine powder before diffraction analysis process. After that, 2g of sample's powder was deposited on the sample holder and the diffraction peaks analysis at scanning rate 5 °/min was carried out.

Fourier-transform infrared spectroscopy

FTIR technique was used to identify the chemical compound such as chemical bonds in a molecule or glass substance by generating an infrared absorption spectrum of a phosphate glass by collecting high spectral resolution data over a wide spectral range using Fourier transform infrared spectroscopy (Perkin Elmer/Lamda-950). A-series were used for general observation and AB-series was chosen for comparison between before and after γ-irradiation at 200 Gy because only AB-series shows RPL after irradiation treatment. The FTIR spectra of each glass were recorded over the frequency range 400-4000 cm^{-1} with a resolution of ~ 4 cm^{-1}. For sample preparation, the glass powder was placed on the KBr cell and then pressed using a mechanical press to form a transparent pellet which the beam of the spectrometer can pass through. Therefore, the pellet cell must be thin enough to ensure that the light can pass through.

5.2.4   Optical characterization

The optical characterization such as optical absorption, transmission and luminescence measurements of each glass samples were carried out as described in Chapter 3. Cut and polished glass samples having disc shape with thickness in the range 2-4 mm were used for these measurements. The samples were excited at 273 nm.

UV-Vis spectroscopy

The light absorption and transmittance spectra of the glasses were recorded on a Perkin Elmer lambda-35 spectrometer at room temperature between 200 and 1000 nm range with 2 nm resolutions. The measurement procedure was discussed in Chapter 3. In brief, the control sample was used and one of the base components was manipulate to study the effect of $NaNO_3$, Ag, $Al(OH)_3$ and P_2O_5 for penetration measurement of glass. After that one of the samples (control) was used to observe penetration ability of glass after irradiated from 50 Gy to 500 Gy. After that, the sample with 3.5 wt.% of Ag was chosen for absorption measurement after γ-irradiation between 50 to 500 Gy range. The glass samples in the form of a disc having diameter more than 12 mm and thickness in the range 2-4 mm were prepared and polished for optical measurements.

Photoluminescent spectroscopy

Excitation and emission measurements were performed at room temperature and RPL intensity was measured using fluorescent spectrophotometer model Varian Cary Eclipse (excitation: 350 nm). The RPL emitted from sample was observed in a direction perpendicular to that of the excitation beam and analysed using suitable filters with central wavelengths of 460 and 620 nm, respectively. All luminescence measurements were carried out at room temperature. Before and after AB-series of glass samples in the form of disc and powder were used in this analysis. After that, the effects of absorbed doses on RPL-intensity at varying absorbed doses were studied. Powder glass samples were put on the slide holder while disc samples were stick in the sample chamber of the instrument. Emission spectra were recorded with a resolution of 5 nm and all emission spectra were corrected for the detector response. Recycle samples of AB-series with same dose irradiation also done for recycles study.

5.3 Results and Discussion

One of the major findings of the present study was the significant influence of glass composition on the sensitivity to ionizing radiation and the RPL 'build-up' kinetics. Therefore, several samples have been made from different chemical compound and their physical, optical, chemical properties and their correlation with the glass composition were investigated.
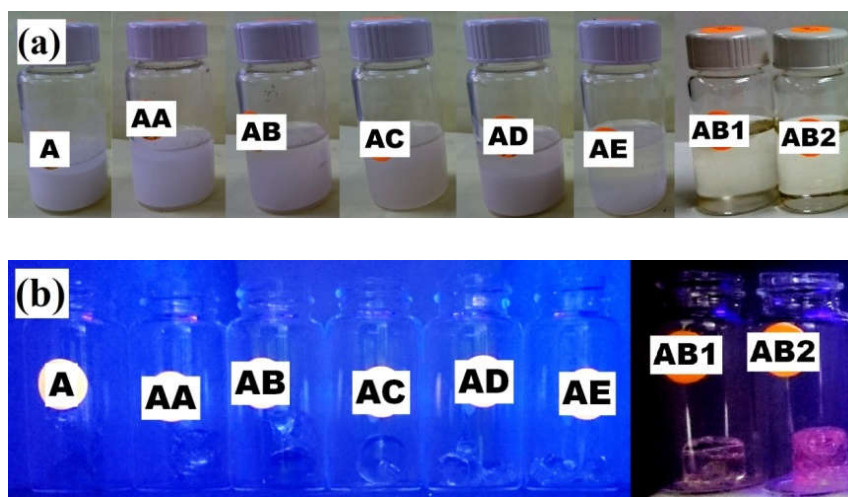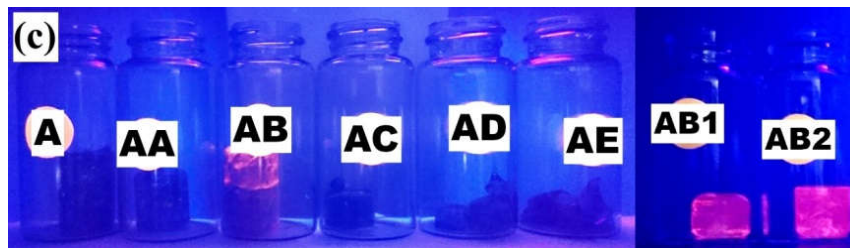
Figure 5.3: Photograph of (a) A-series of glass samples after evaporation process, (b) images of A-series glass samples before γ-irradiation treatment under UV light and (c) RPL emission images of A-series glass samples as a function of γ-irradiation treatment under UV light.

The RPL emission photographs as a function of γ-ray absorbed dose when the γ-ray irradiated A-series of Ag-doped phosphate glass is excited using UV light, are shown in Figure 5.3, where it shows the intensity of orange colour emission during UV light exposure. This result is proven with that of previous report in which RPL emission was related to its composition dependence [70].

5.3.1 Thermo-Physical properties

To understand the variation chemical composition and thermo-physical properties for RPLGD, several studies were carried out and various thermo-physical properties such as T_g, T_d, HR, ρ and V_m for the RPLGD samples are given in Table 5.2.

Table 5.2: Chemical contents (x), Tg, Td, HR, ρ and Vm for the different RPLGD samples

Sample	P$_2$O$_5$ content (wt.%)	Tg (°C)	Td (°C)	HR (HRA)	ρ (g.cm^{-3})	Vm (cm^3)
A	x = 60	382	406	98.7	1.79	70.83
AA	x = 71	394	420	99.6	2.04	62.20
AB	x = 73	393	418	100	2.12	59.85
AC	x = 75	393	418	99.8	2.17	58.47
AD	x = 77	392	417	99.4	2.22	57.16
AE	x = 90	383	409	98.7	2.58	49.18
AB1	x = 73	393	418	100	2.14	59.15
AB2	x = 73	393	418	100	2.14	59.15
Control	x = 74.4	393	418	100	2.15	59.05

Density

Density measurements of A-series samples were measured using Archimedes principle and the variations in ρ and V_m of the series glasses as a function of Ag content are shown in Figure 5.4.
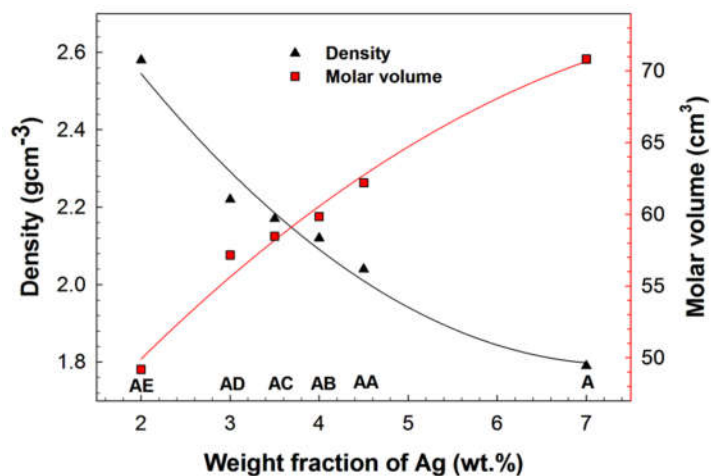
Figure 5.4: Variation of molar volume and density of A-series as a function of Ag molar concentration.

The glass density values of A-series samples are lightly shifted in the range 1.79 to 2.58 g.cm^{-3}, depending on molecular weight of each composition in the glass.

However, with a high amount of Ag in the vitreous network the density decreased down to 1.79 g.cm^{-3} value, possessing the lowest density value of the samples in this study. From figure 5.4, the ρ values decrease with addition of the Ag content. However, the V_m values increase with addition of the Ag content. The observed variation, particularly because of the molecular weight of elemental content in the glass, which is P_2O_5, TiO_2 and Ag are 142, 79.9 and 107.87 g.mol^{-1}, respectively and replacement of P_2O_5 by TiO_2 and Ag is expected to decrease the ρ while increase the V_m indicates the formation of strong and rigid bonding. Moreover, this indicates that for higher wt.% of Ag and Ti content, interconnections provided by Ag and Ti are not sufficient to overcome the depolymerisation of phosphate network, resulting in different outcome of ρ and V_m values, which make the glass network more rigid [140].

Hardness

The variations of hardness versus RPLGD with different chemical contents especially aluminium and phosphate pentoxide are shown in Figure 5.5. Al and P_2O_5 were chosen because these elements are important for strengthen the glass matrix and improve durability of glass. Ten measurements of Knoop hardness numbers were taken with a Rockwell indenter over the polished surface to obtain average hardness numbers glasses.
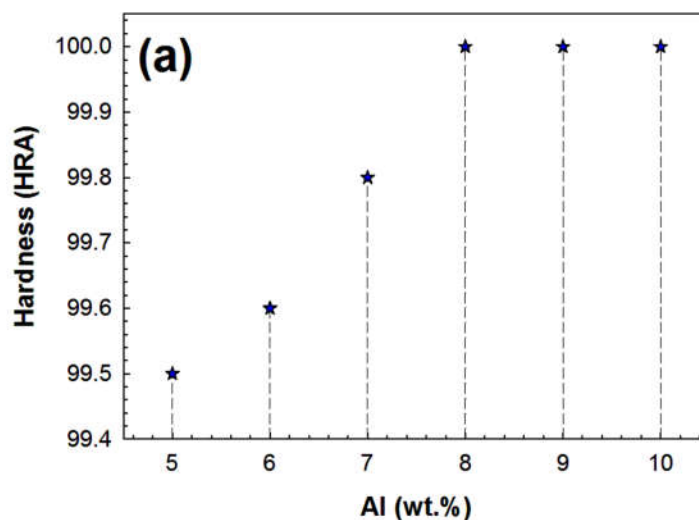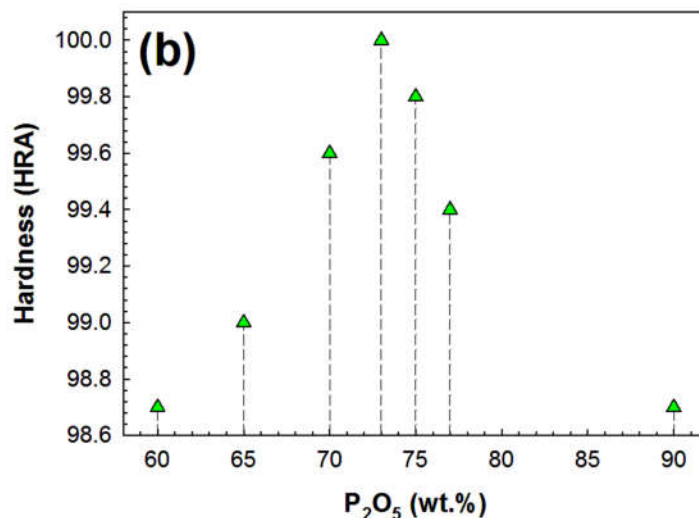
Figure 5.5: Distribution of Knoop hardness of RPLGD with different wt.% of aluminium and phosphorus pentoxide contents

Generally, the Rockwell values of glasses investigated vary from 98 to 100 HRA, which are dependent on the glass composition. From the Figure 5.5(a), it is observed that increasing the wt.% of Al results in increasing the hardness values. Al is known to improve durability, but it is also known to raise the glass transition temperature. Therefore, the optimum wt.% of Al for RPLGD system emerges to be in the range of 8-9wt.%. With other elements fixed, the hardness values were increasing until 73 wt.% of P_2O_5 and decreases after that value as shown in Figure 5.5(b). Hence, optimum P_2O_5 percentage for this RPLGD appears to be approximately 73%.

Differential scanning calorimetry

The thermos-analytical measurement for A-series phosphate glasses were done by differential scanning calorimetry analysis including measurement the glass phase transitions and decompositions temperatures.
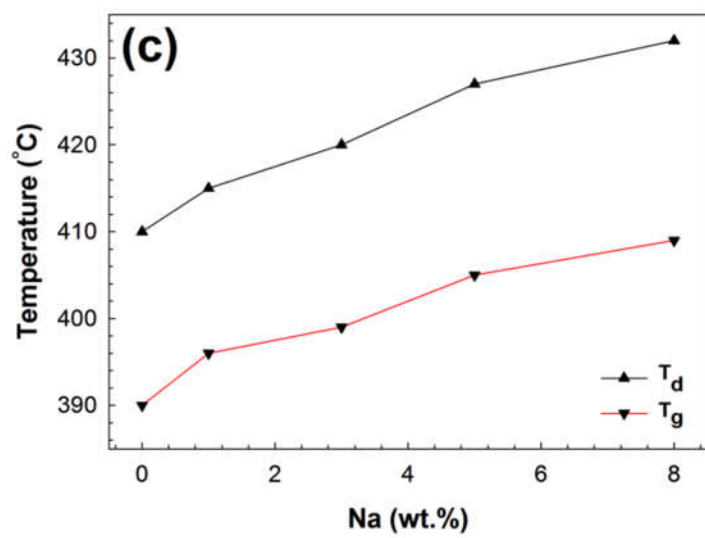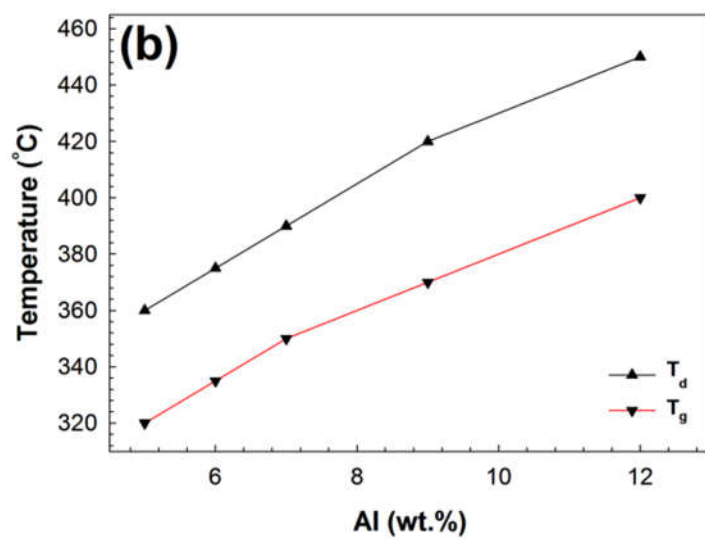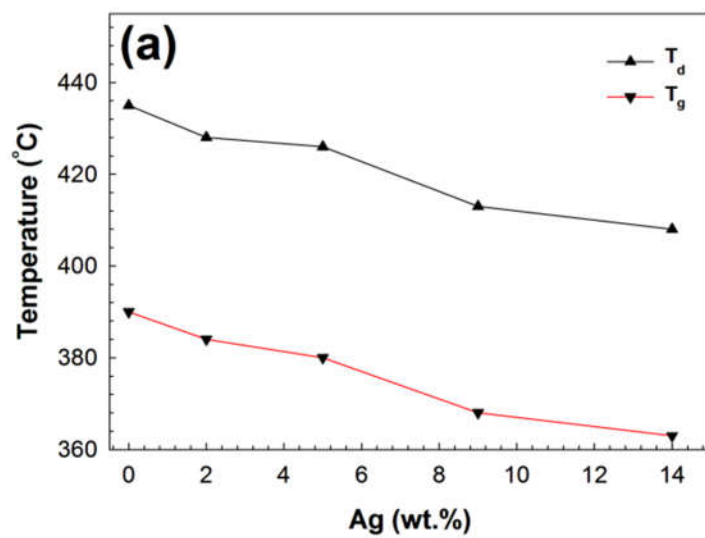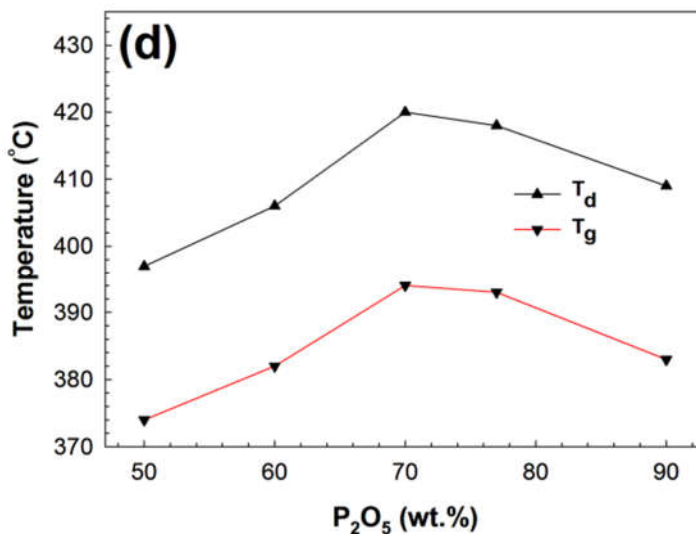
Figure 5.6: Decomposition temperature (T$_d$) and transition temperature (T$_g$) of RPLGD with different concentration of (a) silver, (b) aluminium, (c) sodium and (d) phosphorus pentoxide.

The T$_g$ and T$_d$ peaks for the different chemical composition especially Ag, Al, Na and P$_2$O$_5$ element, which are related to thermos change in the glassy system of RPLGD were obtained at heating rate of b=10°C.min^{-1} are shown in Figure 5.6. Herein, the composition of the T$_g$ is situated between 320 °C and 410 °C and the T$_d$ is in the range from 360 °C to 445 °C with the average T$_g$ value is 339.4 °C and T$_d$ is 381.5 °C. The data applied are milestones for glass annealing procedures as well the crystallization stability of the glasses. Figure 5.6(a) shows that increasing Ag resulted in the lower T$_g$ and T$_d$, indicating that the excess Ag weakens the glass network structure and becomes more rigid [141]. On the contrary, increasing Al content raised T$_g$ and T$_d$ in Figure 5.6(b), suggesting that Al content strengthens the glass network structure by enhancing water tolerance [10]. Similarly, T$_g$ and T$_d$ values also increase with increasing Na content in the glass matrix due to its functioning for mobility of activator ions and forming a sub-major structure by substituting P-O-P by P-O-Naas shown in Figure 5.6(c) [10]. Besides, Figure 5.6(d) demonstrated that 70wt.% of P$_2$O$_5$ content had the highest temperatures of T$_g$ and T$_d$. When P$_2$O$_5$ content was higher than 70wt.%, the T$_g$ and T$_d$ were decreased indicating that the former structure is more cross-linked, which is has greater PO$_4$ content [10].These evolutions can be explained by lacking Na or H$_3$BO$_3$ as a network modifier in the glass system.

5.3.2   Structural studies of phosphate glasses

To understand the observed variation in thermo-physical properties and $E_{optical}$ values, structural studies were carried out using X-ray diffractometer and Fourier-transform infrared spectroscopy.

X-ray diffraction analysis

In this section, clear, transparent and bubble-free glasses were used for all the investigated compositions. Figure 5.7(a) shows XRD pattern observed for A-series pattern of the RPLGDs. It showed a scattering peak at 25° which is due to P-O-P network, characteristic of the amorphous nature of the RPLGDs, similarly with XRD patterns obtained from Abd. Rahman's group [139]. 200 Gy was chosen as dose control because it shows optimum dose for RPL intensity. Thus 200 Gy is suitable to differentiate between glass before and after irradiation.
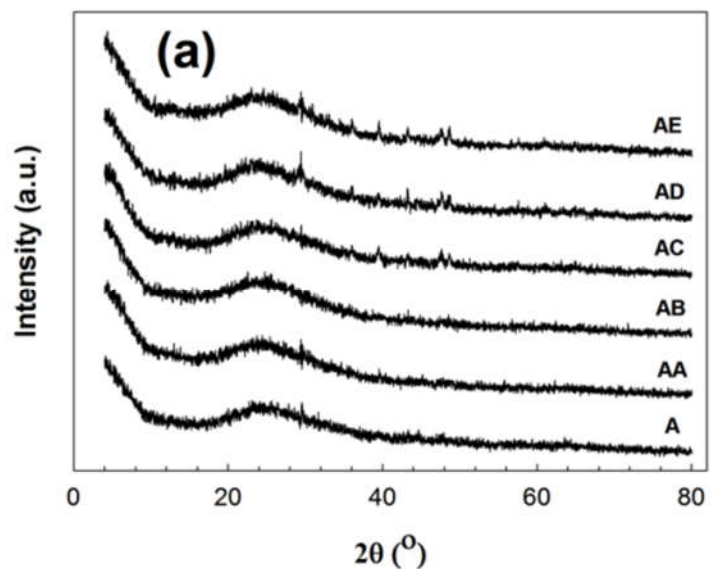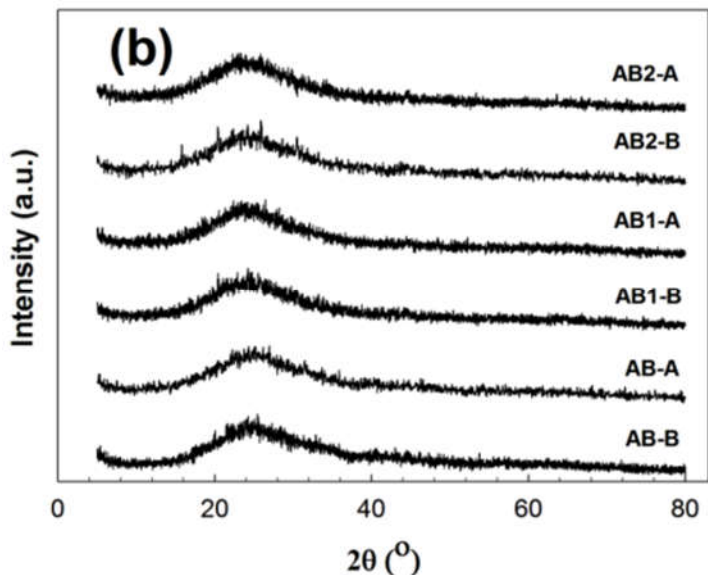
Figure 5.7: X-ray diffraction patterns of the (a) A-series and (b) AB-series glasses with before (-B) and after (-A) 200 Gy of γ-irradiation.

Several small sharp peaks were observed in the both pattern caused by detector noise forms during the detection and readout process. Apart from that, as the silver content was increased, no significant change was exhibited in the XRD profiles of all samples with differing loading of silver contents (2.0-7.0 wt.%) before γ-irradiation as shown in Figure 5.7(a). AB-series was chosen for extra measurement because only AB sample in A-series was fluoresced after γ-irradiation. Therefore, AB-series were subject to be further examination. Figure 5.7(b) also shows no significant change are exhibited in the XRD profiles of the AB-series samples before and after 200 Gy γ-irradiation indicating no phase change in the glass matrix after irradiation treatment.

Fourier-transform infrared spectroscopy

Vibrations of bonds and groups spectra of A-series and AB glasses powder (before & after 200 Gy γ- irradiation) are shown in Figure 5.8.
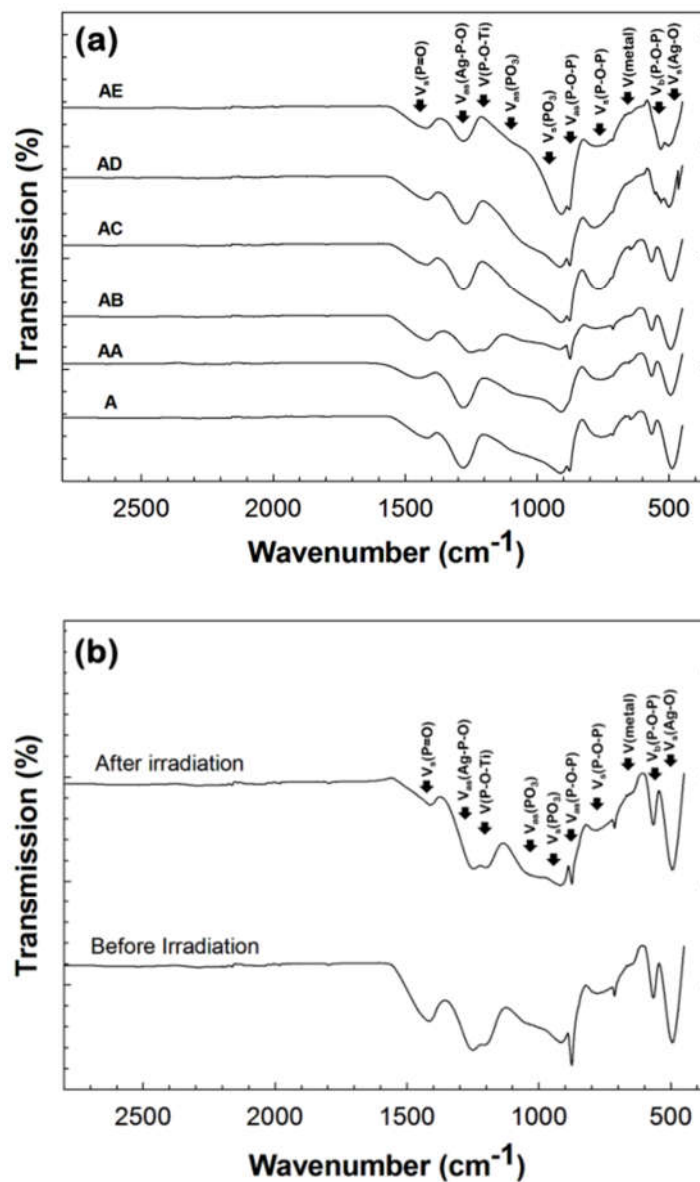
Figure 5.8: FTIR spectra of (a) A-series and (b) AB sample before and after γ-irradiation.

The IR vibrations are mainly active in the mid-region of the infrared spectrum in the range of 1500-400 cm^{-1} due to characteristic bands of phosphate glass as shown in Figure 5.8(a). There is no significant difference in the line shapes of the spectra, because all glass samples contain higher than 50 wt.% of P_2O_5, which is as expected. We noted that the band observed at 1425 cm^{-1} is due to the characteristic stretching mode of the P=O bond. Next, the band at about 1281 cm^{-1} is assigned to the asymmetrical stretching vibration of O-P-O and P=O groups, v_{as}(O-P-

O)/v_{as}(P=O) (equivalent to Q_2 structural units), while the medium broad band at 1100 cm^{-1} is related to the symmetric stretching vibration of that group, v_s(O-P-O) [142]. For the AB glass sample with 12 wt.% TiO_2, the IR patterns essentially remain the same except the intensity of bands around 1200 and 1280 cm^{-1}. A reduction and increases in the intensity of the band indicate that as TiO_2 content increases, the phosphate network depolymerizes with the conversion of PO_2 groups (Q_2 structural units) into PO_3 groups (Q_1 structural units).

Despite of Q_2 to Q_1 conversion occurs by breaking of P-O-P linkages, the formation of P-O-Ti (along with P-O-Al) bonds provide cross linking between 'P' structural units, correspond to the symmetric and asymmetric vibrations of PO_2^- in Q_2 units with Ti around 1200-1300 cm^{-1}, which make the glass network more rigid [143]. The non-bridging oxygens of P=O bonds may be converted into bridging oxygens upon formation of P-O-Al bonds and the links O-Al-O replace O-P-O as aluminium enters the network [144]. Next, the 1100 cm^{-1} band is the dominant feature of the spectra and has been assigned to P-O- units and easily interacts with metal such as Ag to form P-O-Ag band. The asymmetric stretching of the metaphosphate group, v_{as}(PO_3) was observed in the range of 1012-1153 cm^{-1}. This indicates that the bands due to v_{as}(PO_3) can intervene with the band at 1100 cm^{-1} (chain end group equivalent to Q1 structural units). Additionally, the broadening observed in the region of 900-1105 cm^{-1} may be due to the interference of v_s(PO_3) with the spectral range 1000-1060 cm^{-1}. The shoulder around 878 cm^{-1} is assigned to the asymmetric stretching vibration of P-O-P linkages, v_{as}(P-O-P), while the relatively weak band around 764 cm^{-1} is due to the symmetric stretching vibration of that linkage, v_s(P-O-P) [144-145]. The region below 600 cm^{-1} is usually assigned to the vibration of metals [146]. Hence, the broad band at about 525-539 cm^{-1} may be assigned to the harmonics of P-O-P bending vibration as well as to the deformation mode of PO- group and the last band at 480 and 510 cm^{-1} corresponds to the stretching and Ag-O symmetrical vibrations in PO_4. Piao and group (2000) describes that production of electron-hole pairs during irradiation provides another path for bond rearrangement, reducing the constraints on structural relaxation [147]. The relaxation process releases some of the excess energy stored in the structure, resulting in change in the bond angle. Apart from that, a comparison of spectrum in Figure 5.8(b) shows that the samples before

and after γ-irradiation shows nearly similar IR transmission spectra but different in term of intensity. There is changes in the intensity peaks in the 800-1017 and 1425 cm^{-1} range dominated by P-O-P and P=O linkages, indicates the breaking of these linkages will produces more non-bridging oxygen [148].

5.3.3 Optical properties

The optical characterization such as optical absorption, transmission and luminescence measurements of each glass samples were carried out using UV-Vis spectroscopy and photoluminescence spectroscopy.

UV-Vis spectroscopy

Figure 5.9 shows the transmittance and penetration capability of phosphate glass in the UV-Vis regions with different wt.% of $NaNO_3$, Ag, $Al(OH)_3$ and (d) P_2O_5.
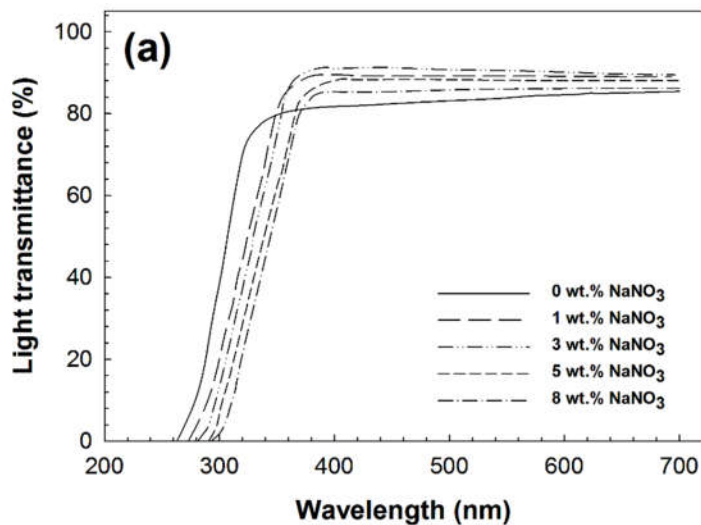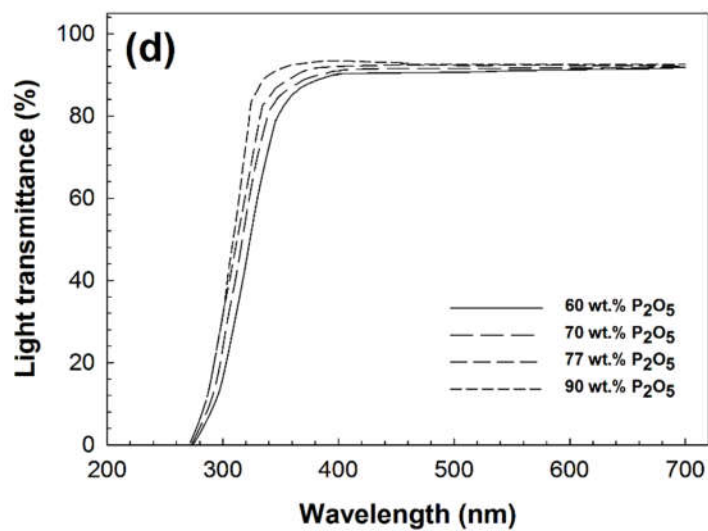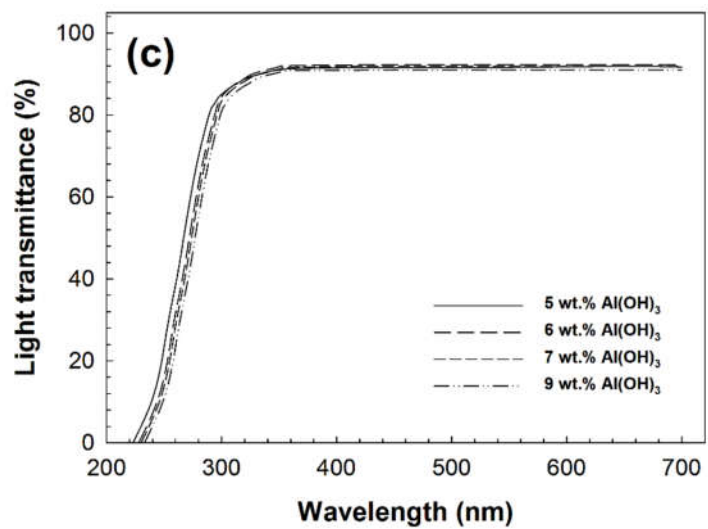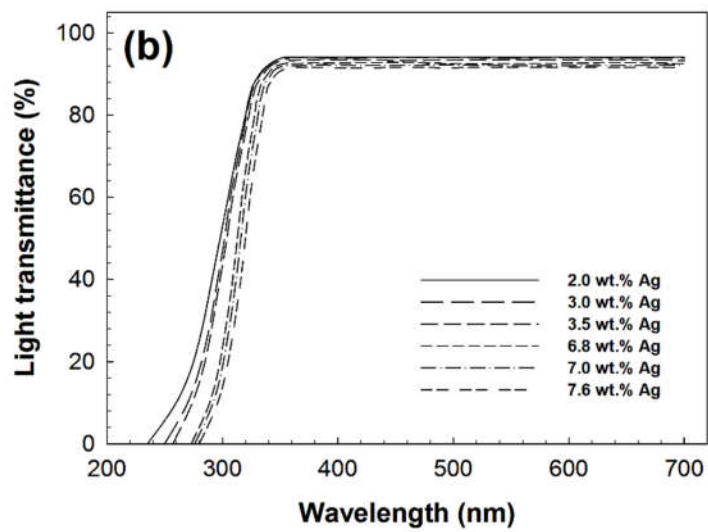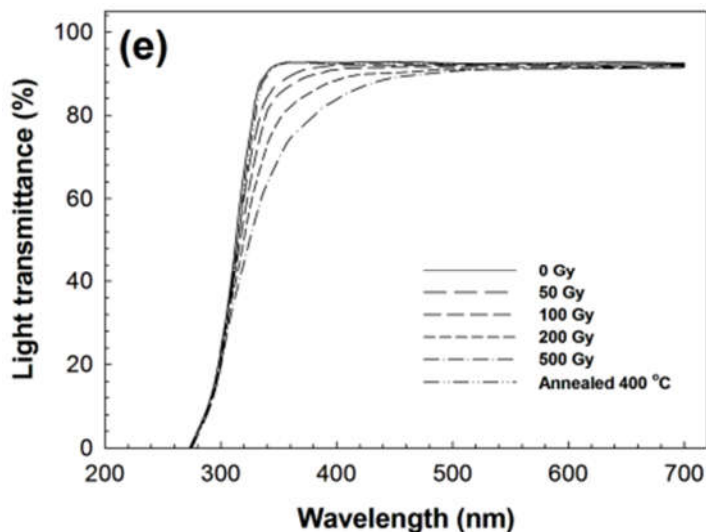
Figure 5.9: Penetration spectrum of glass system with different wt.% of (a) NaNO₃, (b) Ag metal compound, (c) Al(OH)₃ and (d) P₂O₅. (e) The irradiated dosage of 3.5 wt.% Ag glasses (control) was from 0 to 500 Gy.

Figure 5.9(a) shows that excess Na compound decrease the penetration capability of UV light. However, Na is important for mobility of activator ions in glass matrix. Thus, the optimum wt.% of Na was important in making a good RPLGD with high penetration rate, as well as colour centre forming in the glass matrix. Therefore, the curve with 3.0 wt.% of $NaNO_3$ was chosen as the best result due to the highest light transmittance of the glass system. Besides, figure 5.9(b) shows the light transmittances were decreasing with increasing wt.% of Ag. Hence, higher concentration of Ag results in weaker penetration ability for ultraviolet spectrum [16]. Therefore, glass sample with 3.5 wt.% shows the best penetration ability of all glass with Ag samples. Similarly, excess Al compound also decreased the penetration capability of UV light as shown in figure 5.9(c) using Beer-Lambert Law. In addition, the observed variation in the penetration rate values can be explained based on the conversion of bridging oxygen (BO) to non-bridging oxygen (NBO) atoms brought about by the Al_2O_3 incorporation in the glass. Hence, for glasses containing low wt.% of Al(OH)₃ where the relative concentration of NBO atoms are high, their penetration rate values are higher, when compared to the glass with high wt.% of Al(OH)₃. Above all, it can be inferred that at higher concentration of Al(OH)₃, Al^{3+} mainly goes to the network to form BO rather than further modifying the network and increasing the concentration of NBO atoms.

Additionally, the penetration capability of UV light was enhanced after the wt.% of P_2O_5 were increased due to higher NBO content in the glass system as shown in Figure5.9(d). However, different penetration curve was observed in the pattern with different irradiated dose in the same chemical compounds due to formation of neutral Ag atoms within the forbidden band of glass matrix during ionising radiation exposure, as shown in Figure 5.9 (e). Also, it is evident that RPLGDs which have the best transmittance have the highest RPL sensitivity because good transmittance ability of glass will produce more colour centre form within the glass.
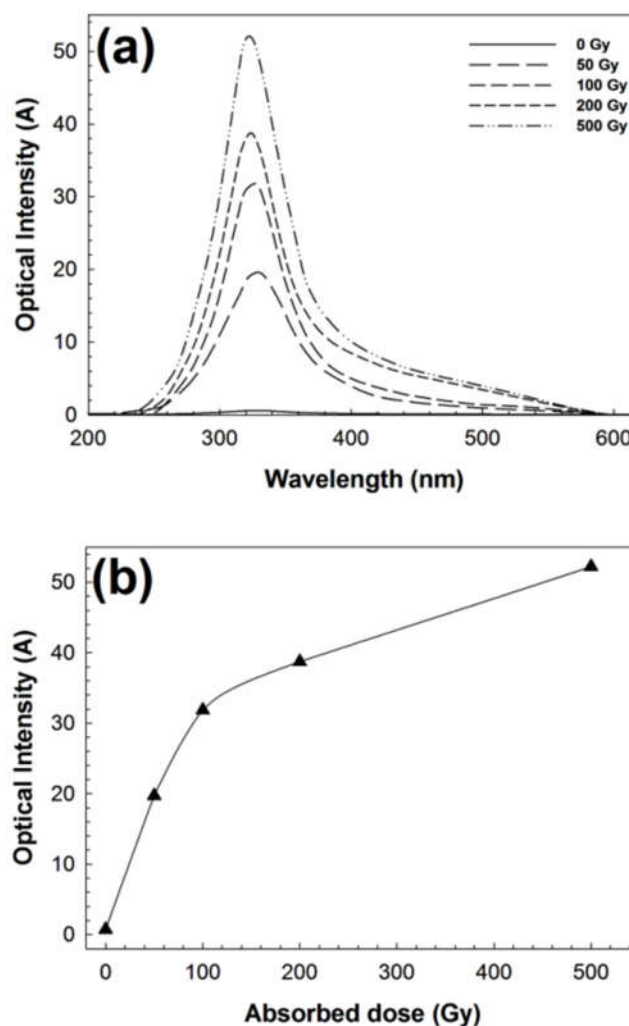
Figure 5.10: Absorption spectra of RPLGD with 3.5 wt.% of Ag concentrations irradiated with the different doses from 50 to 500 Gy by Co-60 source and 0 Gy used as a control sample.

Figure 5.10 shows the absorption spectra of RPLGD with 3.5wt.% of Ag activator concentration with different irradiation doses from 50 to 500 Gy. All the absorption curves are characterized by a broad onset of absorption edge over the region of 200-600 nm as shown in figure 5.10(a). Different irradiation doses affected the absorption spectrum of the irradiated glass. The intensity peak of absorption spectra was increased when irradiation dose increased indicating the formation of significant amount of luminescence centres within the glass network, therefore increasing the absorption intensity peaks as shown in figure 5.10(b). However, the wavelength of absorption spectra peak has not changed for the same synthesised compounds. Thus, the amounts of luminescence centres depend on radiation dosages and optical intensity was directly proportional to the radiation dose absorbed by the RPLGD.

Photoluminescences Spectroscopy

To demonstrate the favourable PL activity induced by the fading effect of the AB-series samples because from the A-series samples, only AB sample was fluoresced under UV light irradiation. The PL intensity of AB-series was compared with fresh prepared glass and recycled glass with the same conditions.
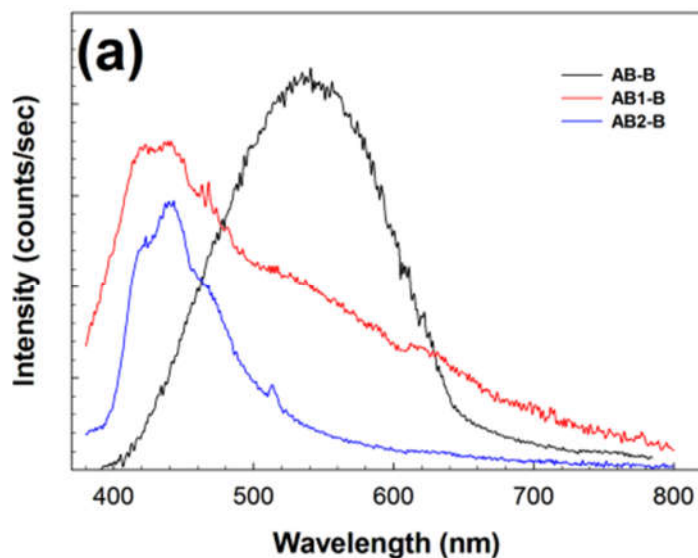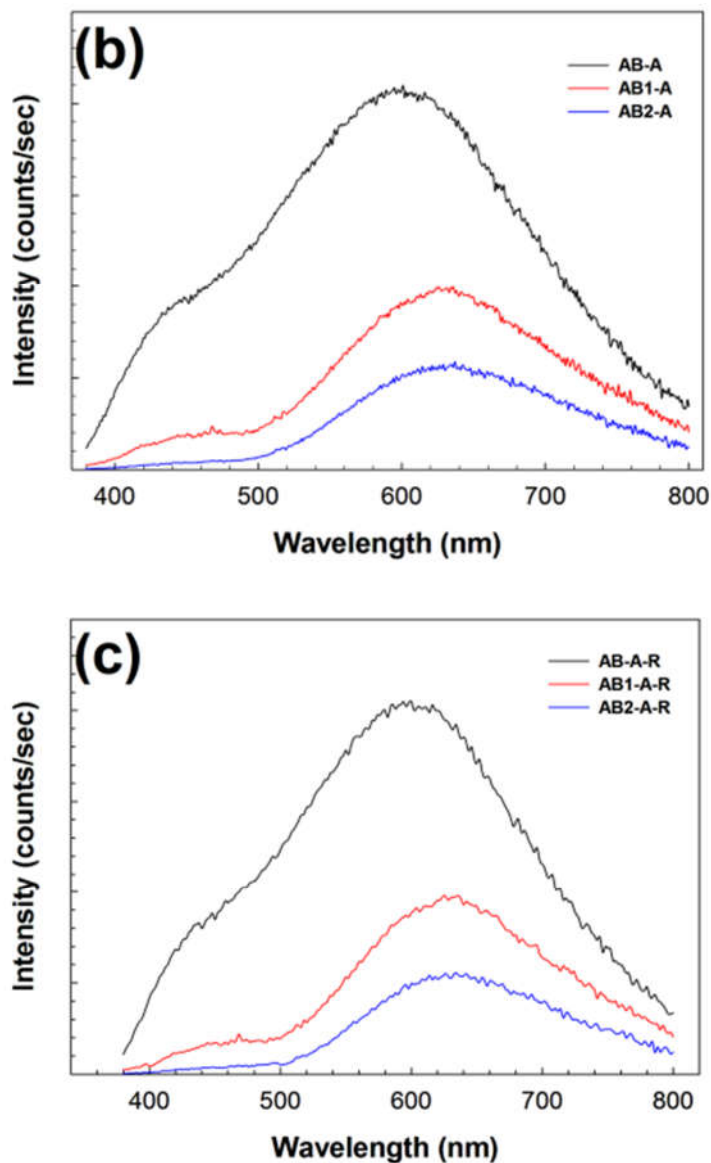
Figure 5.11: Emission spectrum of AB-series RPLGD: (a) before (-B), (b) after (-A) 200 Gy of γ-irradiation and (c) Recycled of AB-series (-R) samples with same dose irradiation. The samples were excited at 325 nm.

Before irradiation, the AB2-B sample with 0 wt.% TiO_2 shows a broad peak centred at 435 nm with significant tailing towards higher wavelength region attributed to the different types of colour centres present in the glass as shown in figure 5.11(a). It is reported that in binary phosphate glasses, linkages form and act as localized levels in the optical gap of the glasses and can trap the electrons known as colour centres [149-150]. In a multi-component glass, there can be a variety of colour

centres, depending upon chemical concentration in the glass where a broad emission spectrum is observed. With incorporation of TiO_2 at the expense of P_2O_5 up to 5% (AB1-B), the wavelength corresponding to the emission maximum remained the same, even though there is a slight change in the line shape. However, above 5% of TiO_2 at the expense of P_2O_5 (AB-B) incorporation in the glass, the emission maximum shows significantly shifted to higher wavelength at 528 nm indicating a decrease in the energy corresponding to localized levels. The changes are with respect to the creation of more NBO atoms and formation of relatively more ionic P-O-Ti linkages at the expense of more covalent P-O-P linkages. At this stage, it is worthwhile to mention that no Ti^{3+} emission is observed from the AB-B sample as reported by Bausa [151] and Batyaev [152].

Apart from that, Figure 5.11(b) shows the PL spectra of the AB-series samples excited at 325 nm after γ-irradiation with an absorbed dose of 200 Gy. After irradiation treatment, all AB-series samples have radio-photoluminescence signals. The RPL spectra were measured to investigate the emission of silver ions corresponding to the dipolar electric transition $4d^{10} \leftrightarrow 4d^9 5s^1$ [66]. According to a research performed by Dmitryuk (1996), spectral range of radiophotoluminescence of silver glass was 600-800 nm, which was not dependent on glass material [153]. Moreover, the relative intensity of the band at 435 nm appears was indicating that different nature of colour centres is most likely occurring within the glass before γ-irradiation treatment [154]. The existence of this emission band can be related to the formation of significant amount of Ag° centres within the glass network. Even if the formation mechanisms of hole and electron traps are different, in all the irradiated cases, the 435 and 620 nm peak observed in the emission spectrum is believed to be due to aggregation of Ag° and Ag^+ ions which have possibly generated additional chemically stable clusters Ag_m^{x+} such as Ag^{2+}, Ag_3^{2+} [153]. Besides, there is only slight decrease of luminescence intensity to 98% (AB-A-R), 99% (AB1-A-R) and 98% (AB2-A-R) for recycled AB-series of RPLGD compared to the original series of RPLGD from luminescence maxima intensity with the same irradiation dose as shown in figure5.11(c)). The tiny loss of the luminescence efficiency indicates the excellent radiation glass reusability of RPLGD.
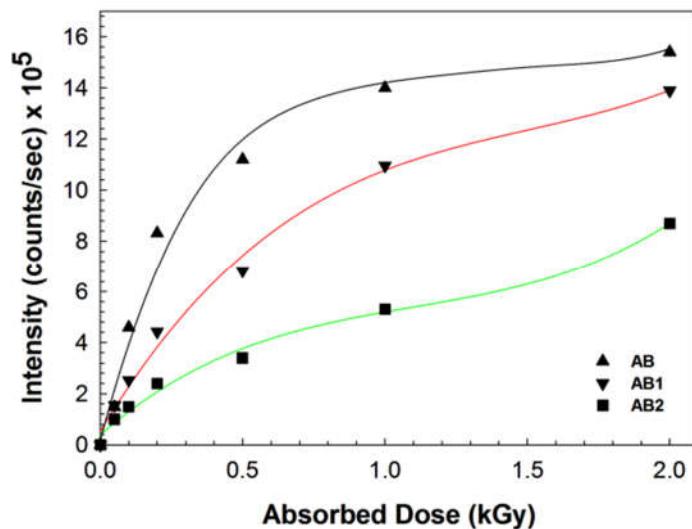
Figure 5.12: **Effects of absorbed doses on the RPL-intensity at 620 nm of (▲) AB, (▼) AB1 and (■) AB2 powder at varying absorbed doses.**

In order to determine the dosimetry sensitivity of RPLGD toward irradiation dose, the glass samples were irradiated with γ-irradiation at varying doses from 0.05 to 2.0 kGy, respectively. The dose range was chosen to estimate the effect of doses in full range. The data were re-plotted in maximum PL-intensity versus absorbed doses as shown in Figure5.12 in order to elucidate the PL-intensity and reaction rates. The intensity peaks were increasing proportionally with absorbed dose due to the colour centres forming within the glass [154]. All the PL-intensity highest peaks are almost approaching saturation function with precisely R-squared values of 0.979, 0.989 and 0.986 for AB, AB1 and AB2 samples, respectively. In accordance to the AB-series samples, the first-rate constant gave the value of 11.34 (AB), while this value decreased to 3.66 (AB1) and 3.11 (AB2) at same absorbed dose by calculating the slope of the graph. The highest rate constant of this sample is technically better by applying the optimum chemical composition, which renders higher colour centres forming after γ-irradiation and thus greatly enhances the PL-intensity peak. However, the rate constant of AB-sample may be attributed to existence of multiple emission band including Ag° centres [149-150]. Besides, with high concentration of Al(OH)$_3$ in AB2 sample, the rate constant gave a lowest value because no charge transfer phenomena take place in these glasses as Al^{3+} mainly goes to the network to form BO rather than further modifying the network and increasing the concentration of NBO atoms. As a result, it obstructed the transmittance of γ-irradiation and

slowing the build-up process of colour centres within the glasses. Therefore, there is an optimum amount of chemical composition (AB1) on RPLGD would give best impact on the reaction rate.

5.4 Conclusion

In summary, the glass made by the wet melting method had better chemical compounds distribution. Based on thermo-physical and structural studies, the hardness test shows that the HRA values increased with increasing Al content. Additionally, variation in T_g, T_d and density values for these glasses are in accordance with the structural changes taking place in the glass as a function of composition. In fact, it was established that the glasses possess good optical transmittance (above 80%) for the region above 350 nm. Moreover, we found out that the irradiated glass wavelength of absorption spectra maxima typically occurs in the range of 300-350 nm. Radiation dosage did not affect the peak position of absorption spectra; however, it could affect the optical intensity in the same compounds. Furthermore, different synthesised compounds could also affect the radiation sensitivity. RPLGD series have the highest sensitivity between 2.0 to 4.0 wt.% of silver. Hence, RPLGD series of AB-sample have the highest sensitivity with 4.0 wt.% of silver content. Therefore, the RPL spectra of the AB-series glasses were further investigated with application of silver nanoparticles in this study. RPL emission peaked at 620 nm due to orange RPL at connected to the 325 nm bands of the excitation spectrum. These bands were attributed to the Ag° and Ag^{2+} centres, respectively. Lastly, IR spectra of all sample glasses have been studied and provides information about the main characteristics frequencies for phosphate bonds present in the glass network such as P=O, P-O-P and O-P-O. It also confirms that the addition of TiO_2 in the glass results in the progressive conversion of Q2 structural units into Q1 (up to 10 wt.%) and Q0 structural units (more than 10 wt.%). Cross-linking provided by P-O-Ti and P-O-Al bonds between shortened discrete 'P' structural units (for $x \leq 10$ wt.%) results into a stronger and rigid glass network.

Chapter 6

6.   Studies on the Effect of Silver Particle Size on Radio-Photoluminescence Glass Dosimeters

6.1   Introduction

Radiophotoluminescence glass dosimeter (RPLGD) is an integrating type solid state dosimeter and used to be a prospective tool intended for dosimetry control and have long been examined for applications in personal solid-state dosimetry and radiation measurements [65]. They possess linear dose sensitivity in a wide gamma and X-ray spectral region. For that reason, phosphate based glass was chosen due to its ability to accommodate large concentrations of active ions without losing their useful properties of the material [66]. Therefore, silver metal which is activator content in the glasses gives important effect on the build-up performance. Generally, increasing silver content will accelerate the build-up, while a decreasing silver content will retard build-up. However, lower silver content may be required to reduce the effective order of magnitude. Apart of using heat treatment to increase build-up, using silver seed at nanometer scale is also one of the possible solutions due to localized surface plasmon resonance (LSPR) of free electrons and can be tuned by using different particles size, resolving the build-up effect [18].

After colour centres are completely formed, the orange fluorescence (620 nm) emitted by the RPL glass is viewed during UV light excitation. The fluorescent radiation, thus emitted is proportional to the ionizing radiation which has been received, and is measured vertically to the direction of the UV-radiation incidence. The dose rate can be measured many times from the irradiated RPLGDs as the colour centres never disappear after reading out the accumulated data by UV light again and again. However, resetting of the RPL signal can be done by a suitable heat treatment, normally around transition temperatures of phosphate glasses. Thus, this product gives some excellent features such as repeatable measurement [18].

Improving dosimetric sensitivity and quality of glass by improving the design of base composition and using different silver sizes as activator in phosphate oxide glass was the main objective in this chapter study. Therefore, phosphate glass dosimeters were prepared from reagent powders of P_2O_5, Li_2CO_3, $Al(OH)_3$, $NaNO_3$ TiO_2 and H_3BO_3 with different sizes of silver metals using wet melting method. The dosimeter glasses generally contain large proportions of lithium compound. The lithium proportion ensures a low effective order of magnitude while at the same time giving a low natural luminescence or initial dose to the dosimeter. However, excess in lithium portion gives alternating effect of glasses with thermal neutrons; such the phosphate glass is inherently sensitive to thermal neutrons. Thus, optimum ratio of lithium content is required for the best physical and optical properties efficiency. Apart from that, the use of aluminium hydroxide will improve the surface chemical resistance. The optical and physical properties of RPLGDs were determined after different silver contents were incorporated within the phosphate glass. In addition, the density of the phosphate glass system was determined. The photoluminescence properties of Ag-doped phosphate glass with evaluation of the excitation and emission properties of RPLPGDs and related RPL mechanisms are also discussed.

6.2 Experimental

6.2.1 Synthesis of silver nanoparticles

Before synthesizing the Ag-doped phosphate glass, silver nanoparticles (AgNPs) was firstly prepared following the procedure as described in section 3.3 of Chapter 3. Briefly, aqueous mixtures of $AgNO_3$ (0.375 mM, 180 mL), $Na_3C_6H_5O_7$, Na_3CA (12.5 mM, 72 mL) and H_2O_2 (50 mM, 180 mL) were prepared. The bulk sample was divided into two parts and KBr solutions (1 mM, 50 & 100 μL) was added to each solution to make different sizes of AgNPs as KBr control the nucleation and particles growth process, respectively [117]. Potassium bromide limits the growth of the silver. Subsequently, $NaBH_4$ (5 mM, 25-30 mL) was injected to each mixed solution and the reaction was initiated. The different colour of AgNPs solution confirms the formation of silver nanoparticles with different sizes [105]. The sample was then centrifuged and washed with excess deionized water to remove impurities and then dried overnight at 60 °C in the oven.

6.2.2 Synthesis of radio-photoluminescence glass dosimeters

Here, all phosphate glass dosimeter series were prepared from reagent grade powders of anhydrous P_2O_5 (73 wt.%), Li_2CO_3 (5 wt.%), $Al(OH)_3$ (6 wt.%), $NaNO_3$ (2 wt.%), TiO_2 (8.5 wt.%), H_3BO_3 (1.5 wt.%) and was set as BASE for ratio measurement with AgNPs (various wt.%) at different sizes, following the weight ratio of sample AB as described in Chapter 5. Phosphate glasses of an appropriate composition as given in Table 6.1 were synthesized using wet melting method.

Table 6.1: Chemical composition for making radiophotoluminescent glass dosimeter

No	Chemical content	Nominal composition range (wt.%) & label									
		Ag (Bulk)				AgNPs (40 nm)			AgNPs (90 nm)		
		A0	A1	A2	A3	B1	B2	B3	C1	C2	C3
1	BASE	100	97.5	95.7	92.3	97.5	95.7	92.3	97.5	95.7	92.3
2	Ag	0	2.5	4.3	7.7	2.5	4.3	7.7	2.5	4.3	7.7

Systematically, each glass dosimeters contain different weight composition of Na, P, O, Al, Li, Ti and Ag, weighed using a digital weighing instrument with an accuracy of ±0.01 g. The batch powders were mixed with DI water and the mixed liquid batch was preheated at 120 ºC for 24 h in an alumina crucible to evaporate water as described in methodology in Chapter 3. After that, the liquid batch was melted in electrical heated furnace in atmosphere at a heating rate of about 10 ºC.min^{-1}, the temperature was gradually increased up to 600 ºC and kept at this temperature for 5 h. Once the mixture was liquidized, the temperature was then increased again to 1250 ºC and left for one hour to obtain the appropriate viscosity. After the refining process, the glass liquid was then poured onto a preheated graphite plate. At this point it then takes 12 h to complete the annealing process at 400 ºC to avoid internal mechanical stresses developed during solidification process.

6.2.3 Radio-photoluminescence dosimeter application

For dosimetric measurement, the samples were irradiated with γ-radiation, delivered at 1.37 kGy/h (24/08/2017) using Gamma-cell (Gamma-excell-220, UKM) using a Co-60 source. In this work, the samples were irradiated such that the

absorbed dose was at 100 Gy. The glass samples were kept in a desiccator to prevent possible occurrence by moisture before further characterization.

6.2.4   Density

The densities of the glasses (A0, A1, A2, A3, B1, B2, B3, C1, C2 and C3) were measured at room temperature using the Archimedes principle, and distilled water was used as the immersion liquid with an accuracy of ± 0.03 g/cm^3. Molar volume of the glass was also obtained from the density. Density of glasses was measured to understand the effect of transmittance with density and molar volume of base component, which is affecting the sensitivity of the RPLGD.

6.2.5   Transmission electron microscopy

The morphology and dimension of silver nanoparticles with different sizes (40 nm & 90 nm) were inspected by transmission electron microscopy (TEM), 200kV Tecnai G2 20 S-Twin, FEI model. AgNPs solution was sonicated for 10 min in ultrasonic bath before dropping on the copper grid. After aqueous AgNPs was drop on copper grid, it was dried at room temperature before viewing process. Size dimension analysis was done using SigmaScan pro – systat software.

6.2.6   X-ray diffractometer

The structure of the phosphate glass samples were investigated using X-ray diffraction (Advance-8 Bruker X-ray diffractometer). AgNPs with 40 nm and 90 nm sizes were measured for control, then glass samples before and after 100 Gy of γ-irradiation were characterized for comparison. Each sample was made into a fine powder before diffraction analysis process. After that, 2g of sample's powder was deposited on the sample holder and the diffraction peaks analysis was carried out.

6.2.7   Fourier-transform infrared spectroscopy

FTIR technique was used to identify the chemical compound such as chemical bonds in a glass substance by creating an infrared absorption spectrum of a phosphate glass by collecting high spectral resolution data recorded over the frequency range 400-4000 cm^{-1} with a resolution of ~ 4 cm^{-1} as detailed in Chapter 3using Fourier transform infrared spectroscopy (Perkin Elmer/Lamda-950). In brief, every wt.% of samples before and after 100 Gy γ-irradiation were used for analysis.

The glass powder was placed on the KBr cell and then pressed in a mechanical press to form a thin and transparent pellet, which the beam of the spectrometer can pass through.

6.2.8   Photoluminescent spectroscopy

Excitation and emission measurements were performed at room temperature and RPL intensity was measured using FLS-920 spectrophotometer (excitation: 260 & 320 nm). The RPL emitted from sample was observed in a direction perpendicular to that of the excitation beam and analysed using suitable filters with central wavelengths of 460 and 620 nm, respectively. Samples were irradiated with 100 Gy and excited 325 nm for RPL measurement. Then, AgNPs (90 nm) samples were used for further analysis as it shown the best RPL intensity comparing to others. It was set 50 Gy to 2 kGy for dose kinetic study. All luminescence measurements were carried out at room temperature. The glass samples in the form of disc and powder were used in this analysis. Powder glass samples were put on the slide holder while disc samples were stick in the sample chamber of the instrument. Emission spectra were recorded with a resolution of 5 nm and all emission spectra were corrected for the detector response.

6.3   Results and discussion

The RPL emission images as a function of 100 Gy γ-ray absorbed doses when the γ-irradiated Ag-series phosphate glass is excited using UV light, are shown in figure 6.1, where it shows the intensity of orange colour emission in human eye during UV light exposure.
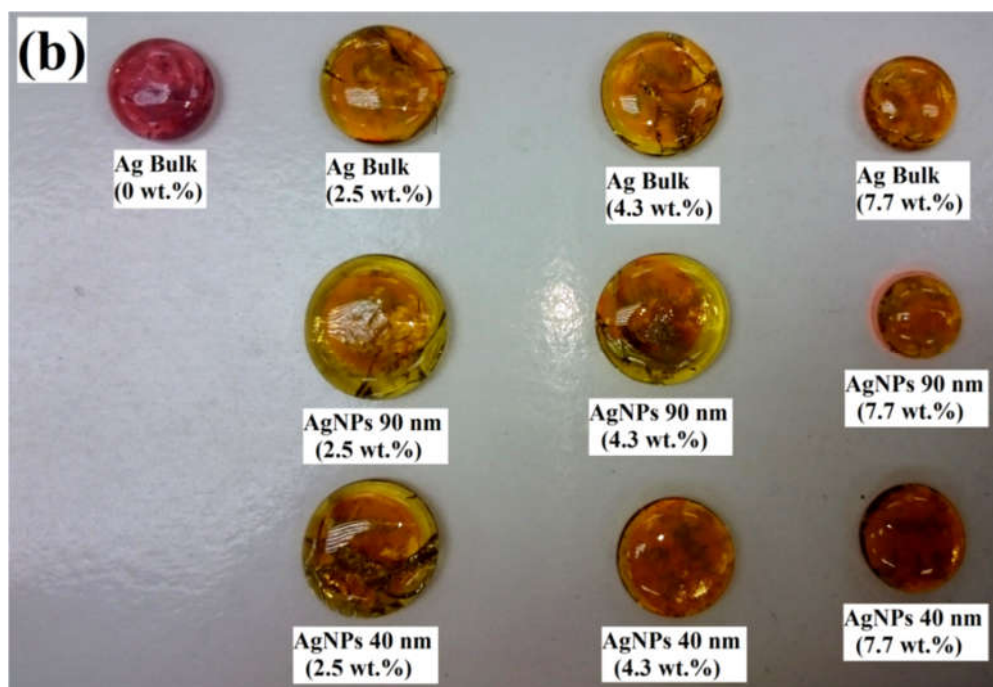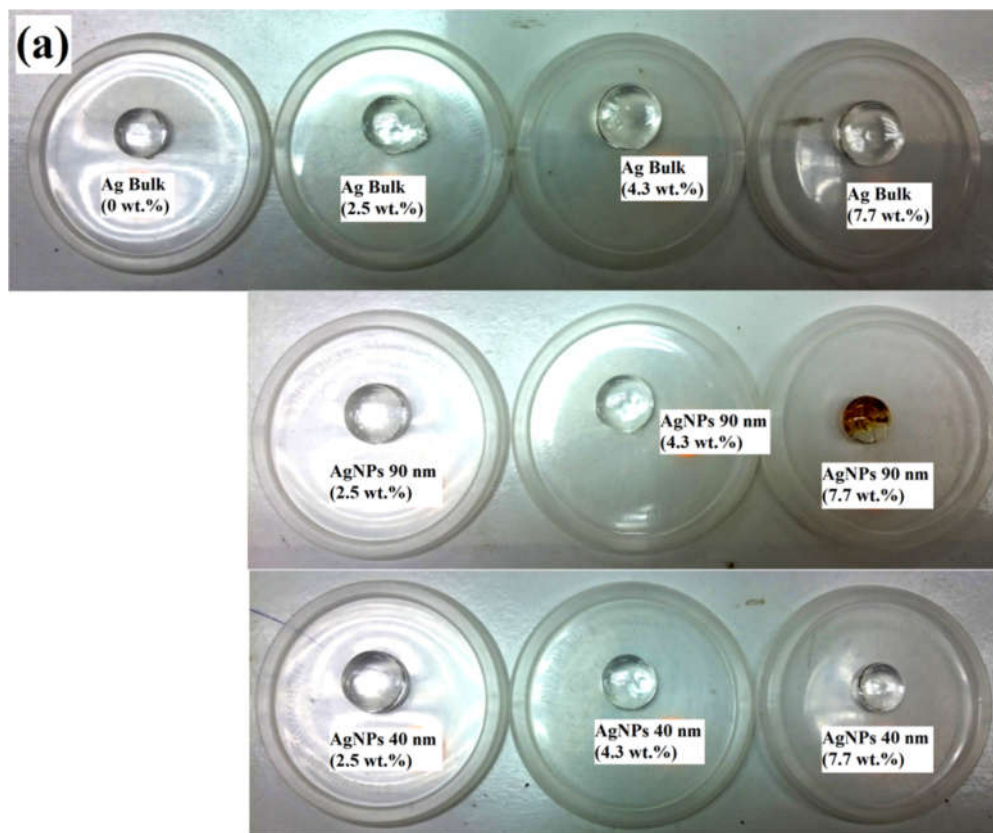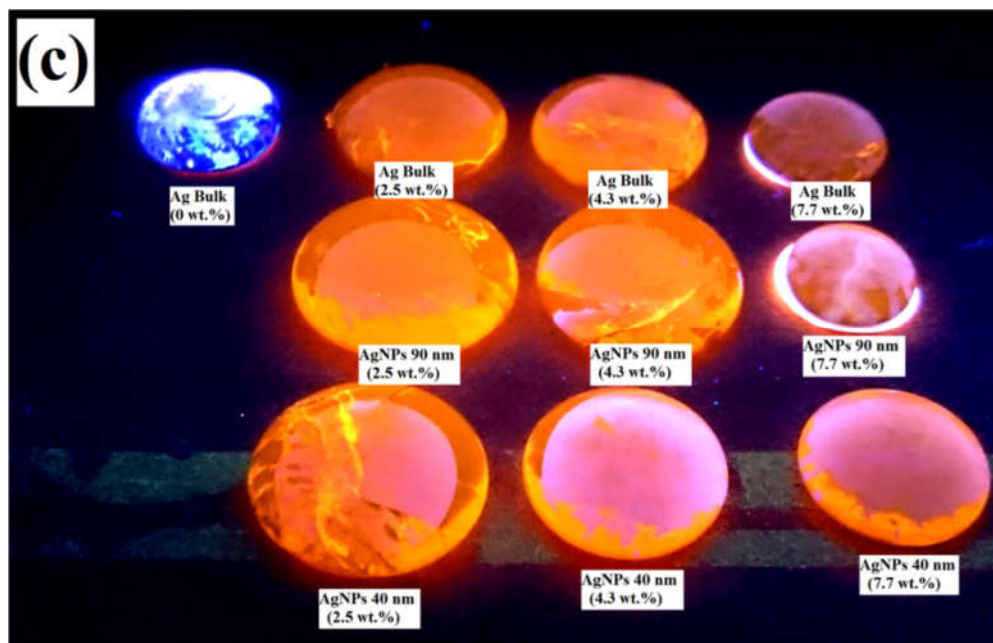
Figure 6.1: Photograph of Ag-series of glass samples; (a) before γ-irradiation, (b) after γ-irradiation and (c) RPL emission under UV light excitation.

Figure 6.1 show the images of Ag-series of phosphate glass samples. Figure 6.1(a) shows clear images of all samples before γ-irradiation treatment, where Fig. 6.1(b) shows brown images of all samples after γ-irradiation and Fig. 6.1(c) shows a RPL emission of phosphate glass under UV light excitation. The colour of the glasses turns to brown after γ-radiation treatment is due to the formation of colour centres in which electron-hole pairs is produced and will be trapped within forbidden energy level within the phosphate glass system [18]. After colour centres completely formed, the orange fluorescence is emitted during UV light excitation and the fluorescent radiation intensity emitted is proportional to the ionizing radiation which has been received [18].

6.3.1 Density

Density measurements of Ag-series RPLGDs samples as a function of Ag weight fraction (wt.%) were measured using Archimedes principle are shown in figure 6.2.
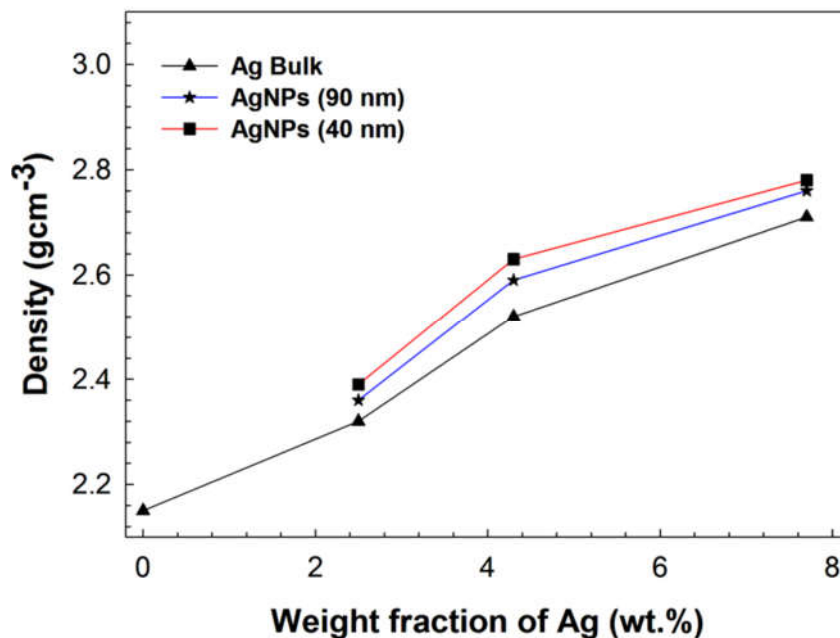
Figure 6.2: Variation of density of Ag-series RPLGDs as a function of Ag weight fraction (wt.%).

Figure 6.2 shows the glass density values of Ag-series samples are slightly shifted from 2.15 to 2.78 g.cm^{-3} and increases proportionally to the silver content in the glass as other compositions were control. The densities result seems to be different with previous measurement in A-series (Chapter 5) because of different base composition. With a high amount of Ag (7.7 wt.%) in the vitreous network, the density increases up to 2.71, 2.76 and 2.78 g.cm^{-3} for A3, B3 and C3 samples, possessing higher density values in this study. Despite, the packing density of a glass system is found to increase if the particle size distribution is extended, means increasing the mean-size ratios resulting in greater packing densities. Thus, decreasing the silver dimension would increase the density of glass samples.

6.3.2 Morphology

The micrograph and dimension of the AgNPs with different sizes (40 & 90 nm) prepared by modified polyol method were obtained via TEM analysis are shown in Figure 6.3. The silver metal powder (Ag bulk) was used in the range of 2-3.5 μm with ≥99.9% trace metals basis from Sigma Aldrich (CAS No: 7440-22-4).
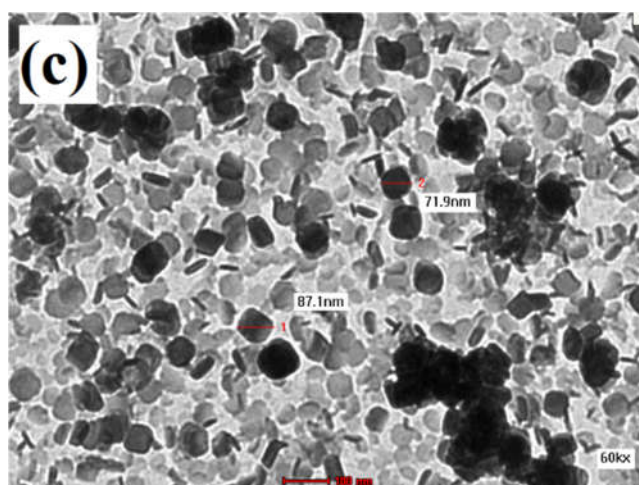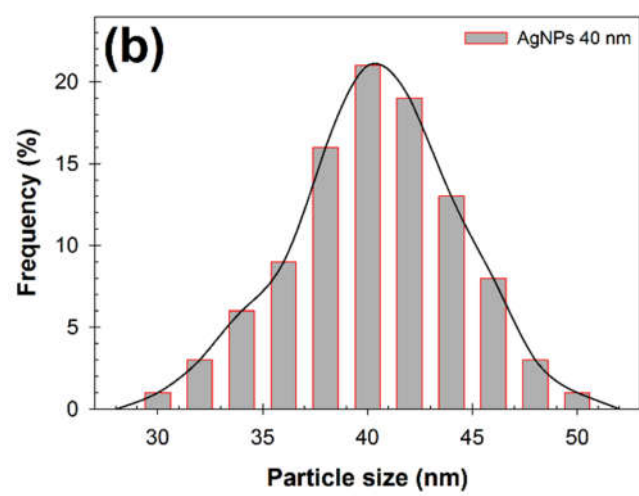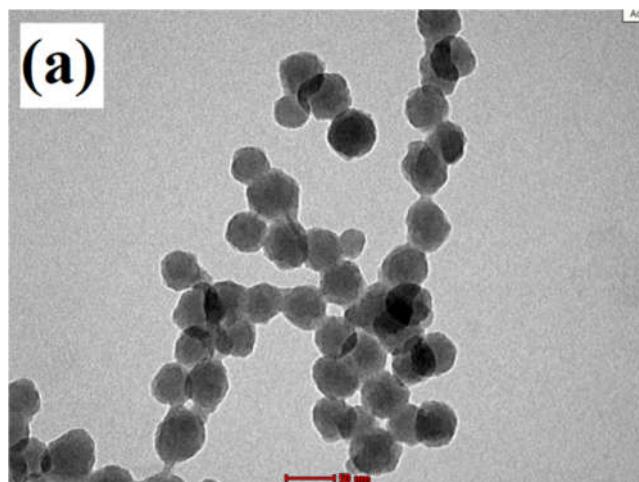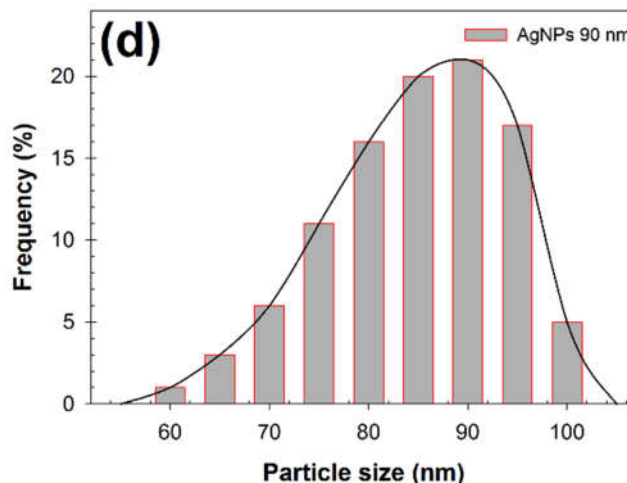
Figure 6.3: TEM micrographs of the AgNPs with different sizes; (a) AgNPs-40 nm (scale bar: 50 nm), (b) size distribution of AgNPs-40, (c) AgNPs-90 nm (scale bar: 100 nm) and (d) size distribution of AgNPs-90nm prepared by modified polyol method.

The images in Figure 6.3(a & c) show a structure consisting of irregular spherical for AgNPs (40 nm) and cuboid (90 nm) with the average particle size estimated to be in range of 30-50 nm and 60-100 nm, determined by using the Sigma scan method as shown in Figure 6.3(b & d).Aggregations occur due to large specific surface area and high surface energy between particles. Meanwhile, strong van der Waals forces between the AgNPs surface and polymer functional group results in the particles packed close to each other as discussed in section 4.3.6, Chapter 4. Due to the advantageous properties of AgNPs, addition of these AgNPs to phosphate glass increases the luminescence properties of the glass.

6.3.3 Structural

X-ray diffraction patterns of the AgNPs and Ag-series of radio-photoluminescence glass dosimeter before and after γ-irradiation with 100 Gy are shown in figure 6.4. Dose irradiation at 100 Gy was chosen because it shows good RPL intensity from absorbed dose parameter study.
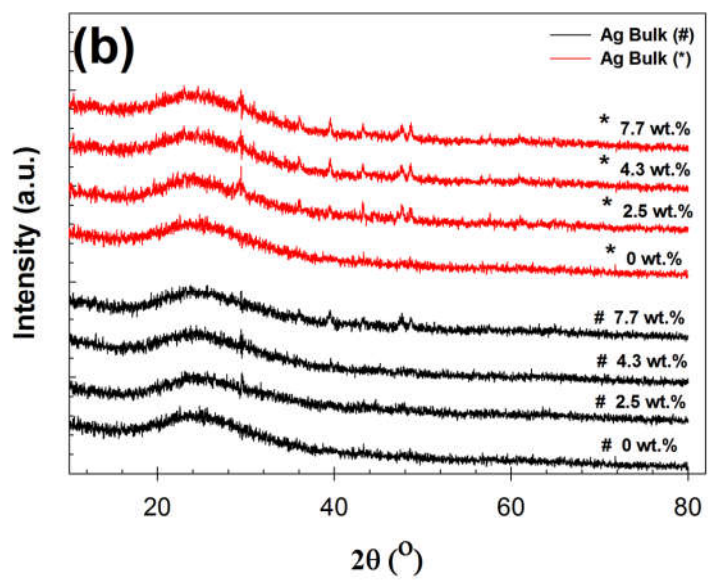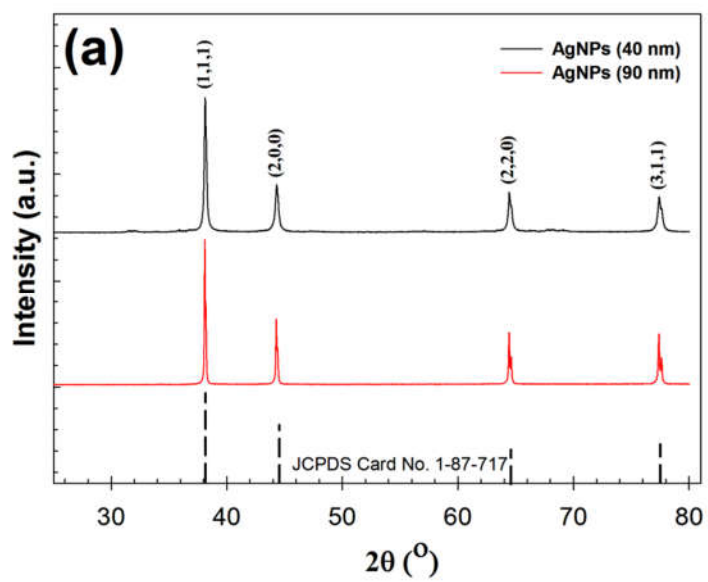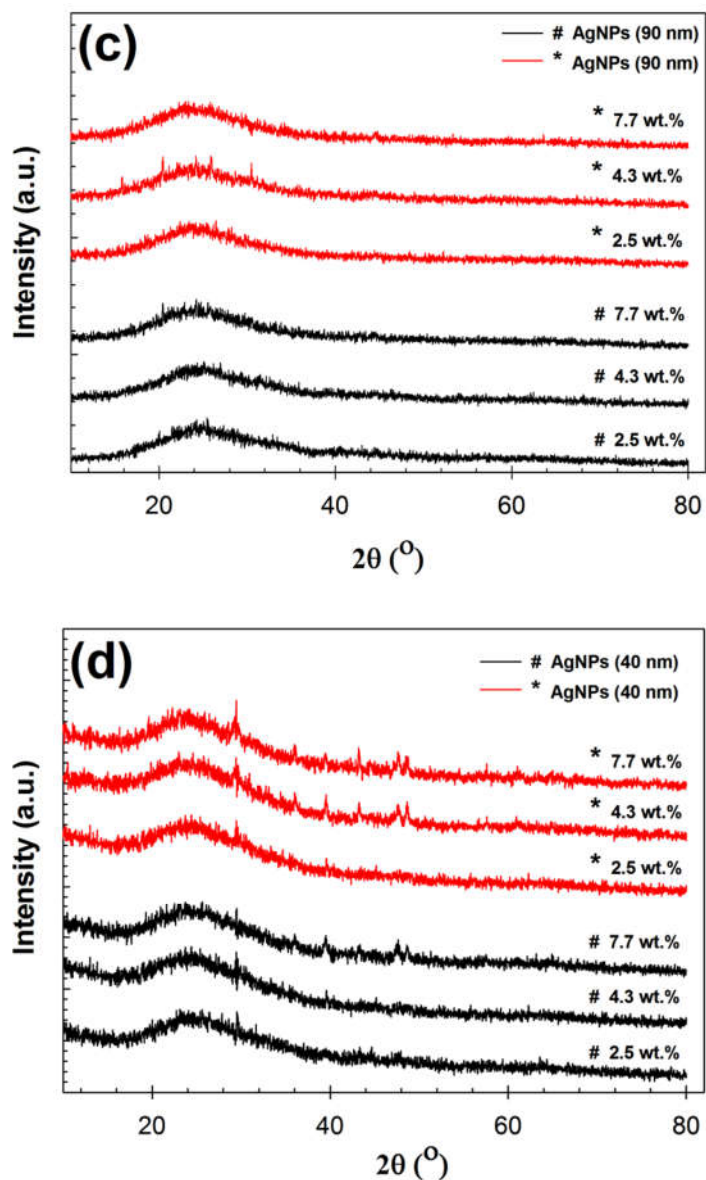
Figure 6.4: X-ray diffraction patterns of the (a) AgNPs; and Ag-series of radio-photoluminescence glass dosimeter; (b) Ag bulk, (c) AgNPs (90 nm) and (d) AgNPs (40 nm). (#) before γ-irradiation and (*) after γ-irradiation. (Irradiation dose = 100 Gy).

The XRD pattern of both AgNPs are is shown in figure 6.4(a). The series of characteristic peaks have been indexed to metallic Ag indicating a face-centred cubic structure, according to JCPDS Card No. 1-87-717, with the lattice parameters; a = 4.0857 nm and space group fm-3m. No diffraction peaks of impurities have been observed, implying that only pure Ag powder has been used in this study.

Figure 6.4(b-d) shows the pattern of the Ag-series of phosphate glasses. When the silver content was increased, no remarkable change was exhibited in the XRD profiles of all samples with differing silver contents (0, 2.5, 4.3 and 7.7 wt.%) before and after γ-irradiation. The pattern displays no sharp peaks, indicating the absence of any crystalline nature observed broad humps in the glass samples, characteristic of the phase at diffraction angles (2θ) to be fully amorphous, indicates that these glass samples are composed of a glassy phase. The series of characteristic peaks were indexed to monoclinic structure of silver phosphate with the lattice parameters; a = 11.86 nm, b = 6.06 nm, c = 7.31 nm and space group P21/n. From the XRD patterns, a strong peak is present the region at 24° (0 2 0), which indicates that silver was doped in phosphate glass and shows the phosphate glass JCPDS Card No. 1-72-122 as shown in figure 6.4(b-d). Therefore, silver diffraction peaks were not well identified, since they were only present in the after mentioned bands. A great deal of interest has been shown in glasses with implanted metallic clusters. As expected, the signal intensity of silver increased in the 7.7 wt.% sample, due to a higher amount of silver content. When Ag were partially substitute P_2O_5, sign of the corresponding contribution remains the same, but the absolute value decreases (atomic factor of Phosphorus is lower). Thus, the contribution was negative and the intensity will increase.

6.3.4 Chemical bonding

In order to obtain more information about the prepared glasses, FTIR measurements were performed. Figure 6.5-6.7 shows the FTIR spectrum of RPLGD's samples before and after γ-irradiation with 100 Gy doses (control dose for comparison before and after γ-irradiation) for the Ag-series doped phosphate glasses. The positions of the bands for the Ag-doped phosphate glass system are summarized in Table 6.2.
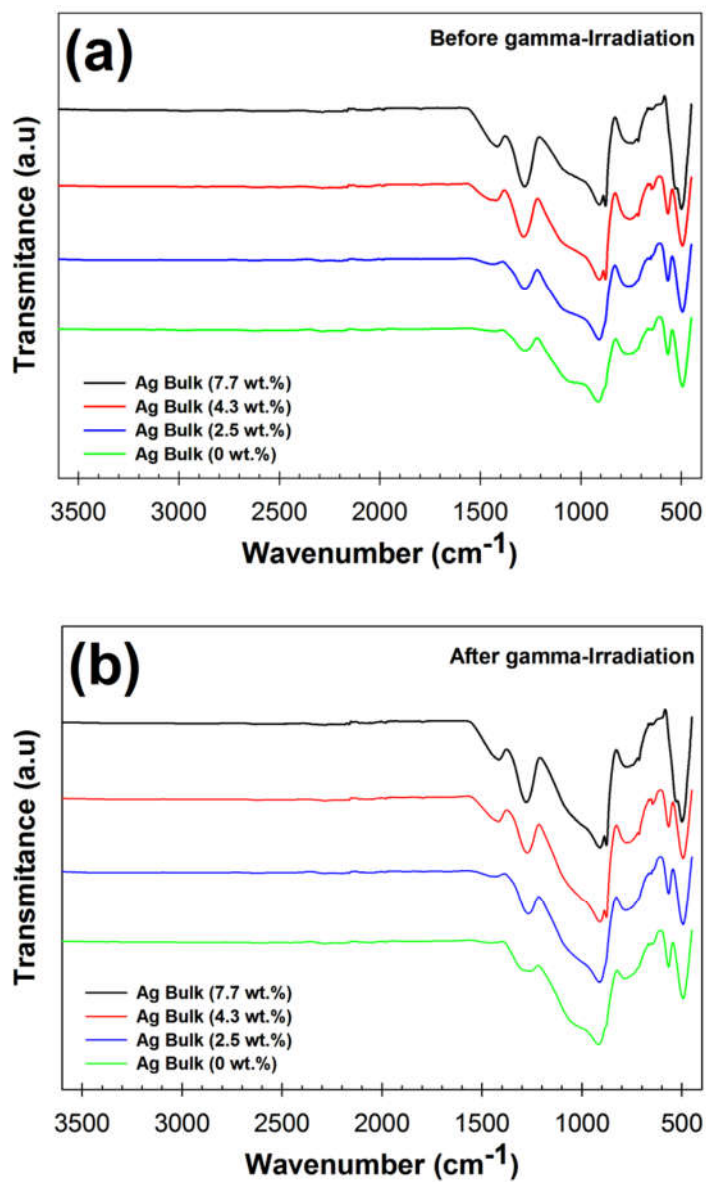
Figure 6.5: FTIR spectra for the RPLGDs doped with different wt.% of silver bulk and silver nanoparticles before and after γ-irradiation.
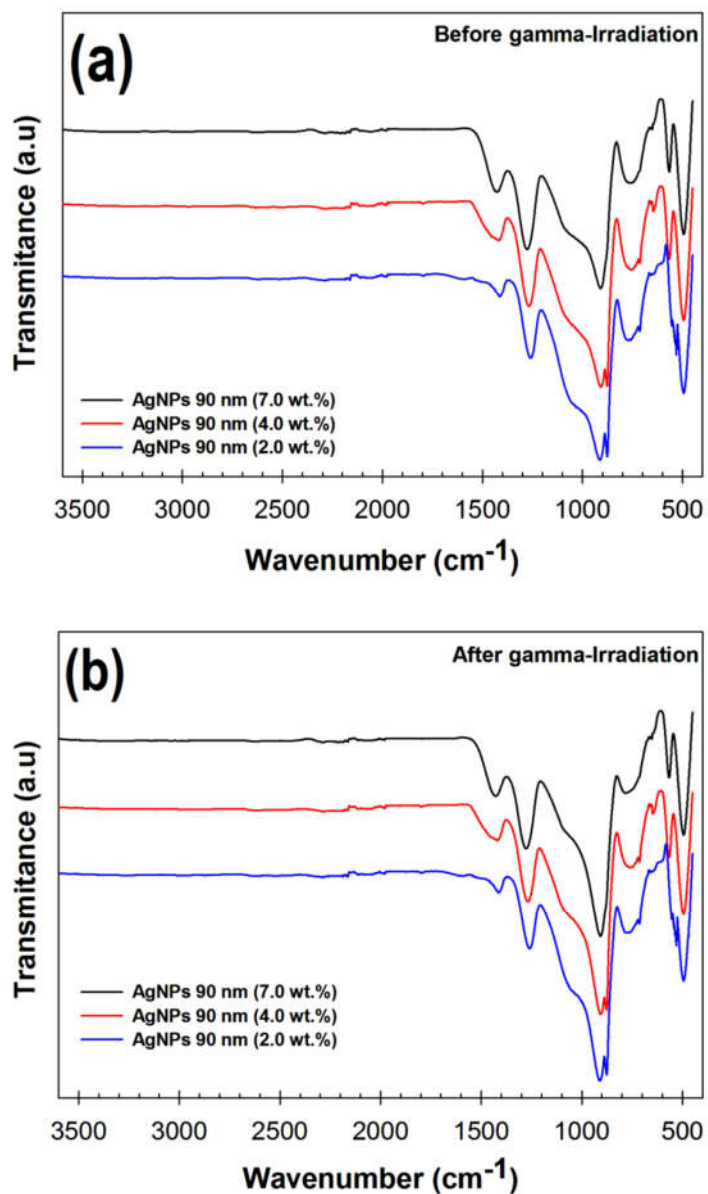
Figure 6.6: FTIR spectra for the RPLGDs doped with different wt.% of silver nanoparticles (90 nm) before and after γ-irradiation.
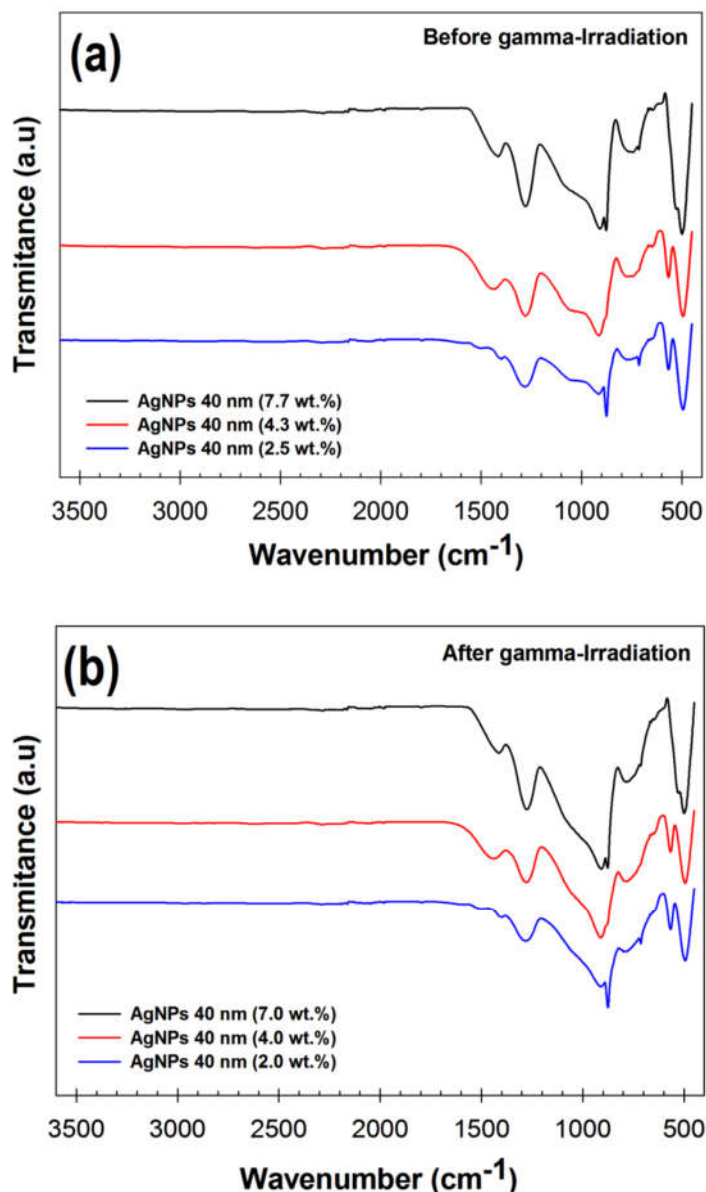
Figure 6.7: FTIR spectra for the RPLGDs doped with different wt.% of silver nanoparticles (40 nm) before and after γ-irradiation

A comparison of spectra in Figure 6.5-6.7 show that the samples before and after γ-irradiation shows nearly similar IR transmission spectra, due to similar composition of the glass matrix, except for a change in the intensities of some peaks in same region for different amount of Ag, which seems to be having less or negligible effect on IR absorption spectra. However, a main observation after 100 Gy of γ-irradiation is the obvious intensity increase of some peaks in the 800-1017 cm^{-1} range dominated by P-O-P linkages. This clearly indicates the breaking of these P-O-

P linkages, which produces more non-bridging oxygen. This is associated with an increase in the intensity of band due to P=O bond at 1187 cm^{-1}, which confirms the idea of breaking P-O-P linkages in the glass [148].

Besides, the bands in the region of 1400-500 cm^{-1} show several strong characteristic bands of phosphate glass. There is no significant difference in the line shapes of the spectra, because all the samples contain higher than 50 wt.% P_2O_5, as expected. These spectra consist of two main sets of IR absorption bands in the low and high frequency regions due to phosphate group and O-H molecule (bending mode), respectively [145]. The shoulder observed at 1425 cm^{-1} is due to the stretching vibration mode of the P=O bond. Several researchers have reported that the band correlating to the stretching vibration of doubly bonded oxygen could be found in the frequency range of 1230-1390 cm^{-1} [145 & 155]. The band at about 1281 cm^{-1} is assigned to the asymmetrical stretching vibration of O-P-O and P=O groups, v_{as}(O-P-O)/ v_{as} (P=O), while the medium broad band at 1100 cm^{-1} is related to the symmetric stretching vibration of that group, v_s(O-P-O) [145]. The 1100 cm^{-1} band is the dominant feature of the spectra and has been assigned to P-O- groups. Moreover, increasing the quantity of the silver component will resulting in alteration of each band in the region of 1200-1500 cm^{-1}, confirming the modifying behaviour of silver [142].

The phosphorus non-bridging oxygen portion of PO_4 tetrahedral in a chain structure has been referred to as a P-O- unit. The asymmetric stretching vibration of the metaphosphate group, v_{as}(PO_3) was observed in the range of 1012-1153 cm^{-1}. This indicates that the bands due to v_{as}(PO_3) can interfere with the band at 1100 cm^{-1}. The broadening observed in the region of 900-1105 cm^{-1} may be due to the interference of v_s(PO_3) with the spectral range 1000-1060 cm^{-1}. The shoulder around 878 cm^{-1} is assigned to the asymmetric stretching vibration of P-O-P linkages, v_{as}(P-O-P), while the relatively weak band around 764 cm^{-1} is due to the symmetric stretching vibration of that linkage, v_s(P-O-P). The region below 600 cm^{-1} is usually assigned to the vibration of metals [146]. The broad band at about 525-539 cm^{-1} may be assigned to the harmonics of P-O-P bending vibration as well as to the deformation mode of PO- group. The wavenumbers of 480 and 510 cm^{-1} correspond to the stretching and Ag-O symmetrical vibrations in PO_4. Therefore, the production

of electron-hole pairs during γ-irradiation could provide another path for bond rearrangement, reducing the constraints on structural relaxation but tends not to be reversible [142]. The relaxation process releases some of the excess energy stored in the structure, resulting in change in the bond angle.

Table 6.2: Vibrational modes of the FTIR spectra of Ag-doped phosphate glass samples

No.	Vibrational modes	Wavenumbers (cm^{-1})
1.	V_s(P-O-H)	2346-2926
2.	Stretching mode of P=O	1425
3.	Asymmetric stretching O-P-O V_{as}(O-P-O)/(P=O)	1281
7.	Symmetric stretching V_s(O-P-O)/PO$^-$	1100
8.	V_{as}(PO$_3$)	1012-1153
9.	V_s(PO$_3$)	1000-1060
10.	Asymmetric stretching P-O-P V_{as}(P-O-P)	878
11.	V_s(P-O-P)	764
12.	Harmonics of P-O-P bending vibration/deformation mode of PO$^-$	525-539
13.	V_s(Ag-O)	480 & 510

6.3.5 Photoluminescence

During wet melting processes, $AgPO_4$ was form by interacting between Ag and P_2O_5 as shown in equation 6.1. After annealing treatment, the glasses were irradiated with γ-irradiation and the $AgPO_4$ in RPLGDs can be viewed as Ag^+/PO_4^- related colour centres, produced inside the glasses as shown in equation 6.2. The glass changed colours from colourless to slightly yellow after γ-irradiation. When the tetrahedron of PO_4^- is exposed to γ-radiation, it loses one electron and forms a positron hole, hPO_4 as shown in equation 6.3. The electron released from the PO_4^- will combine with Ag^+ to form an $Ag°$ as shown in equation 6.4 which is an electron trap within the forbidden band. Similarly, hPO_4 will combine with Ag^+ to become an Ag^{2+} as shown in equation 6.5. The process where Ag^+ ions trap holes is the main

reason of the stabilization phenomenon of RPL centres. Both Ag° and Ag^{2+} form the colour centres. The colour centres formation mechanisms are shown below.

$$2Ag + P_2O_5 + 3H_2O \rightarrow 2AgPO_4 + 3H_2 \qquad (6.1)$$

$$AgPO_4 \rightarrow Ag^+ + PO_4^- \qquad (6.2)$$

$$PO_4^- \rightarrow hPO_4 + e^- \qquad (6.3)$$

$$Ag^+ + e^- \rightarrow Ag^o \text{ (electron trap)} \qquad (6.4)$$

$$hPO4 + Ag^+ \rightarrow Ag^{2+}/PO_4^- \text{ (hole trap)} \qquad (6.5)$$
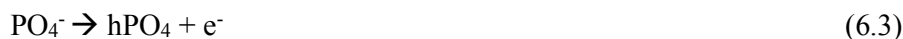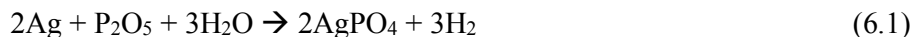
When these colour centres were excited with 325 nm UV light, the electrons in Ag° and Ag^{2+} are excited to higher energy levels and emit 570-680 nm visible orange light, then return to the original colour centres. These electrons will not return to the valence band of the glass material directly because the energy gained by electrons from the UV light is not high enough to let electron escape from colour centres. Therefore, the colour centres in the glasses do not disappear after readout unless heat treatment was applied. Hence, this glass can be read repeatedly.
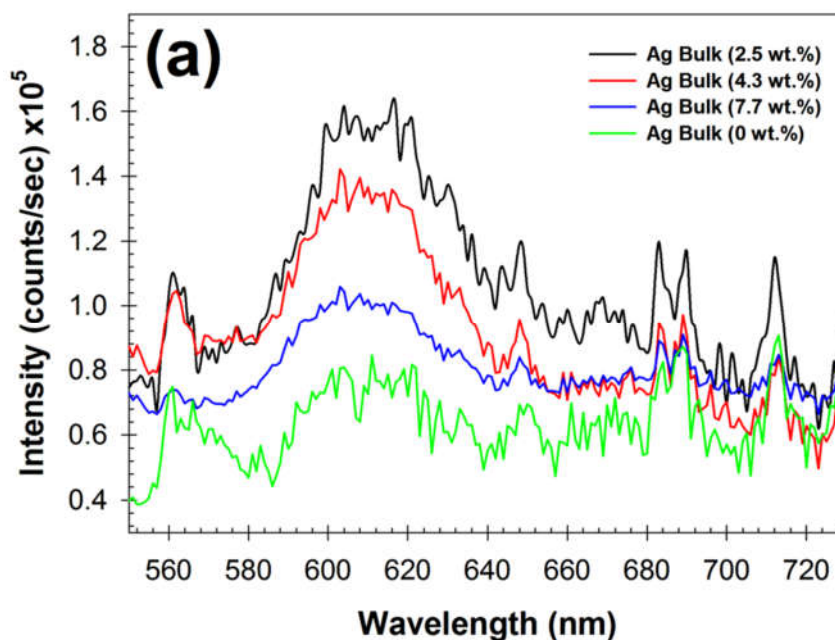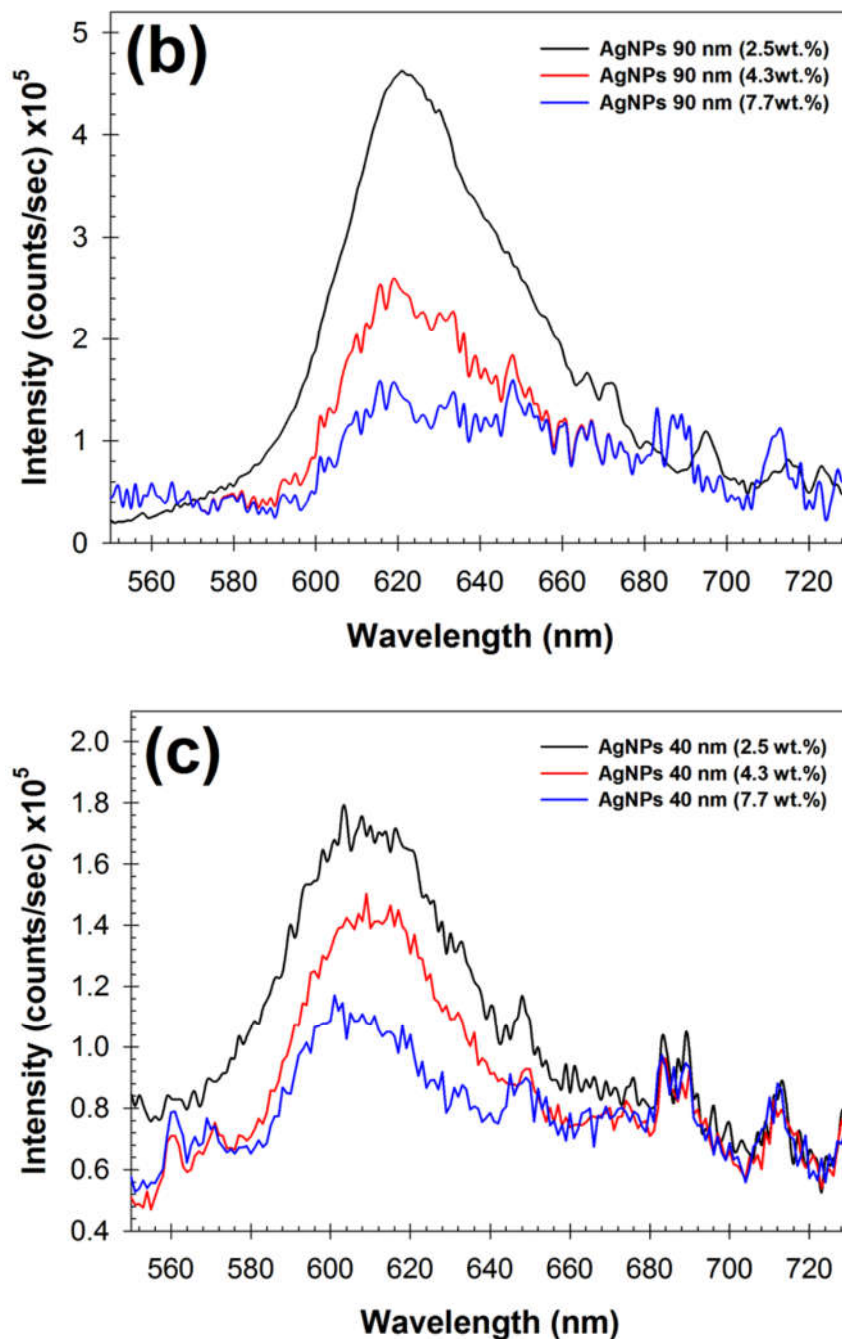
Figure 6.8: RPL spectra of the Ag-series phosphate glass; (a) Ag bulk, (b) AgNPs 90 nm and (c) AgNPs 40 nm after γ-irradiation with 100 Gy irradiated dose. The samples were excited at 325 nm.

Figure 6.8 shows the radiophotoluminescence spectra of the Ag-series activated phosphate glass excited at 325 nm after γ-irradiation with an absorbed dose of 100 Gy. After γ-irradiation treatments, all Ag-series samples have radio-

photoluminescence signals. The main feature is composed from excitation at 325 nm, which consequently released an emission between 570 up to 680 nm with a band located around 620 nm. The relative intensity of the band at 560 nm appears to indicate that different natures of luminescent centres are most likely occurring [154]. The existence of this emission band can be related to the formation of significant amount of Ag° centres within the glass network. All these observations are consistent with a decrease of the emission of isolated silver ions showing that silver is definitely acting as the electron trap [137]. From figure 6.8, the intensity peaks were increasing proportionally with wt.% of Ag content due to the colour centres forming within the glass [137]. Moreover, Ag-series phosphate glasses with AgNPs-90 nm in figure 6.8(b) shows the highest RPL peaks intensity followed by AgNPs-40 nm in figure 6.8(c) and Ag bulk in figure 6.8(a) due to their special characteristics of high surface to volume ratio and has strong optical absorption in the visible region due to localized surface plasmon resonance (LSPR) of free electrons in nanometric size of AgNPs [94]. Moreover, the LSPR in AgNPs are depending on the size and surrounding medium, these resonances were due to charge oscillation close the sphere surface and there show the maximum intensity of electric field. At large-sized AgNPs (90 nm), light scattering is more significant than small-sized AgNPs [156]. Therefore, Ag-series of phosphate glass with AgNPs-90 nm content were used to further analysis for dosimetric sensitivity.
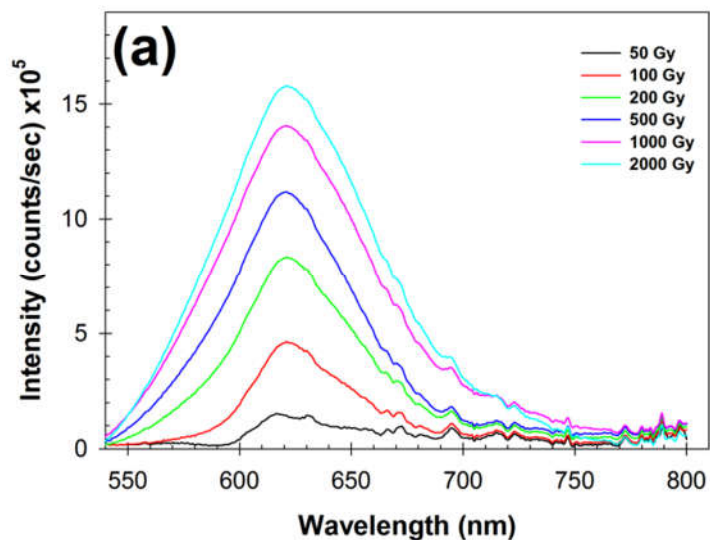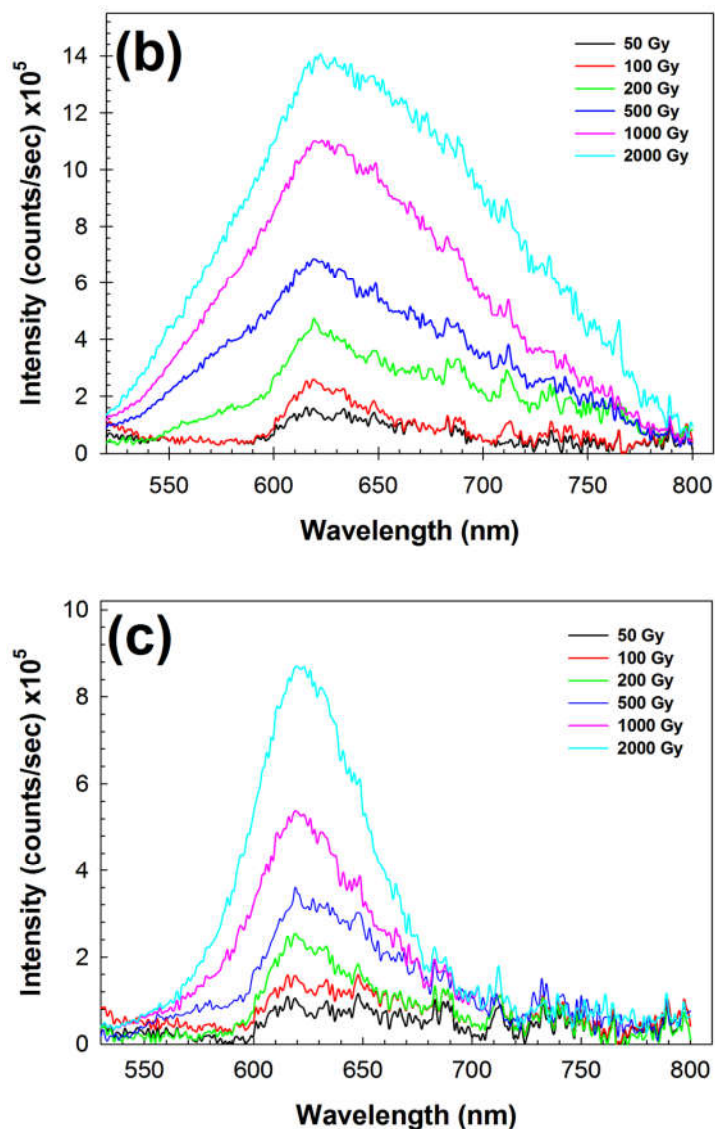
Figure 6.9: Emission spectrum of RPLGD samples; (a) 2.5 wt.%, (b) 4.3 wt.% and (c) 7.7 wt.% of AgNPs-90 nm contents at different irradiation doses. The samples were excited at 325 nm.

In order to determine the dosimetric sensitivity of RPLGD toward irradiation dose, the RPLGD samples with AgNPs-90 nm were chosen because it's shows the highest RPL peaks intensity among samples. Therefore, AgNPs (90 nm) doped phosphate glasses were irradiated with γ-irradiation at varying doses from 50 Gy to 2 kGy, respectively. The RPL spectra were measured to investigate the emission of silver ions corresponding to the dipolar electric transition $4d^{10} \leftrightarrow 4d^9 5s^1$ [18]. Therefore, glass samples with 2.5 wt.% in Figure 6.9(a) shows the highest intensity

of RPL peak followed by 4.3 wt.% in figure 6.9(b) and 7.7 wt.% in Figure 6.9(c), respectively. The intensity peaks were increasing proportionally with absorbed dose due to the colour centres forming within the glass [18]. In brief, the interpretation of emission spectra is affected by variation in site symmetries from site to site of the colour centres, which are the colour centres forming gradually with absorbed dose and thus, increase in the RPL-intensity peak at visible region around 620 nm band. Moreover, the increase of RPL-intensity after a definite absorbed dose values may be explained in terms of build-up in the colour centres of $Ag°$, Ag^+ and Ag^{2+} within the forbidden band [18]. Additionally, when the concentration of phosphorus is high, some additional peculiarities may be observed in the case of disordered materials (AgNPs). That is structural non-equivalence of centres with corresponding transformation of single decay kinetics (exponent) to a wide distribution of parameters during irradiation. Center responsible for UV luminescence participates in recombination processes of hole and electron.

6.4   Conclusion

In summary, we performed optical, physical and chemical measurements on Ag-series of RPLGDs to clarify the origin and characteristics of the γ-induced colour centres. It was established that the phosphate glasses suitable for dosimeter control possess density values ranging from 2.15 to 2.78 g/cm^3. The glass density values are composition dependent, for example the density increases with increasing Ag particles in the vitreous network. The micrograph of the AgNPs with different sizes were obtained via TEM analysis showing a structure consisting of irregular spherical for AgNPs (40 nm) and cuboids (90 nm) with average of particle size, estimated to be in range of 30-50 nm and 60-100 nm, respectively. Aggregations occur due to large specific surface area and high surface energy between particles. Besides, FT-IR spectra of Ag-doped phosphate glasses have been studied before and after γ-irradiation. The IR absorption spectra of Ag-doped phosphate glasses provide information about the main characteristics frequencies for phosphate bonds present in the glass network such as P=O, P-O-P, O-P-O and P-O-H. The presence of P-O-H bond indicates the hygroscopic nature of these phosphate glasses. The decrease in oxygen content of glass sample after γ-irradiation was indicated by rearrangement in the glass sample. This creates oxygen vacancy in the glass sample, which is noticed

as generation of defects in the optical observations. The optical properties such as RPL emission spectra of all Ag-series phosphate glass were also investigated in this chapter. The orange RPL at 620 nm was associated with the 325 nm of the excitation band and this optical activity was due to the Ag^{2+} centres. Apart from that, Ag-series RPLGD shows the highest sensitivity at 4.3 wt.% of silver content. Finally, the effect of γ-irradiation was observed in the form of change in the structural units of phosphate glass due to breaking and rearrangement of bonds in the glass network. All these changes were found to be dependent on the composition of the glasses system. Currently, the developments of a high sensitivity RPLGD were continuously being investigated in our laboratory.

Chapter 7

7. Summary and Future Work

7.1 Summary

Radio-photoluminescence glass dosimeter (RPLGD) was chosen for the estimation of dose absorbed by radiation because RPLGD having low energy dependence, high sensitivity and good chemical stability. Besides, it also have some excellent features such as reproducibility, repeatable measurement, information about radiation type from reading and small dispersions among samples (Fuminobu et al. 2018).

To begin with, RPLGDs were prepared using oxide glass by wet melting processes. Among oxide glasses, phosphate based glasses was chosen due to their ability to accommodate large concentrations of active ions without losing their useful properties of the material (Aya Mahmoud 2018). Moreover, phosphate glasses have attracted much interest in various scientific and technological fields, after the development of novel compositions of superior chemical and physical properties in the recent past. Phosphate glasses are relatively easy to prepare and offers a large range of compositional possibilities, which facilitates in tailoring the physical, chemical and optical properties of interest for specific technological applications. Therefore, in this dissertation we have investigated some technologically important phosphate based glasses, which is radio-photoluminescence glass dosimeter. The present investigations are mainly focused on preparation of glass and silver nanoparticles, thermo-physical properties and structural aspects of different chemical composition based phosphate glass. Investigations carried out on the effect of silver nanoparticles properties with their sizes, the effect phosphate glass with different chemical composition and the effect of silver's sizes on optical properties of radio-photoluminescence glass dosimeter are discussed in Chapters 4, 5, and 6, respectively. This chapter summarizes the work carried out in the thesis and presents the important finding along with future direction of the work.

Silver nanoparticles (AgNPs) with different sizes have been investigated and observed a hue changing of AgNPs sols as a function of polyethyleneimine (PEI) and poly(sodium 4-styrene sulfonate) (PSS) concentrations with a constant concentration of silver precursor using a chemical reduction method. The main aim was to investigate the hue changing solutions of AgNPs as a function of AgNPs sizes. It has been demonstrated that a fine control of both PEI and PSS concentrations in different sizes of AgNPs made it possible to changes or reduces its colour due to interaction between AgNPs and specific polymer functional groups. Studies on optical properties of both samples show two spectral regions consisting of a single sharp surface plasmon resonance band at 400 and 700 nm. Two width regions of this spectrum are due to the presence of more than one surface plasmon resonances related to transverse and longitudinal electron oscillations. Based on the comprehensive SERS analysis, it is concluded that the existence of different amino groups of PEI adsorbed onto AgNPs surface either by interaction with citrate that react as a linker between AgNPs and PEI or a coordination complex direct with the AgNPs surface. In contrast, the SERS peaks of AgNPs/PSS broadening around sulfonate group agree well with the result of adsorbed PSS onto the AgNPs surfaces. SERS results were supported by absorbance spectra, which suggest that adsorption of PEI and PSS on the AgNPs surface results decrease in the maximum absorption intensity at violet region due to decreases of surface plasmon resonance, resulting colourless and yellow sols of both AgNPs/PEI and AgNPs/PSS at the end of experiments. This information is useful to develop and controlled the sizes of AgNPs preparation to optimize the RPLGDs' performance.

The primary aim of investing phosphate glasses was to study the effect of chemical content addition on various thermo-physicals, chemical and optical properties of phosphate glasses, as these glasses have potential application in dosimetric devices. It was found that hardness (HRA) values increased with increasing aluminium (Al) content. Additionally, variation in T_g, T_d and density values for these glasses are in accordance with the structural changes taking place in the glass as a function of composition. Furthermore, different synthesized compounds also affect the radiation sensitivity. RPLGD series shows the highest sensitivity between 2.0 to 4.0 wt.% of silver content. Apart from that, the structural

studies provide information about the main characteristics frequencies for phosphate bonds present in the glass network such as P=O, P-O-P and O-P-O. The spectra also revealed that TiO_2 enters the glass network resulting in the progressive conversion of Q2 structural units into Q1 (up to 10 wt.% TiO_2) and Q0 structural units (more than 10 wt.% TiO_2). Cross-linking provided by P-O-Ti and P-O-Al bonds between shortened discrete 'P' structural units (for x ≤ 10 wt.%) results into a stronger and rigid glass network. Based on optical studies, excess Na compound decrease the penetration capability of UV light. However, Na is important for mobility of activator ions in glass matrix. Thus, the curve with 3.0 wt.% of $NaNO_3$ was chosen as the best result due to the highest penetration rate of the glass system. Higher content of Al will reduced the penetration rate values due to the conversion of bridging oxygen (BO) to non-bridging oxygen (NBO) atoms brought about by the Al_2O_3 incorporation in the glass. Additionally, the penetration capability of UV light was enhanced after the wt.% of P_2O_5 were increased due to higher NBO content in the glass system. From emission spectra, the glass with incorporation of TiO_2 up to 10 wt.%, the wavelength corresponding to the emission maximum remained the same, even though there is a slight change in the line shape. However, above 10 wt.% of TiO_2 at the expense of P_2O_5 incorporation in the glass, the emission maximum shows significant shifting to higher wavelength at 528 nm indicating a decrease in the energy corresponding to localized levels. The changes are with respect to the creation of more NBO atoms and formation of relatively more ionic P-O-Ti linkages at the expense of more covalent P-O-P linkages (Saoussen et al. 2018). Therefore, further investigation on effect of other chemical content with fixed amount of TiO_2 and P_2O_5, are useful to get deeper understanding about the role of chemical composition in phosphate glasses.

The final aim of investing phosphate glasses was to study the effect of Ag metal sizes doped on RPLGDs sensitivity. Optical, physical and chemical measurements on Ag-series of RPLGDs were performed to clarify the origin and characteristics of the γ-induced colour centres. At a constant chemical content ratio, the density values increased from 2.15 to 2.78 g/cm^3 as the Ag content increased in the vitreous network. Micrographs of AgNPs with different sizes obtained via TEM analysis also proposes a structure consisting of irregular spherical for AgNPs (40

nm) and cuboid (90 nm) with the average particle size estimated to be in range of 30-50 nm and 60-100 nm, respectively. Besides, structural studies of Ag-doped phosphate glasses revealed that the presence of P-O-H bond indicates the hygroscopic nature of these phosphate glasses. The decrease in oxygen content of glass sample after γ-irradiation was indicated by bond breaking in the glass sample. This creates oxygen vacancy in the glass sample, which has been noticed as generation of defects in the optical observations. From the RPL emission results, the orange RPL at 620 nm was associated with the 325 nm of the excitation band and this optical activity was due to the Ag^{2+} centres. The intensity of RPL emission peaks gives indication of RPLGD's sensitivity, with the peaks intensity comparable with colour centres formation and absorbed doses within the glasses. Therefore, Ag-series RPLGD with AgNPs (90 nm) shows the highest sensitivity, followed by AgNPs (40 nm) and Ag bulk. Moreover, silver content between 3.0 to 5.0 wt.% gives the highest sensitivity toward γ-irradiation due to optimum Ag content within the glasses. Finally, the effect of γ-irradiation was observed in the form of change in the structural units of phosphate glass due to breaking and rearrangement of bonds in the glass network. All these changes were found to be dependent on the composition of the glasses system. Based upon these studies, RPLGD with AgNPs show better sensitivity toward γ-irradiation compared with bulk sized material. Meantime, the development of a high sensitivity RPLGD is continuously being investigated in our laboratory.

7.2 Future Work

The development of new compositions of RPLGD requires the study of the phosphate glass forming regions of new compositional systems as well as the process of making glasses. Requirements of this research are to develop the glasses which have low processing temperature, nontoxic material, high refractive indices and relatively low dispersion while maintaining a good chemical durability. Sometimes, it is hard to find the right compositions for the right application and it always seems to happen in the laboratory that one property needs to be sacrificed to get the other property. For example, the glasses which have high refractive index also have high dispersion. In this thesis, phosphate base glasses were studied and these glasses were modified with different chemical content such as Li_2CO_3, $Al(OH)_3$, $NaNO_3$, $MgSO_3$,

H_3BO_3, and Ag to obtain desirable optical, chemical, physical and thermal properties suitably for dosimetric devices. Due to their strong nonlinear properties and an opportunity of doping with high concentrations of rare earth elements, samarium (Sm) or terbium (Tb) could be a good candidate for next phase of research.

The studies of glass composition presented in this thesis provide a guide for future work. A number of techniques are introduced to understand the relationship between the glass structures and their properties in this study. However, the structure studies with FT-IR spectra are not enough to understand the whole phosphate glass system. The peaks and bands in the short wavenumber (cm^{-1}) regions of the IR spectra need to be assigned to specific types of bonds. It is also necessary to understand the change of the $Ag-PO_4$, O-P-O and P-O-P bonds from phosphate glass system more by using NMR and Mossbauer spectroscopy. In addition, the electron transition within the glasses system has not been studied. Further experimentation need to be carried out to understand the behaviour of build-up and fading effect of the prepared glasses on the kinetic transition response after γ-irradiation. Instead of using phosphate glass, we could consider another glass with lower processing temperature such as tellurite, borate or soda lime glass for new dosimetric devices. This could be another important area of future research interest.

Chapter 8

8. References

[1]   Quintero, A., Patino, G., Soriano, C.Á., Diego, P.C.J., Vilar, P.J., Carmen, P.M., Llorca, D.N., Ballester, F., Vijande, J. & Candela-Juan, C. 2018. Calibration of a thermoluminescent dosimeter worn over lead aprons in fluoroscopy guided procedures. *Journal of Radiological Protection*. 38(2): 1-8.

[2]   Geber-Bergstrand, T., Bernhardsson, C., Christiansson, M., Mattsson, S., & Rääf, C. L. 2017. Optically stimulated luminescence (OSL) dosimetry in irradiated alumina substrates from mobile phone resistors. *Radiation and environmental biophysics*. 57(1), 69-75.

[3]   Aya Mahmoud, H.A. 2018. New Trend in Radiation Dosimeters. *American Journal of Modern Physics*. 7(1): 21-30

[4]   Toshio Kurobori. 2018. Performance characterisation of a real-time fiber dosimetry system using radiophotoluminescent glasses. Japanese Journal of Applied Physics. 57(10): 106402-106409.

[5]   Huang, D.Y.C. & Hsu, S.M. 2011. Radiophotoluminescence glass dosimeter (RPLGD). Prof. Hala Gali-Muhtasib (Ed.), ISBN: 978-953-307-703-1, *Advances in Cancer Therapy. InTech*: 553-568.

[6]   Schulman, J.H., Ginther, R.J., Klick, C.C., Alger, R.S. & Levy, R.A. 1951. Dosimetry of X-rays by radiophotoluminescence. *Journal of Applied Physics*. 22: 1479-1487.

[7]   Regulla, D.F. 1972. Lithium Fluoride Dosimetry Based on Radiophotoluminescence. *Health Physics*. 22(5): 419-421

[8]   Miller, S.D., Endres, G.W.R., 1990. Laser-induced, optically stimulated M-centre luminescence in LiF. *Radiat. Prot. Dosim*. 33(1): 59-62.

[9]   Kahoe, K., Joonyoung, F.J., Heeyeon, P., Myeong-Geun, K.S. & Park, W.K. 2018. Fluorescent Organic Glass with Unique Optical and Mechanical Properties. *Advances Functional Materials*. 28(39): 1-9.

[10]   Brow, R.K. 2000. Review 1: the structure of simple phosphate glasses. *Journal of Non-Crystalline Solids*. 263: 1-28.

[11]   Paramelle, D., Sadovoy, A., Gorelik, S., Free, P., Hobley, J. & Fernig, D.G. 2014. A rapid method to estimate the concentration of citrate capped silver nanoparticles from UV-visible light spectra. *Analyst*. 139: 4855-4861.

[12]   Shangjiu, N., Yin, Z., Jun, L., Nianying, Z. & Wen, Z. 2018. Glass formation and properties of sodium zinc phosphate glasses doped with ferric oxide. *Advances in Applied Ceramics*. 117(6): 319-327.

[13]   Benali, A.H. & Ishak-Boushaki, G.M. 2018. Energy response of FD-7 RPL glass dosimeter compared with LiF Mg, Ti and $Al_{20}0_3$:C dosimeters. *Journal of Instrumentation*. 13: 1-7.

[14]   Shingo, U., Ryota, A., Madoka, O. & Yasuo, H. 2017. Molecular dynamics study on nano-particles reinforced oxide glass. *Journal of the American Ceramic Society*. 101(6): 2266-2276

[15]   Abd El-Ghany, H. 2018. Characterization and Optical Properties of MnO Doped CuO-Containing Phosphate Glass as Absorption Filters. *Journal Of Advances In Physics*. 15: 5983-5996.

[16]   Hsu S-M, Hung C-H, Liao Y-J, Fu H-M, Tsai J-T, Huang Y-H and David, Y.C.H. 2017. Feasibility Study on Applying Radiophotoluminescent Glass Dosimeters for CyberKnife SRS Dose Verification. PLoS ONE, 12(1): 1-11.

[17]   Zheng, W. & Kurobori, T. 2011. Observation and partly characterization of silver nanoparticles in X-ray irradiated radiophotoluminescent phosphate glass. *Nuclear Instruments & Methods in Physics Research Section B-beam Interactions With Materials and Atoms*. 269: 2814-2818.

[18]   Hiroki, K., Yutaka, F., Masanori, K., Go, O., Takayuki, Y. & Keisuke, A. 2018. Analysis of radiophotoluminescence centre formation mechanism in Ag-doped phosphate glasses. *Japanese Journal of Applied Physics*. 57(6): 1-8.

[19]   Yokota, R. & Imagawa, H. 1966. ESR studies of radiophotoluminescent centres in silver-activated phosphate glass. *J. Phys. Soc. Jpn*. 20: 1537-1538.

[20]   Monmi, G., Debjani, B. & Archana, M. 2018. Green synthesis of silver nanoparticles supported on cellulose and their catalytic application in the scavenging of organic dyes. *New Journal of Chemistry*. 42: 10868-10878.

[21]   Zhi, Z., Wenfei, S., Jing, X., Yuanmeng, L., Yanwei, L., Peipei, Y., Jixian., L. & Jianguo, T. 2018. Recent advances in synthetic methods and applications of silver nanostructures. *Nanoscale Research Letters*. 13(54): 1-18.

[22]   Alexandra-Cristina, B., Oana, G., Alexandru, M.G., Laurent, M., Anton, F. & Ecaterina, A. 2018. Biomedical Applications of Silver Nanoparticles: An Up-to-Date Overview. *Nanomaterials*. 8: 681-706.

[23]   Olena, I., Barbara, P., Jacek, G., Dorota, F., Marcin, J., Karol, Z., Grzegorz, N., Zuzanna, P. & Stefan, J. 2018. Silver and ultrasmall iron oxides nanoparticles in hydrocolloids: effect of magnetic field and temperature on self-organization. *Scientific Reports*: 8: 1-14.

[24]   Burduşel, A.C., Gherasim, O., Grumezescu, A.M., Mogoantă, L., Ficai, A. & Andronescu, E. 2018. Biomedical Applications of Silver Nanoparticles: An Up-to-Date Overview. *Nanomaterials (Basel)*. 8(9): 1-13.

[25]   Yoichi Kamikoriyama, Hiroshi Imamura, Atsushi Muramatsu & Kiyoshi Kanie. 2019. Ambient aqueous-phase synthesis of copper nanoparticles and nanopastes with low-temperature sintering and ultra-high bonding abilities. *Scientific Reports*. 9: 899-902.

[26]   Senthilkumar, N., Sakthi Raadha, S. & Udayavani, S. 2015. Synthesis and Characterization of Silver Nanoparticle by Chemical Route Method. *International Journal of Production Engineerin*g, 1: 25-34.

[27]   Shengtao, G. & Honglong, X. 2018. Effect of nanosilver on the thermal stability and thermal decomposition kinetics of poly(acetoacetoxyethyl methacrylate–styrene). *Journal Of Elastomers & Plastics*. 50(8): 1-5.

[28]   Fiévet, F., Ammar-Merah, S., Brayner, R., Chau, F., Giraud, M., Mammeri, F., Peron, J., Piquemal, J.Y., Sicard, L. & Viau, G. 2018. The polyol process: a unique method for easy access to metal nanoparticles with tailored sizes, shapes and compositions. Chemical Society Reviews. 47(14): 5187-5233.

[29]   Iravani, S., Korbekandi, H., Mirmohammadi, S.V. & Zolfaghari, B. 2014. Synthesis of silver nanoparticles: chemical, physical and biological methods. *Research in Pharmaceutical Sciences*. 9(6): 1-17.

[30]   Elliott, S.R. 1984. Physics of amorphous materials. *Longman Group Ltd*. London, New York. ISBN: 0-582-44636-8.

[31]   Shelby, J.E. 1997. Introduction to Glass Science and Technology. *Royal Society of Chemistry*. ISBN 10: 0854045333.

[32]   Rodrigo Rivas, B., Edilio Lázaro, L., Patricia, M., Tim, S., Valeria, P., Pedro, E., Ramírez-G., Magdaleno, M.N. & Marco, L. 2018. Different routes into the glass state for soft thermo-sensitive colloids. *Soft Matter*. 14: 5008-5018.

[33]   Prigogine, I. & Defay, R. 1954. Chemical Thermodynamics. *Longman*, London. ISBN: 0582462835.

[34]   Turnbull, D. & Cohen, M.H. 1970. On the Free-Volume Model of the Liquid-Glass Transition. *The Journal of Chemical Physics*. 52(6): 3038-3046.

[35]   Adam, G. & Gibbs, I.H. 1965. On the temperature dependence of cooperative relaxation properties in glass-forming liquids. *J. Chem. Phys*. 43:139-146.

[36]   Angell, C.A. & Torell, L.M. 1983. Short term structural relaxation processes in liquids: Comparison of experimental and computer simulation glass transitions on picosecond timescales. *J. Chem. Phys*. 78(2): 937-945.

[37]   Wright, A.C., Yarker, C.A., Johnson, P.A.V & Sinclair, R.N. 1985. A neutron diffraction investigation of the structure of phosphorus, barium and lead vanadate glasses. *J. Non-Cryst. Solids.* 76(2-3): 333-350.

[38]   Nicolas, A., Ferrero, E., Martens, K. & Barrat, J.L. 2018. Deformation and flow of amorphous solids: an updated review of mesoscale elastoplastic models. Review Modern Physic. 90: 1-18.

[39]   Zachariasen, W.H. 1932. The atomic arrangement in glass. *J. Am. Ceram. Soc*. 54(10): 3841-3851.

[40]   Warren, B.E. 1941.Summary of work on atomic arrangement in glass. *J. Am. Ceram. Soc*. 24(8): 256-261.

[41]   Jianrui, F., Pengwan, C. & Mo, L. 2018. Existence of fractal packing in metallic glasses: Molecular dynamics simulations of $Cu_{46}Zr_{54}$. *Physical Review B*. 98(2): 24201-24205.

[42]   Si-Da, H., Cheng, S., Pei-Lin, K. & Zhi-Pan, L. 2018. Atomic structure of boron resolved using machine learning and global sampling. *Chemical Sciences*. 9: 8644-8655.

[43]   Siddharth, S., Liping, H., Simona, I. & Walter, K. 2018. New optimization scheme to obtain interaction potentials for oxide glasses. *The Journal of Chemical Physics*. 148(19): 108.

[44]   Laurence, K., Jerome, K., Guiomar, G., Andrew, L. & John, C. 2018. Global Lithium Sources-Industrial Use and Future in the Electric Vehicle Industry: *A Review. Resources*: 1: 1-29.

[45]   Qiaoling, X., Yuwei, L., Lijun, Z., Weitao, Z., David, J.S. & Yanming, M. 2016. Sn(II)-Containing Phosphates as Optoelectronic Materials. Chemistry of Materials 29(6): 1-11.

[46]   Sen, R., Boetti, N.N.G., Hokka, M. & Petit, L. 2019. Optical, structural and luminescence properties of oxyfluoride phosphate glasses and glass-ceramics doped with Yb^{3+}. *Journal of Non-Crystalline Solids: X*. 1: 1-7.

[47]   Zhizhen, Z., Yuanjun, S., Bettina, L., Yong-Sheng, H., Hong, L., Jürgen, J., Linda, F.N., Ce-Wen, N., Joachim, M., Michel, A. & Liquan, C. 2018. New horizons for inorganic solid state ion conductors. *Energy & Environmental Science.* 8(11): 1945-1976.

[48]   Jlassi, I. & Elhouichet, H. 2017. Improvement of thermal and optical properties of lithium phosphate glasses by adding MgO. *Journal of Thermal Analysis and Calorimetry*. 129(12): 1-9.

[49]   Michael, H.P. & Robert, H.F. 2014. The Electronic Structure of Tetraphosphorus-and Tetraarsenic- Trisulphides; Interpretation of their Photoelectron Spectra. A Journal of Physical Sciences. 38(1): 1-12.

[50]   Van Wazer, J.R. 1958. Phosphorus and its Compounds. *Wiley:Interscience Publishers*. New York-London. Vol 1: 954-955.

[51]   Hagg, G. 1935. The Vitreous State. *J. Chem. Phys*. 3: 42-45.

[52]   Uchino, T. & Ogata, Y. 1995. Ab initio molecular orbital calculations on the electronic structure of phosphate glasses. Sodium phosphate glasses. *J. Non-Cryst. Solids*. 181(1): 175-188.

[53]   Galeener, F.L. & Mikkelsen, J.C. 1979. The Raman spectra and structure of pure vitreous P_2O_5. *Solid State Commun*. 30(8): 505-510.

[54]   Vogel, W. in: D.R. Uhlmann, N.J. Kreidl (Eds.). 1991. Optical Properties of Glass. *American Ceramic Society Inc. OH*: 18-19.

[55]   Gard, D.R. 1991. In: Kirk-Othmer Encyclopedia of Chemical Technology, 4th Ed.*John Wiley & Sons*. New York. Vol 18: 669-718

[56]   Ojha, N., Tuomisto, M., Lastusaari, M. & Petit, L. 2018. Upconversion from fluorophosphate glasses prepared with $NaYF_4$:Er^{3+},Yb^{3+} nanocrystals. RSC Advances. 8, 19226-19236

[57]   Samuel, V.F.B., Samuel, D.C., Alexander, N.K., Andrew, R.J., Jose, M.G. & Geoffrey, H. 2018. Phosphinecarboxamide as an unexpected phosphorus precursor in

the chemical vapour deposition of zinc phosphide thin films. Dalton Transaction. 47(28): 9221-9225.

[58]   Mascaraque, N., Takebe, H., Tricot, G., Luis, J., Fierrod, G., Durán, A. & Muñoz, F. 2014. Structure and electrical properties of a new thio-phosphorus oxynitride glass electrolyte. *Journal of Non-Crystalline Solids*. 405: pp. 159-162.

[59]   Narayanan, M.K. & Shashikala, H.D. 2014. Optimization of melt-quenching process parameters for refractive index of barium phosphate glasses using taguchi method. *Procedia Materials Science*. 5: pp. 303-310.

[60]   Da-Ming, G., Bohan, Z., Haichao, L., Kei, M., Kazuyoshi, K., Zhiyong, H., Maomao, Z., Huaping, W., Jie, C. & Kazuki, N. 2018. Synthesis of a hierarchically porous niobium phosphate monolith by a sol–gel method for fructose dehydration to 5-hydroxymethylfurfural. *Catalysts and Science Technology*. 8: 3675-3685

[61]   Bordeenithikasem, P., Liu, J., Kube, S.A., Li, Y., Ma, T., Scanley, B.E., Broadbridge, C.C., Vlassak, J.J., Singer, J.P. & Schroers, J. 2017. Determination of critical cooling rates in metallic glass forming alloy libraries through laser spike annealing. *Scientific reports*. 7(1): 7155-7159.

[62]   Ehrt Doris. 2015. Review: Phosphate and fluoride phosphate optical glasses - properties, structure and applications. *European Journal of Glass Science and Technology Part B Physics and Chemistry of Glasses*. *Physical Chemical of Glasses: Europe of Journal Glass Scientific Technoogy. B*. 56(6): 217-234.

[63]   Phakphum, A., Nicholas, A.B. & Michael, D.W. 2018. Selecting passive dosimetry technologies for measuring the external dose of terrestrial wildlife. *Journal of Environmental Radioactivity*. 182: 128-137.

[64]   Yokota, R. & Muto, Y. 1971. Silver-activated phosphate dosimeter glasses with low energy dependence and higher sensitivity. *Health Phys*. 20: 662-663.

[65]   Perry, J.A. 1987. RPL dosimeter, Radiophotoluminescence in Health Physics. Bristol United Kingdom. Adam Hilger.

[66]   Fuminobu, S., Taichi, H., Shingo, T., Sachie, K. & Hiroyuki, M. & Isao, M. 2018. Development of string-shaped radiophotoluminescence dosimeter for high-radiation field. Radiation Measurements. 111: 1-5

[67]   Fan, S., Yu, C., He, D. & Hu, L. 2013. Preparation and Property of Radio-Photoluminescence Dosimeter Glass. *Atomic Energy Science and Technology*. 47(3): 502-507.

[68]   Knežević, Ž., Stolarczyk, L., Bessieres, I., Bordy, J.M., Miljanić, S. & Olko, P. 2013. Photon dosimetry methods outside the target volume in radiation therapy: Optically stimulated luminescence (OSL), thermoluminescence (TL) and radiophotoluminescence (RPL) dosimetry. *Radiation Measurement*. 57(1): 9-18

[69]   Lee, J.H., Lin, M.S., Hsu, S.M., Chen, I.J., Chen, W.L. & Wang, C.F. 2009. Dosimertry characteristics and performance comparisons: Environmental radiophotoluminescent glass dosemeters versus thermoluminescent dosemeters. *Radiat Measur*. 44(1): 86-91.

[70]   Miyamoto, Y., Takei, Y., Nanto, H., Kurobori, T., Konnai, A., Yanagida, T., Yoshikawa, A., Shimotsuma, T., Sakakura, M., Miura, K., Hirao, K., Nagashima, Y. & Yamamoto, T. 2011. Radiophotoluminescence from Silver-Doped phosphate Glass. *Radiation Measurements*. 46: 1480-1483.

[71]   Yamamoto, T., Maki, D., Sato, F., Miyamoto, Y., Nanto, H. & Iida, T. 2011. The recent investigations of radiophotoluminescence and its application. *Radiat Measur*. 46(12): 1554-1559.

[72]   Manninen, A.L. 2014. Clinical applications of radiophotoluminescence (RPL) dosimetry in evaluation of patient radiation exposure in radiology determination of absorbed and effective dose. PHD thesis, Oulu University Hospital

[73]   Hubbell, J.H. & Seltzer, S.M. 1996. Tables of X-Ray Mass Attenuation Coefficients, Radiation and Biomolecular Physics Division, PML, NIST. *Scientific Research*. 1-20

[74]   Mizuno, H., Kanai, T., Kusano, Y., Ko, S., Ono, M., Fukumura, A., Abe, K., Nishizawa, K., Shimbo, M., Sakata, S., Ishikura, S. & Ikeda, H. 2008. Feasibility

study of glass dosimeter postal dosimetry audit of high-energy radiotherapy photon beams. *Radiother Oncol*. 86(2): 258-263.

[75] Kadoya, N., Shimomura, K., Kitou, S., Shiota, Y., Fujita, Y., Dobashi, S., Takeda, K., Jingu, K., Matsushita, H., Namito, Y., Ban, S., Koyama, S. & Tabushi, K. 2012. Dosimetric properties of radiophotoluminescent glass detector in low-energy photon beams. *Med Phys*. 39(10): 5910-5916.

[76] Piesch, E., Burgkhardt, B. & Vilgis, M. 1993. Progress in Phosphate Glass Dosimetry: Experiences and Routine Monitoring with a Modern Dosimetry System. *Radiat Prot Dosim*. 47(1-4): 409-414.

[77] ATGC & Asahi Techno Glass Corporation. 2004. Glass dosimetry system, FGD-1000. Instruction Manual Ver.1.3.0.0.

[78] Online: http://www.usho.co.jp/en/corp/index.html. 20 Feb 2015, Usho Optical Systems Co. , Ltd. 1-10-16, Hanakawa, Nishiyodogawa-ku, Osaka 555-0023 Japan.

[79] Piesch, E. & Burgkhardt, B. 1994. Photoluminescence dosimetry: the alternative in personnel monitoring. *Radioprotection*. 29(1): 39-67.

[80] Becker, K. 1965. High γ-Dose Response of Recent Silver-Activated Phosphate Glasses. *Health Physics*. 11(6): 523-529

[81] Oliveira, T.J.S., Junior, E.P.L., Paula, A.S., Domingos, M.O., Navarro, D.R. & Prado, M.H. 2017. Thermal Analysis of Two Niobo-Phosphate Glasses. *Short Communication, Biomater Medical Application*. 1(1): 1-2.

[82] Cheka, J.S. 1964. Stability of radiophotoluminescence in metaphosphate glass. *Health Physic*. 10: 363-368.

[83] Cheka, J.S. 1968. Long-term stability of radiophotoluminescence in metaphosphate glass. *Health Physic*. 15: 363-368.

[84] Khan, M.Z.H., Tareq, F.K., Hossen, M.A. & Roki, M.N.A.M. 2018. Green synthesis and characterization of silver nanoparticles using Coriandrum Sativum leaf extract. *Journal of Engineering Science and Technology*. 13(1): 158-166.

[85]   Online: https://wiki.anton-paar.com/en/   the-principles-of-dynamic-light-scattering/# references. 21 Feb 2017, Particle size analysis - Dynamic light scattering (DLS). *International Organization for Standardization*. ISO 22412:2017.

[86]   Online: https://www.malvernpanalytical.com/en/products/category/x-raydiffractometers. 22 June 2017. Crystalline analysis – X-ray diffractometer (XRD).

[87]   Wiesendanger, R. 1994. Scanning probe microscopy and spectroscopy: Methods and applications. *Cambridge University Press*. Cambridge, New York.

[88]   Mysen, B.O., Finger, L.W., Virgo, D. & Seifert, F.A. 1982. Curve-fitting of Raman spectra of silicate glasses. *American Mineralogist*. 67: 686-695.

[89]   Pantic, I. 2014. Application of silver nanoparticles in experimental physiology and clinical medicine: Current status and future prospects. *Rev. Adv. Mater. Sci*. 37: 15-19.

[90]   Pannaree, S., Yi-Ting, C., Varadee, V., Maria, D.M. & Randall, T.L. 2018. Bimetallic Nanoparticles: Enhanced Magnetic and Optical Properties for Emerging Biological Applications. *Applied Sciences*. 8(7): 1106-1113.

[91]   Djamel, G., Abdul aziz, A., Mabrouk, T., Mohamed, A. & Noureddine, A.M. 2018. Nanotechnology Phenomena in the Light of the Solar Energy. *Journal of Energy, Environmental & Chemical Engineering*. 3(1): 1-8.

[92]   Xun, F. & Yang, C. 2018. Drug delivery targets and systems for targeted treatment of rheumatoid arthritis. *Journal of Drug Targeting*. 26(10): 845-857.Yamamoto, T., Maki, D., Sato, F., Miyamoto, Y., Nanto, H. & Iida, T. 2011. The recent investigations of radiophotoluminescence and its application. *Radiat Measur*. 46(12): 1554-1559.

[93]   Xavier, J., Vincent, S., Meder, F. & Vollmeret, F. 2017. Advances in optoplasmonic sensors – combining optical nano/microcavities and photonic crystals with plasmonic nanostructures and nanoparticles. *Nanophotonics.* 7(1): 1-38.

[94]   Gonzalez,´A.L., Noguez, C., Beranek, J. & Barnard, A.S. 2014. Size, shape, stability, and colour of plasmonic silver nanoparticles. *J. Phys. Chem. C*. 118: 9128-9136.

[95] Indranil, M., Shipra, R., Poulomi, R. & Raju, P. 2018. Silver nanoparticles (AgNPs) as a contrast agent for imaging of animal tissue using swept-source optical coherence tomography (SSOCT). *Laser Physics*. 28(1): 1-8.

[96] Gutierrez, L., Aubry, C., Cornejo, M. & Croue, J.P. 2015. Citrate-Coated Silver Nanoparticles Interactions with Effluent Organic Matter: Influence of Capping Agent and Solution Conditions. *Langmuir*. 31: 8865-8872.

[97] Koyani, R., Andrade, M., Quester, K., Gaytan, P., Huerta-Saquero, A., Vazquez-Duhalt, R. 2018. Surface modification of protein enhances encapsulation in chitosan nanoparticles. *Applied Nanoscience*. 8(5):1197-1203.

[98] Agnihotri, S., Mukherji, S. & Mukherji, S. 2013. Immobilized silver nanoparticles enhance contact killing and show highest efficacy: elucidation of the mechanism of bactericidal action of silver. *Nanoscale*. 5: 7328-7340.

[99] Prozorova, G.F., Pozdnyakov, A.S., Kuznetsova, N.P., Korzhova, S.A., Emel'yanov, A.I., Ermakova, T.G., Fadeeva, T.V. & Sosedova, L.M. 2014. Green synthesis of water-soluble nontoxic polymeric nanocomposites containing silver nanoparticles. *Int J Nanomedicine*. 9: 1883-1889.

[100] Colino, C.I., Millán, C.G., & Lanao, J.M. 2018. Nanoparticles for Signaling in Biodiagnosis and Treatment of Infectious Diseases. *International journal of molecular sciences*, 19(6): 1627-1634.

[101] Jyo, L.H., Haonan, W., Zahra, F. & Daeyeon L. 2018. Effects of polymer–nanoparticle interactions on the viscosity of unentangled polymers under extreme nanoconfinement during capillary rise infiltration. *Soft Matter*. 14: 2438-2446

[102] Herold, B.C., Bourne, N., Marcellino, D., Kirkpatrick, R., Strauss, D.M., Zaneveld, L.J., Waller, D.P., Anderson, R.A., Chany, C.J., Barham, B.J., Stanberry, L.R. & Cooper, M.D. 2000. Poly(sodium 4-styrene sulfonate): an effective candidate topical antimicrobial for the prevention of sexually transmitted diseases. *J Infect Dis*. 181: 770-773.

[103] Ye, Y.S., Rick, J. & Hwang, B.J. 2012. Water Soluble Polymers as Proton Exchange Membranes for Fuel Cells. *Polymers*. 4: 913-963.

[104] Paweena, P., Chakrit, S., Anurat, W., Piyachat, C., Adisorn, T., Patchareenart, S. & Decha, D. 2018. A facile one-pot green synthesis of gold nanoparticle-graphene- PEDOT:PSS nanocomposite for selective electrochemical detection of dopamine. *RSC Advance*. 8: 12724-12732.

[105] Rivero, P.J., Goicoechea, J., Urrutia, A. & Arregui, F.J. 2013. Effect of both protective and reducing agents in the synthesis of multicolour silver nanoparticles, *Nanoscale Research Letters*. 8: 101-109.

[106] Jiaolai, J., Shaofei, W., Hui, D., Haoxi, W., Jun, C. & Junsheng, L. 2018. Rapid and sensitive detection of uranyl ion with citrate-stabilized silver nanoparticles by the surface-enhanced Raman scattering technique. *Royal Society Open Science*. 5: 181099-181107.

[107] Barrera, N., Guerrero, L., Debut, A., Santa-Cruz, P. 2018. Printable nanocomposites of polymers and silver nanoparticles for antibacterial devices produced by DoD technology. *PLoS ONE*. 13(7): 1-11.

[108] Bastus, N.G., Merkoci¸ F., Piella, J. & Puntes, V. 2014. Synthesis of Highly Monodisperse Citrate-Stabilized Silver Nanoparticles of up to 200 nm: Kinetic Control and Catalytic Properties. *Chem. Mater*. 26: 2836-2846.

[109] Zhang, N., Yu, X., Hu, J., Xuea, F. & Ding, E. 2013. Synthesis of silver nanoparticle-coated poly(styrene-cosulfonic acid) hybrid materials and their application in surface-enhanced Raman scattering (SERS) tags. *RSC Adv*. 3: 13740-13747.

[110] Wei, J., Schaeffer, N., Albouy, P.A. & Pileni, M.P. 2013. Surface Plasmon Resonance Properties of Silver Nanocrystals Differing in Size and Coating Agent Ordered in 3D Supracrystals. *Chem. Mater*. 27: 5614-562.

[111] Swenson, J., Smalley, M.V. & Hatharasinghe, H.L.M. 1998. Mechanism and Strength of Polymer Bridging Flocculation. *Phys. Rev. Lett*. 81: 5840-5843.

[112] Runkana, V., Somasundaran, P. & Kapur, P.C. 2006. A population balance model for flocculation of colloidal suspensions by polymer bridging. *Chemical Engineering Science*. 61: 182-191.

[113]   LaMer, V.K. & Dinegar, R.H. 1950. Theory, production and mechanism of formation of monodispersed hydrosols. *Journal of American Chemical Society*. 72: 4847–4854.

[114]   Lim, J.K., Yeap, S.P., Che, H.X. & Low, S.C. 2013. Characterization of magnetic nanoparticle by dynamic light scattering. *Nanoscale Research Letters*. 8: 381-394.

[115]   Wolfgang, H., Nguyen, T.K., Thanh, Jenny, A. & David, G.F. 2007. Determination of Size and Concentration of Gold Nanoparticles from UV−Vis Spectra. *Analytical Chemistry*. 79(11): 4215-4221.

[116]   Mogensen, K. & Kneipp, K. 2014. Size-Dependent Shifts of Plasmon Resonance in Silver Nanoparticle Films Using Controlled Dissolution: Monitoring the Onset of Surface Screening Effects. *The Journal of Physical Chemistry C*. 118(48): 1-13.

[117]   Andrew, J.F., Nicole, C., Kenneth, E.M. & Vladimir, K. 2010. Synthesis of silver nanoprisms with variable size and investigation of their optical properties: A first-year undergraduate experiment exploring plasmonic nanoparticles. *Journal of Chemical Education*. 87(10): 1098-1101.

[118]   Jean Lerm. 2011. Size Evolution of the Surface Plasmon Resonance Damping in Silver Nanoparticles: Confinement and Dielectric Effects. *J. Phys. Chem. C*. 115: 14098-14110.

[119]   Sperling, R.A. & Parak, w.j. 2010. Surface modification, functionalization and bioconjugation of colloidal inorganic nanoparticles. *Phil. Trans. R. Soc. A*. 368: 1333-1383.

[120]   Appel, E.A., Tibbitt, M.W., Greer, J.M., Fenton, O.S., Kreuels, K., Anderson, D.G. & Langer, R. 2015. Exploiting Electrostatic Interactions in Polymer-Nanoparticle Hydrogels. *ACS Macro Lett*. 4: 848-852.

[121]   Mingli, Y., Yanchun, L., Ying, H., Wenxin, C., Jiaqi, Z., Jiecai, H., Zhongyuan, L. & Ming, Y. 2015. Hydrogen Bonding Stabilized Self-Assembly of

Inorganic Nanoparticles: Mechanism and Collective Properties. *ACS Nano*. 9(6): 5807–5817.

[122]   Yuan, G.H.J., Mingrui, D. & Weiqiang, C. 2018. Dispersion of Multi-Walled Carbon Nanotubes Stabilized by Humic Acid in Sustainable Cement Composites. *Nanomaterials*. 8(858): 1-14.

[123]   Samir, C.P. & Vince, C. 2018. Coronene Diimide Containing Redox Active Electrochromic Polymer Film via Electropolymerization of Diphenylamine End Groups. *Journal of Electrochemical Society*. 165(10): 116-122.

[124]   Jang, L.W., Jeon, D.W., Sahoo, T., Jo, D.S., Ju, J.W., Lee, S.J., Baek, J.H., Yang, J.K., Song, J.H., Polyakov, A.Y. & Lee, I.H. 2012. Localized surface plasmon enhanced quantum efficiency of InGaN/GaN quantum wells by Ag/SiO$_2$ nanoparticles. *Optics Express*. 20(3): 2116-2123.

[125] Pandey, Y.N., Papakonstantopoulos, G.J. & Doxastakis, M. 2013. Polymer/Nanoparticle Interactions: Bridging the Gap. *Macromolecules*. 46(13): 5097-5106.

[126] Ramesh, S., Grijalva, M., Debut, A., Albericio, F., Cumbal, L.H. 2016. Peptides conjugated to silver nanoparticles in biomedicine–a "value-added" phenomenon. *Biomaterial Science*. 4(12):1713-1725.

[127]   Hendra, P.J. & Agbenyega, J.K. 1993. The Raman spectra of polymers; John Wiley & Sons: Chichester.

[128]   Bruker Analytische Messtechnik GMBH library, 1995.

[129]   Hyunho, K., Joseph, T.B., Rebeca, S.R., Hattie, L.R., Jiayi, H., Kyle, C.B. & Christy, L.H. 2019. Stabilization of Silver and Gold Nanoparticles: Preservation and Improvement of Plasmonic Functionalities. *Chemical Reviews*. 119(1): 664-699

[130]   Ratyakshi, N., Saiyam, D., Parth, B., Gajender, S., Balaram, P. & Sidhharth, S. 2018. Ag decorated silica nanostructures for surface plasmon enhanced photocatalysis. *RSC Advances*. 8: 20287–20294

[131]   Uznanski, P., Zakrzewska, J., Favier, F., Kazmierski, S., & Bryszewska, E. 2017. Synthesis and characterization of silver nanoparticles from (bis)alkylamine silver carboxylate precursors. *Journal of nanoparticle research : an interdisciplinary forum for nanoscale science and technology*. 19(3): 121-130.

[132]   Inho, J. & Hyunwook, S. 2017. A study on electrical contact at the PEDOT:PSS electrode/molecule interface in large-area molecular junctions. *Journal of the Korean Physical Society*. 71(3): 161–165

[133]   Ren, X., Tan, E., Lang, X., You, T., Jiang, L., Zhang, H., Yin, P. & Guo, L. 2013. Observing reduction of 4-nitrobenzenthiol on gold nanoparticles in situ using surface-enhanced Raman spectroscopy. *Phys. Chem. Chem. Phys*. 15(34): 14196-14201. 2013.

[134]   Myeong, H.J., Amit, S. Sung, B.K., Yeon, S.J., In, S.O., Jung, W.Y., Gun, H.K. & Kyoung, J.C. 2018. Increasing the thermoelectric power factor of solvent-treated PEDOT:PSS thin films on PDMS by stretching. *Journal of Materials Chemistry A*. 6: 15621-15629.

[135]   Ranoszek-Soliwoda, K., Tomaszewska, E., Socha, E. Pawel, K., Anna, I., Piotr, O., Małgorzata, K., Grzegorz, C. & Jaroslaw, G. 2017. *Journal of Nanopartical Research*. 19: 273-280.

[136]   Pattanayak, S., Swarnkar, A., Priyam, A. & Bhalerao, G.M. 2014. Citrate-hydrazine hydrogen-bonding driven single-step synthesis of tunable near-IR plasmonic, anisotropic silver nanocrystals: implications for SERS spectroscopy of inorganic oxoanions. *Dalton Trans*. 43: 11826-11833.

[137]   Tanaka, H., Fujimoto, Y., Koshimizu, M., Yanagida,, T., Yahaba, T., Saeki, K. & Asai, K. 2016. Radiophotoluminescence properties of Ag-doped phosphate glasses. *Radiation Measurements*. 94(10): 1-10.

[138]   Andreeva, N.Z., Vil'chinskaya, N.N., Dmitryuk, A.V., Perminov, A.S., Petrovskii, G.T. & Savvina, O.C. 1985. Influence of activator concentration on the dosimetric properties of radiophotoluminescent glasses. *Atomic Énergiya*. 58(2): 132-135.

[139] Abd. Rahman, I., Ayob, M.T.M., Mohd, H.M.K., Ahmad, A.F., Sharin, S., Mohamed, F., Ab. Aziz, S., Radiman. S. 2016. Effect of silver nanoparticle addition on the structure and characteristics of radio-photoluminescence glass Dosimeter. *Malaysian Journal of Analytical Sciences*. 20(1): 64-72.

[140] Radouan, M., Nadia, B. & Said, A. Study of Chromium-Lead-Phosphate Glasses by XRD, IR, Density and Chemical Durability. *Advances in Materials Physics and Chemistry*. 8: 269-280.

[141] Sidebottom, D.L. 2015. Fragility of network-forming glasses: a universal dependence on the topological connectivity. *Physical Review E*. 92(6): 62804-62813

[142] Saoussen, H., Nassira, C.B. & Adel, M. 2018. Structural Study of Europium Doped Gadolinium Polyphosphates LiGd(PO3)4 and Its Effect on Their Spectroscopic, Thermal, Magnetic, and Optical Properties. *International Journal of Analytical Chemistry*. 2018: 1-11.

[143] Lee, S., Obata, A. & Kasuga, T. 2009. Ion release from $SrO-CaO-TiO_2-P_2O_5$ glasses in Tris buffer solution. *Journal- Ceramic Society Japan*. 117: 935-938.

[144] Saddeek, Y.B., Kaid, M.A. & Ebeid, M.R. 2014. FTIR and physical features of $Al_2O_3–La_2O_3–P_2O_5–PbO$ glasses. *Journal of Non-Crystalline Solids.* 387(1): 30-35.

[145] Moustafa Y.M. & El-Egili K. 1998. Infrared spectra of sodium phosphate glasses. *J. Non-Cryst. Solids*. 240(1-3): 144-153.

[146] ElBatal, F.H., Ouis, M.A., Morsi, R.M.M. & Marzouk, S.Y. 2010. Interaction of gamma rays with some sodium phosphate glasses containing cobalt. *J. Non.-Cryst. Solids*. 356(1): 46-55.

[147] Piao, F., Oldham, W.G. & Haller, E.E. 2000. The mechanism of radiation-induced compaction in vitreous silica. *J. Non-Cryst. Solids*. 276(1): 61-71.

[148] Rai, V.N., Raja Sekhar, B.N., Phase, D.M. & Deb, S.K.. 2014. Effect of gamma irradiation on the structure and valence state of Nd in phosphate glass. *Condensed Matter: Materials Science.* 1406(1): 1-30.

[149]   Anatoly, N.T. 1995. Localized states in wide-gap glasses. Comparison with relevant crystals. *J. Non-Cryst. Sol.* 189(1-2): 1-15.

[150]   Jain, D., Sudarsan, V., Vatsa, R.K. & Pillai, C.G.S. 2009. Luminescence studies on $ZnO-P_2O_5$ glasses doped with Gd_2O_3:Eu nanoparticles and Eu_2O_3. *J. Lumin.* 129(5): 439-443.

[151]   Bausá, L.E., Solé, J.G., Durán, A. & Navarro J.M.F. 1991. Characterization of titanium induced optical absorption bands in phosphate glasses. *J. Non-Cryst. Solids.* 127(3): 267-272.

[152]   Batyaev, I.M. & Leonov, A.V. 2004. Dependence of the Physical and Optical Properties of the $31.5K_2O \cdot 14.5Al_2O_3 \cdot 54P_2O_5$ Glass on the Trivalent Titanium Content. *Glass Phys. Chem.* 30(5): 428-429.

[153]   Dmitryuk, A.V., Paramzina, S.E., Solov'eva, N.D. & Timofeev, N.T. 1996. The influence of glass composition on the properties of silver-doped radiophotoluminescent phosphate glasses. *J. Non-Cryst. Solids.* 202: 173-177.

[154]   Maurel, C., Cardinal, T., Bellec, M., Canioni, L., Bousquet, B., Treguer, M., Videau, J. J. and Richardson, M. 2009. Luminescence properties of silver zinc phosphate glasses following different irradiations. *J. Lumin.* 129(12): 1514-1518.

[155]   Dayanand C., Bhikshamaiah G., Tyagraju V.J., Salagram M. & Krishna Murthy A.S.R. 1996. Structural investigations of phosphate glasses: a detailed infrared study of the x(PbO)-(1-x)P_2O_5 vitreous system. *J. Mater. Sci.* 31(1): 1945-1967.

[156]   Duque, J.S., Blandón, J.S. & Riascos, H. 2017. Localized Plasmon resonance in metal nanoparticles using Mie theory. *Journal of Physics.* 850: 12017-12025.

APPENDICES

List of Publication

Journal Publications

1. Ayob, M.T.M., Rahim, S., Abdul Rahman, I., Lewis, D. & Radiman, S. **2017**. Effect of Chemical Composition on Radio-Photoluminescence Glass Dosimeter Properties. *International Journal of Applied Engineering Research*. 12(22): 12144-12148.

2. Hasim, M.H., Abdul Rahman, I., Rahim, S., Ayob, M.T.M., Sharin, S. & Radiman, S. **2017**. Study on the Effect of -Irradiation on Gadolinium Oxysulfide Nanophosphors (Gd_2O_2S-NPs). *Journal of Nanomaterials*. 2017: 1-6.

3. Ayob. M.T.M., Abdul Rahman, I., Gibson, C., Lockman, Z., Radiman, S. & Lewis, D. **2017**. Adsorption of Polyelectrolyte Layers of polyethyleneimine and poly(sodium 4-styrene sulfonate) on silver nanoparticles surface: A hue changing study. *Indian Journal of Applied Research*. 7(10): 618-623.

4. Basri, N.H., Deraman, M., Daik, R., Ayob, M.T.M., Sahri, M.I., Nor, N.S.M., Dolah, B.N.M. & Soltaninejad, S. **2015**. Electrochemical Impedance Spectroscopy Study of Supercapacitors Using Deposited Nickel Oxide Nanoparticles Carbon Monolith Electrodes. *Advanced Materials Research*. 1112: 236-240.

5. Abdul Rahman, I., Ayob, M.T.M. & Radiman, S. **2014**. Enhanced photocatalytic performance of NiO-decorated ZnO nanowhiskers for methylene blue degradation. *Journal of Nanotechnology*. 2014: 1-8.

6. Ayob, M.T.M., Mohd, H.M.K., Abdul Rahman, I., Mohamed, F., Hidzir, N.M. & Radiman, S. **2016**. Growth and Improvement of Ag-ZnO Nanocomposites for Photocatalytic Activity. *Sains Malaysiana*. 45(8): 1265-1273.

7. Abdul Rahman, I., Ayob, M.T.M., Mohd, H.M.K., Ahmad, A.F., Sharin, S., Mohamed, F., Ab Aziz, S. & Radiman, S. **2016**. Effect of Silver Nanoparticle

Addition on the Structure and Characteristics of Radio-Photoluminescence Glass Dosimeter. *Malaysian Journal of Analytical Sciences*. 20(1): 64-72.

8. Sharin, S., Abdul Rahman, I., Ahmad, A.F., Mohd, H.M.K., Mohamed, F., Radiman, S., Yasir, M.S., Sarmani, S., Ayob, M.T.M. & Ahmad Bastamam, I.S. **2015**. Reduction of Graphene Oxide to Graphene by Using Gamma Irradiation. *Malaysian Journal of Analytical Sciences*. 19(6): 1223-1228.

Published Conference Proceedings

1. Ayob, M.T.M., Ahmad, A.F., Mohd, H.M.K., Abdul Rahman, I. & Radiman, S. **2014**. Effect of Triethanolamine:Ethylenediamine Ratios on CuO Nanoparticles Prepared by Ultrasound Irradiation. *AIP Conf. Proc*. 1614: 8-13.

2. Mohd, H.M.K., Ahmad, A.F., Radiman, S., Mohamed, F., Rosli, N.R.A.M., Ayob, M.T.M. & Abdul Rahman, I. **2014**. Interaction between Silicon Dioxide and Dipalmitoylphosphatidylcholine (DPPC) Vesicles. *AIP Conf. Proc*. 1614: 65-68.

3. Ahmad, A.F., Mohd, H.M.K., Ayob, M.T.M., Rosli, N.R.A.M., Mohamed, F., Radiman, S. & Abdul Rahman, I. **2014**. Effect of Gamma Irradiation on Hyaluronic Acid and Dipalmitoylphosphatidylcholine (DPPC) Interaction. *AIP Conf. Proc*. 1614: 69-74.